# Constraining the Source Craters of the Martian Meteorites: Shock Analysis and Geologic Mapping of Candidate Craters

by

Jarret Sean Hamilton

A thesis submitted in partial fulfillment of the requirements for the degree of

Master of Science

Department of Earth and Atmospheric Sciences
University of Alberta

## Abstract

The ~143 martian meteorites serve as the only rock samples from Mars that are presently available for study in a laboratory setting. These predominantly igneous samples are sourced from the near-surface units adjacent to craters formed during random, hypervelocity impacts of asteroids on the martian surface. Shergottites, a subset of martian meteorites with variable compositions that are otherwise analogous to terrestrial basalts, have crystallization ages that range from 150-2400 Ma and cosmic ray exposure ages that indicate they were ejected from Mars in impact events that occurred <20 Ma ago.

Analysis of shock metamorphism in a suite of 13 previously unstudied martian meteorites was conducted. A combination of optical microscopy, scanning electron microscopy, and laser micro-Raman spectroscopy was used to constrain peak shock pressures and identify high-pressure minerals. Two distinct groups of meteorites based on shock deformation and transformation in the bulk rock were observed, and a detailed shock history was inferred from mineral assemblages, high-pressure phases, and morphology of the shock melt.

Potential martian meteorite source craters were identified using a database of 290 well-preserved craters on the martian surface. Querying based on attributes from four shergottites further limited the number of potential source craters. These attributes include a range of permissible source crater diameters as constrained by impact modeling, craters occurring on Amazonian-age (~3.37 Ga - Present) volcanic terrains, and the model and relative ages of the craters and their nearby surfaces.

Results yielded 52 potential source craters for at least one of four shergottites (Zagami, Tissint, Chassigny, NWA 8159); of these potential source craters, the 8 most well-preserved craters that are potential sources for any of the four meteorites were chosen for further analysis and mapping. These 8 candidate craters and their surrounding geological features were mapped in detail using a combination of visible (CTX, HiRISE, HRSC) and thermal inertia (THEMIS) imagery. Mapping results combined with previous research on crater ages and surface ages were used to evaluate and rank the likelihood of the 8 craters as source(s) of martian meteorites. I find that Zunil, Corinto, and Tooting are the most probable sources of at least one of the shergottites.

# Preface

This thesis is an original work by Jarret S. Hamilton.
No part of this thesis has been previously published.

*“Sometimes you gotta run before you can walk.”*
- Iron Man -

**Acknowledgements**

I would first and foremost like to thank my supervisors, Drs. Chris Herd and Erin Walton, who made this entire thesis possible. Their support and patience as I worked out the kinks and faced numerous setbacks provided me with the determination needed to develop this project and create a thesis-worthy product. Erin's expertise and guidance on shock in meteorites was invaluable during that phase of my research. And thank you to Chris for the many opportunities he provided me to pursue my interests even when they were outside the context of this project.

Many others have supported me throughout my graduate career without whom, this research would not be what it is today. From Western University, I would like to thank Dr. Livio Tornabene for offering his planetary remote sensing expertise and thorough reviews of my work and writing which greatly improved its quality. Thank you to Dr. Alberto Reyes at the University of Alberta who has been a pillar of support for both my academic and industry careers for over four years now. His willingness to continue offering advice and wisdom in every topic that I have approached him with leaves me with the utmost respect and appreciation for him. I would also like to extend my thanks at the University of Alberta to Nathan Gerein (SEM), Nadine Noseworthy (General Administration Assistant), Mark Labbe (Thin Section Laboratory), and Igor Jakab (Digital Imaging Facility). I would like to express my gratitude to Trent Hare at the United States Geological Survey for answering my numerous questions about the Mars cartographic tools and to Tony Irving for loaning several thin sections from the University of Washington Seattle meteorite collection.

I would also like to thank my colleagues for the social support they provided during the many long days spent in the lab or office. Thanks to Christian Veglio for being my personal IT support, to Kelsey Graverson for providing a source of laughter in the office, to Marko Szmihelsky for always lending a supportive ear from over 6,000 km away, to Simon Dahrouge and Fiona Madsen for being the best of pals, and to Herd's Nerds for the many laughs we shared while hunting for meteorites and during our group meetings.

And finally, I would like to thank my parents for their support throughout my entire academic career. Their support allowed me the freedom to pursue my studies over the last seven years.

This research was supported by the Natural Sciences and Engineering Research Council (NSERC) Discovery Grant RGPIN-2018-04902to C. Herd, NSERC Discovery Grant RES0044435 to E. Walton, and the University of Alberta Faculty of Graduate Studies and Research (FGSR) and Graduate Student Association (GSA) travel awards to attend the 50th Lunar and Planetary Science Conference. Jiddat al Harasis (JaH) 479 (two slides; MET11619/TEP1 and /TEP2), Northwest Africa (NWA) 12919 (MET11776/3/TEP), and NWA 10299 (MET11774/1/TEP) were made available through a loan from the University of Alberta Meteorite Collection, Ksar Ghilane (KG) 002 was provided on loan from the Natural History Museum Vienna, and NWA 2646, NWA 7635, NWA 11057, NWA 11073, NWA 11255, NWA 11955, and NWA 12262 were provided by Dr. Tony Irving, from the meteorite collection of the University of Washington Seattle.

# Table of Contents

# List of Tables

## List of Figures

# Chapter 1. Introduction

Planetary geology seeks to study the geology of celestial bodies other than Earth and understand the history and evolution of the solar system itself. The prefix geo- stems from the Greek word ‘gē’, or Earth. Despite this relationship to Earth in its name and the focus on bodies other than Earth, planetary geology maintains the prefix geo- both for convenience and because studying other planets and celestial bodies can often reveal information about our own planet’s formation and evolution. Modern planetary geology was introduced during the Space Race of the 20th century and is based on remote sensing and mapping principles utilized by other facets of geology. During the 20th century, the bulk of planetary science and geology was concentrated on selenography – the study of the Moon. Lunar exploration has continued since the end of the Apollo missions, but a lot of attention has turned towards Mars due to its potential for harboring evidence of ancient life. Mars is a rocky planet, our closest neighbour, and one of the most likely contenders for evidence of discoverable life elsewhere in the universe. This chapter aims to build a foundation of background knowledge and context for Mars and the meteorites that we use to study this planet.

## 1.1 Mars

Mars is the fourth planet from the Sun and one of the four terrestrial planets in our Solar system (Coles et al., 2019). Known for its reddish-brown colouring, Mars is smaller than Earth with about a third of its gravity and an atmosphere with less than 1 kPa of pressure. Mars’ surface colouring results from iron oxidation of the regolith. The rotational period of Mars is roughly the same as Earth, but its calendar year is 687 Earth-days. Daily temperatures on Mars range from -140°C to +30°C and it presently lacks the substantial liquid water oceans that are found on Earth. Mars has two natural satellites, Phobos and Deimos, that are thought to be ejected fragments of Mars, rather than captured asteroids (Glotch et al., 2018).

Early maps of the martian surface date back to at least the 19th century and modern exploration missions have been ongoing since the 1960s with the first landers reaching Mars in the 1970s. The focus of this study will be on the volcanic terrain of Mars, especially in the Tharsis and Elysium regions. The formation and geology of these regions will be discussed in section 1.2.1. In tandem with the late 20th century exponential technology advancements, the data quantity and quality improved dramatically as more missions were launched (McSween and McLennan, 2014). Today, there are six active orbiters (2001 Mars Odyssey, Mars Express, Mars Reconnaissance Orbiter, Mars Orbiter Mission, MAVEN, ExoMars Trace Gas Orbiter), one active lander (Mars InSight), and one active rover (Curiosity) on the surface of Mars with at least a dozen future missions proposed to launch this decade (Fig. 1.1). The Mars missions are outfitted with various scientific tools to study the planet. InSight is equipped with a seismometer to investigate the internal activity of Mars, a heat flow and physical properties package to measure martian temperature, and a radio science instrument to track the wobble of Mars' poles. Curiosity has a series of cameras, spectrometers, radiation detectors, and environmental and atmospheric sensors that are used to determine if Mars is or was ever capable of supporting life. These instruments and more have aided researchers in their pursuit to understand Mars, its history and evolution, and our solar system as a whole.

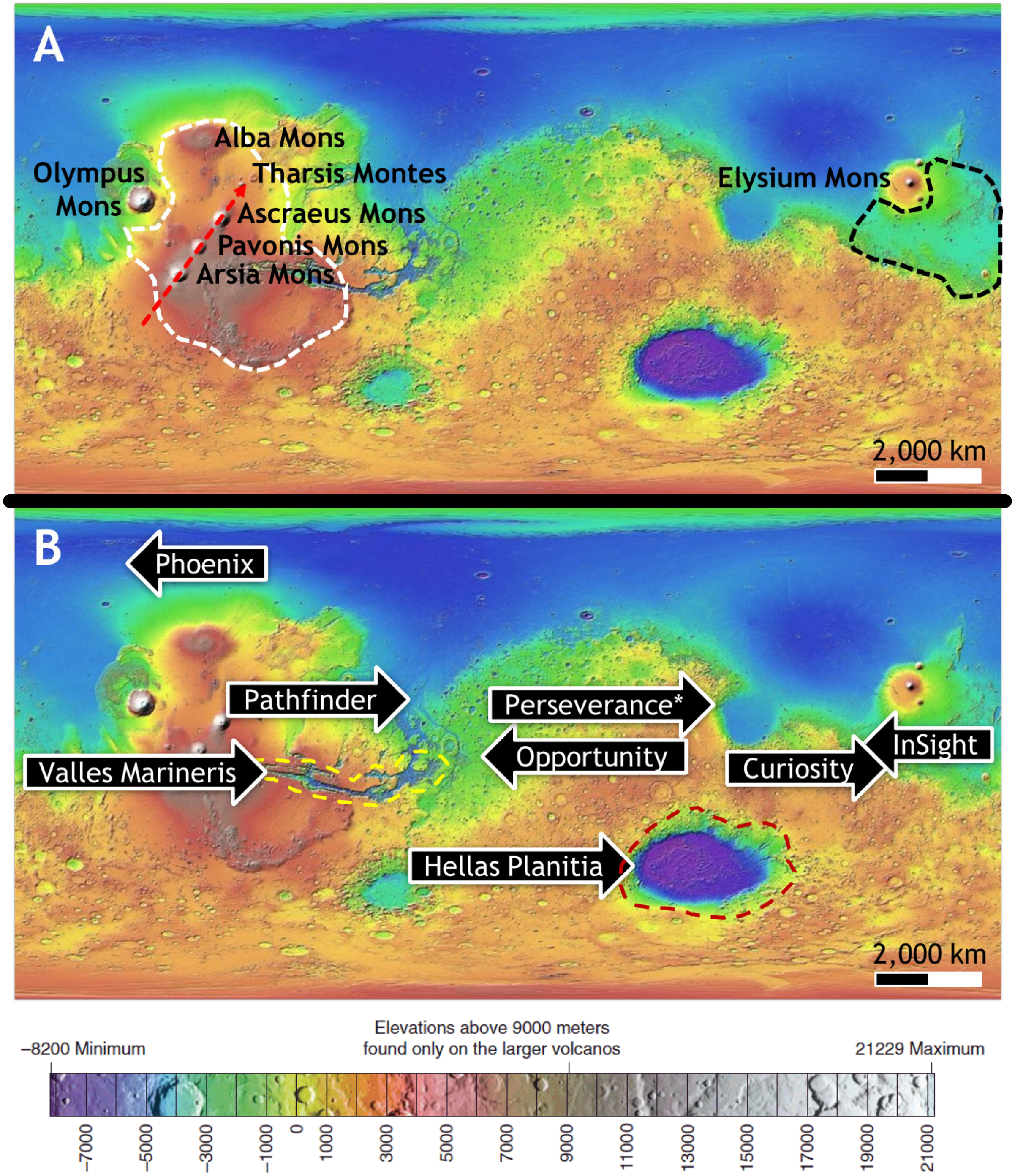

**Fig. 1.1.** Colourized shaded relief map of Mars, its major volcanic features (a), and other notable landmarks (b). Reds and whites represent higher elevations while the blues and purples represent lower elevations. In (a) the white dashed line is an approximate boundary of Tharsis, the red arrow shows the alignment of Tharsis Montes and the black dashed line is the approximate boundary of Elysium Planitia. In (b) the yellow dashed line indicates the location of Valles Marineris and the red dashed line shows the approximate circumference of the impact basin, Hellas Planitia.

### 1.1.1 Mars Geology and Geologic History

Mars accreted and differentiated very rapidly after the formation of the solar system (Carr and Head, 2010). Today, its average crustal thickness is estimated to be ~50 km and the surface is dominated by volcanic plains, layered sedimentary and volcanic deposits, and ice-rich polar deposits (McSween and McLennan, 2014). Early compositional models of Mars' bulk chemical composition relied on extrapolating the composition of martian meteorites, but it is not clear if the current suite of martian meteorites are representative of bulk crust (Hahn and McLennan, 2007; McSween et al., 2009; Taylor, 2013). More recent approaches have suggested that the martian crust is enriched in refractory lithophile elements and depleted in moderately volatile elements (Yoshizaki and McDonough, 2020). The martian core is thought to be composed of mostly iron and nickel with the remainder made up of a lighter element, most likely to be sulfur (Taylor, 2013). Further constraints on the core's structure and composition should be achieved with the successful recent landing and operation of the InSight mission (Yoshizaki and McDonough, 2020; Banerdt et al., 2020).

The geologic history of Mars is divided into three major epochs: the Noachian, Hesperian, and Amazonian. Boundaries for martian epochs vary depending on the cratering chronometry method that is employed, but for the purposes of this study, the Neukum timescale as described and utilized by Coles et al. (2019) will be used. The Noachian era occurred from ~4.15 Ga to ~3.71 Ga and is dominated by undifferentiated volcanic, fluvial, impact, and basin material (Coles et al., 2019; Tanaka et al., 2014). Much of the Noachian deposits have been resurfaced by more recent volcanic activity, but its significant presence in the upper crust suggests that plate tectonics were not actively recycling the more ancient deposits (Carr and Head, 2010; Coles et al., 2019). Instead, much of the martian surface is marked by geologic features resulting from planetary contraction and lithospheric loading in Tharsis and other volcanic provinces during Mars' history. The Middle to Late Noachian is characterized by decreased rates of erosion and weathering, and the formation of valley networks including the beginning of the Valles Marineris canyon system. During the Hesperian from ~3.71 Ga to ~3.37 Ga, erosion, weathering, and valley formation rates decreased exponentially while episodic volcanism produced extensive lava plains. These lower rates of erosion suggest lower aqueous activity compared to the Noachian. Canyons and large outflow channels, and their terminal lakes and seas formed and were subsequently infilled by sedimentary material – these features likely formed by the catastrophic collapse of subsurface ice. The lack of surface aqueous activity during the

Hesperian coincides with evidence of the formation of icy plains deposits on the polar caps of Mars. From ~3.37 Ga to present, Mars has been in the Amazonian period. This period has shown continuous evidence of geologic activity, but at a much lower rate than the Noachian or Hesperian. Vast lava plains produced by massive shield volcanoes overlay older material. These lava plains have been reworked in certain areas, particularly on the flanks of Tharsis Montes, Olympus Mons, and at mid-northern latitudes indicating possible glacial/interglacial periods throughout the Amazonian (e.g. Coles et al., 2019; Viola et al., 2015; Fastook and Head, 2014; Kadish et al., 2008; Head and Marchant, 2003; Forget et al., 2006).

Elysium Planitia and Tharsis are two major volcanic provinces on Mars with a significant amount of their terrain dominated by Amazonian lava flows (Fig. 1.1). Tharsis is the more well-known of the two volcanic regions, as it is the location of the Tharsis Montes and Olympus Mons, a set of massive shield volcanoes that dwarf anything found on Earth or elsewhere in the solar system. Olympus Mons is the largest of these shield volcanoes reaching 25 km in height, a central caldera that is 80 km in diameter, and a near-vertical escarpment on the western flank that is nearly 7 km high. The growth of Tharsis dates to the Noachian and its shear size results from the lack of active plate tectonics on Mars coupled with long-lived volcanism creating a regional bulge (Coles et al., 2019; Bouley et al., 2016). Despite not having plate tectonics, Tharsis shows evidence of tectonic activity in the form of wrinkle ridges, regional and local grabens, and possible rifting (Coles et al., 2019). The seismometer aboard the InSight lander will likely provide further insight into present-day tectonic activity on Mars (Banerdt et al., 2020).

Throughout its history, Mars has hosted a wide range of additional geological and geomorphological processes (Coles et al., 2019). While liquid water is not currently stable on the martian surface, it may reside as brines in subglacial bodies at the polar caps or as seasonal slope lineae (Coles et al., 2019; Lauro et al., 2020; Stillman et al., 2020; Edwards and Piqueux, 2016). However, extensive evidence of past flowing water on the surface of Mars has been detected as early as the Mariner 9 mission in 1971 (Coles et al., 2019). Water was present on the surface of Mars long enough to form glacial features, stream-carved erosional valleys, deltas, and perhaps even ancient oceans (Coles et al., 2019; Head and Marchant, 2003; Forget et al., 2006; Fassett and Head, 2005; Fawdon et al., 2018; Villanueva et al., 2015). Wind is the most influential driver of geologic change on the surface of Mars today (Coles et al., 2019). The wind on Mars causes erosion and sedimentation while producing ripples and dunes throughout the martian surface. Mass wasting and other slope processes seen on Earth are also commonly found on Mars. Features including talus deposits, landslides, rock and ice avalanches, glaciers, debris flows, and fans form where compositional and structural conditions are met. Compositional conditions are primarily constrained by the presence of water and/or ice and bedrock material while structural conditions consist of latitude and local relief and slope gradients. Mass wasting and slope features are found on surfaces that have been modified and steepened by tectonic movements, frost action, wind erosion, and impact deformation. Evidence of hypervelocity impact events, in the form of craters, are a typical feature of the martian surface; however, the distribution of craters is not uniform with older surfaces characterized by higher crater densities compared to younger surfaces (Fig. 1.1). Recent impacts still have many of their morphological features preserved including raised rims and ejecta deposits, and can range from a few meters in diameter upwards of 30 km in diameter (e.g. Tornabene et al., 2006; Tornabene et al., 2012; Mouginis-Mark and Boyce, 2012; McEwen et al., 2005). Large impact craters (>100 km diameter) are less common and are more likely to be partially or completely eroded by martian processes and more recent impacts (Coles et al., 2019). Because the martian crust is not recycled, impacts as recent as a couple of years and as old as the Noachian can be preserved (e.g. Mars Exploration Program, 2018; Frey, 2006). Martian impacts are a vital feature to model chronology and as the source of our only solid samples of the red planet that are available to study on Earth.

## 1.2 The Martian Meteorites

Meteorites are rocks or rock fragments found on the surface of a planetary body that they themselves do not originate from (Rubin and Grossman, 2010). Meteorites are referred to as either “falls” or “finds”. The former is applied when the remains of an observed fireball are recovered shortly thereafter while the latter is applied to meteorites that do not have an observed fireball and thus an unknown fall date. Because meteorites can be subjected to contamination and weathering before their recovery, care must be taken to distinguish terrestrial weathering from pre-impact weathering at their source (e.g. Wright et al., 1989; Stephant et al., 2018). In the world’s collection of meteorites, ~0.7% are lunar in origin, ~0.4% come from Mars, and the significant remainder are asteroid-derived (Krot et al., 2014). Because terrestrial rocks have been recycled by plate tectonics since the formation of Earth, meteorites provide the key material needed to study and understand the early solar system and its evolution. Meteorites can also be studied to develop an understanding of their parent body, i.e. the body on which the rock formed.

Meteoritical research is best used in conjunction with remote sensing analyses and sample return missions to build a more complete picture of the parent body and the solar system. Meteorites can be divided into three major types: stony, stony-iron, and iron. Stony meteorites include chondrites and achondrites, a subset of stony meteorites that are characterized by the lack of chondrules. Chondrites contain chondrules, which are small, spherical inclusions that were formed at the beginning of the solar system and incorporated into asteroids without being erased by parent body melting during the accretionary and differentiation processes of the parent body. This incorporation of chondrules is evidenced by thermal and aqueous overprint. Achondrites can be further subdivided; one of these groups is the focus of this study.

A group of achondrite basaltic meteorites with an unknown source was first proposed to be from Mars in 1980 (McSween and Stolper, 1980). This proposal was based on the young crystallization ages of the basaltic meteorites and corresponding data from the Mariner and Viking missions indicating recent volcanism on Mars' surface. However, a martian origin for these basaltic meteorites was contested because experimental and physical models of hypervelocity impact were unable to account for ejection of unmelted material (Vickery and Melosh, 1983). However, as increasing evidence was acquired through study of new meteorites and the improved impact models were developed, it became clear that these meteorites originate from Mars (e.g. Melosh, 1984; McSween, 1994; Treiman et al., 2000). The history of models leading to our present understanding of the impact ejection process will be discussed in a later section (section 1.3.3).

Martian meteorites were traditionally grouped into three subgroups derived from archetypal meteorite falls. These meteorites – Shergotty, Nakhla, and Chassigny – had long been noted to be distinct from other meteorites in terms of their petrology and geochemistry. Without a known parent body, these meteorites and those sharing common lithologies and other physical characteristics were colloquially referred to as 'SNC' meteorites. This naming convention has persisted in scientific literature even as a martian origin has become widely accepted. Alternative classification schemes have been proposed but do not provide comprehensive groups for the multitude of unique martian meteorites or accurate descriptions of their bulk rock composition (e.g. Mittlefehldt, 1994; McSween, 1994). Instead, a classification scheme that provides sufficient descriptors to accurately group similar martian meteorites while noting their distinct characteristics compared to terrestrial analogues has been developed (Irving et al., 2010; Walton et al., 2012). The primary subgroups consisting of shergottites, nakhlites, and chassignites are maintained while adding descriptors for their textural, trace element, and bulk major element characteristics (Walton et al., 2012). For example, Shergotty, which was originally described plainly as a basalt with characteristics similar to terrestrial basalts, would be classified as an enriched mafic diabasic shergottite under the proposed classification scheme. Basaltic shergottites comprise the vast majority of martian meteorites and are analogous to terrestrial basalts with the exception of their compositional characteristics indicating the need for this unique classification system.

Shergottites are the focus of this study. Shergottites are Amazonian-aged martian meteorites, as demonstrated by crystallization ages from Rb-Sr, Sm-Nd, and U-Pb chronometers. The majority of shergottites have crystallization ages ranging from ~150 to ~2400 Ma including Northwest Africa (NWA) 7635 and NWA 8159, which have crystallization ages of 2.40 ± 0.14 Ga and 2.37 ± 0.25 Ga, respectively (Udry et al., 2020; Lapen et al., 2017; Herd et al., 2017). The four main types of shergottites are basaltic, olivine-phyric, poikilitic, and gabbroic which are further subdivided by the classification scheme described above (Walton et al., 2012; Udry et al., 2020). NWA 7635, NWA 8159, and NWA 10414 are notably distinct from these shergottite types but have overlapping ejection ages.

### 1.2.2 Cosmic-Ray Exposure Ages

Objects in space unprotected by a significant atmosphere and/or overlying material are subject to bombardment by solar and extra-solar rays that react with elements and molecules to produce nuclides (Fig. 1.2). A cosmic-ray exposure (CRE) age is the length of time that an object is exposed to these solar and extra-solar rays and can be determined by measuring the ray-produced nuclides in the object. To accurately calculate the CRE age, the production rate and shielding must be determined. The production rate is the frequency with which a specific nuclide is produced via bombardment and shielding is the process by which production rate decreases with increasing depth from the surface of the object (Fig. 1.2). Because meteoroids are heated by friction and compression of the atmosphere during the entry process on Earth, the outside of the meteoroid experiences melting, ablation, and then rapid cooling and quenching. The newly created fusion crust represents some depth relative to the surface of the meteoroid prior to atmospheric entry. This unspecified depth must be corrected to yield precise shielding models. Calculations for shielding effects in chondrites are available (e.g. Leya and Masarik, 2009; Leya et al., 2000), but martian meteorites do not share a direct relationship with regards to shielding with chondrites due to different physical and chemical characteristics. Models for shielding effects in martian meteorites have been proposed, but their legitimacy is contested (Wieler et al., 2016). Martian meteorites are ejected from the near-surface units adjacent to impacts and are protected from cosmic rays during their residence on Mars by its atmosphere and material that superpose the meteorites. Once an ejection event occurs, the CRE clock begins ticking. By combining the cosmic-ray exposure age of a meteorite with its terrestrial residence, the meteorite's approximate ejection age can be determined.

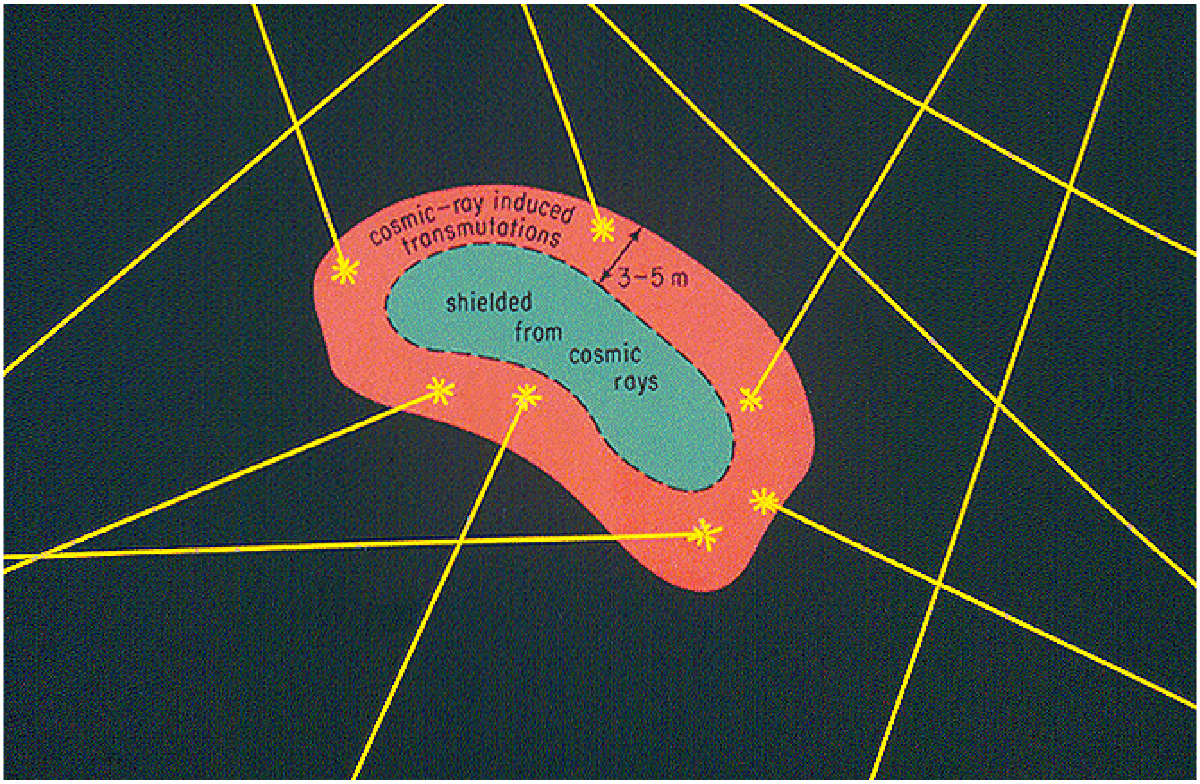

**Fig. 1.2.** Diagram of basic CRE principles (from Lunar and Planetary Institute).

The most used nuclides for martian meteorite CRE dating are $^{3}$He, $^{21}$Ne, and $^{38}$Ar, while less commonly used nuclides include $^{10}$Be, $^{15}$N, $^{53}$Mn, and $^{83}$Kr (Table 1.1). Each system has advantages and disadvantages; therefore, best practices are to use multiple nuclide systems (e.g. Wieler et al., 2016). Determining the CRE age for individual martian meteorites allows us to group the meteorites into distinct impact ejection events when they also share a common lithology. Nyquist et al. (2001) suggested ≤8 ejection events for martian meteorites during a time at which there were only 16 identified martian meteorites. An updated assessment of CRE ages proposed a maximum of 11 distinct launch events (McSween 2015); however, as the inventory of martian meteorites continues to grow, so does the number of meteorite-producing ejection events. The 262 presently known martian meteorite samples indicate ≥11 impact ejection events (Udry et al., 2020).

**Table 1.1.** Cosmogenic nuclides used for calculating cosmic ray exposure ages (after Herzog and Caffee, 2014)

| Nuclide | Half-life (Ma) |
|---|---|
| *Radionuclides* | |
| $^{14}C$ | 0.00573 |
| $^{59}Ni$ | 0.076 |
| $^{41}Ca$ | 0.1034 |
| $^{81}Kr$ | 0.229 |
| $^{38}Cl$ | 0.301 |
| $^{26}Al$ | 0.717 |
| $^{10}Be$ | 1.51 |
| $^{53}Mn$ | 3.74 |
| $^{129}I$ | 15.7 |
| *Stable Nuclides* | |
| $^{3}He$ | |
| $^{21}Ne$ | |
| $^{38}Ar$ | |
| $^{83}Kr$ | |
| $^{126}Xe$ | |

### 1.2.3 Martian Meteorite Sources

Martian meteorites are sourced from the near-surface units of impact craters on Mars (Melosh, 1984). Shock pressures required to accelerate rock fragments to velocities exceeding the martian escape velocity (>5.03 km/s) were previously calculated to be as high as 100 GPa (Melosh, 1984). At these extreme pressures, whole-rock melting, vaporization, and a high degree of shock damage are expected (Melosh, 1984; Stöffler, 2018); however, most martian meteorites have experienced relatively moderate shock pressures 5 – 45 GPa), as evidenced by transformation and deformation features in constituent minerals (e.g. Walton and Spray, 2003; Sharp and deCarli, 2006; El Goresy et al., 2013; Walton et al., 2014; Walton et al., 2016; Sharp et al., 2019). Melosh (1984) proposed that up to 5% projectile mass can be accelerated to escape velocities while experiencing minimal shock pressures via spallation. A hypervelocity impact into a solid surface initiates a process that can be divided into three distinct stages: contact/compression, excavation, and modification (Bjork et al., 1967; Melosh, 1984). During the first stage of impact, a shock wave separates from the impact zone and continues to propagate into the target (Bjork et al., 1967). Material within this zone is characterized by a sudden acceleration as the shock wave passes through, follow by a slower deceleration or ‘decay’ to rest (Fig. 1.3, Bjork et al., 1967).

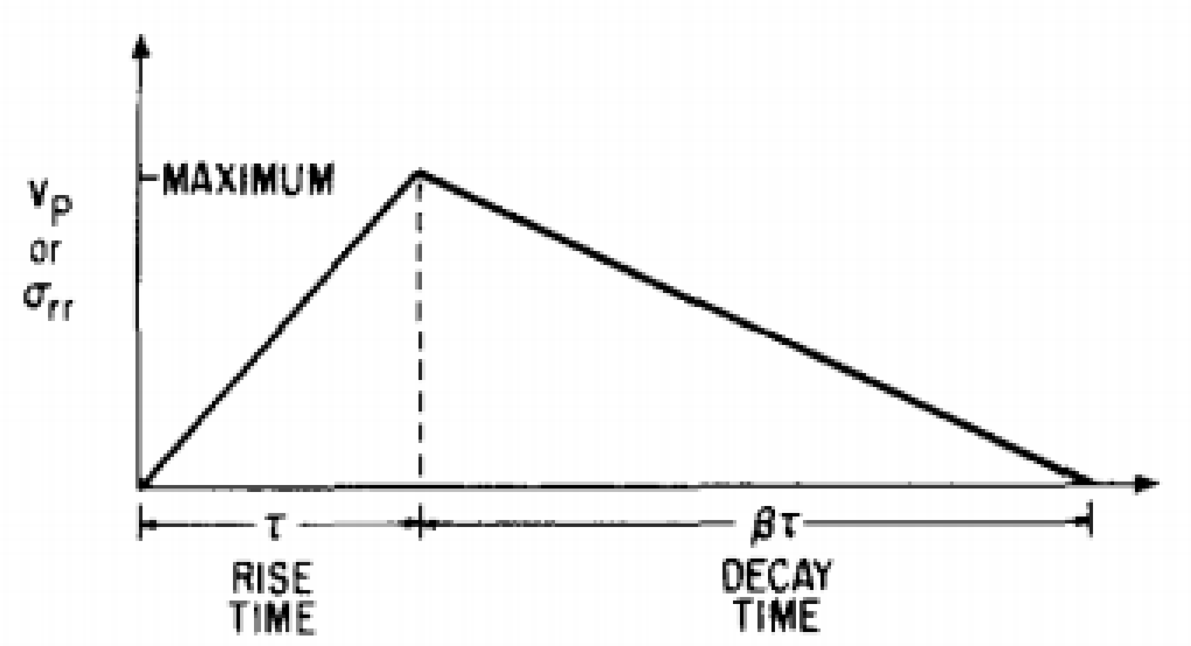

**Fig. 1.3.** Diagram showing the rapid rise in pressure ($V_p$ or $O_{rr}$) from zero (rise time) followed by a significantly longer period (decay time) to return to zero. This rapid rise and slow decay describe pressures experienced by particles during a stress pulse (Melosh, 1984).

Melosh (1984) used the demonstrated “detached shock” to propose a spallation model that describes the effects of a projectile on the nearby area in the moments following an impact with a solid surface (Fig. 1.4). The spallation model describes a ‘goldilocks' zone adjacent to the impact where rocks experience low shock pressures and high ejection velocities (Fig. 1.4). Rocks within this goldilocks zone experience a large vertical pressure gradient, which is the result of a free surface. For Mars, the free surface is the contact between crustal rocks and the atmosphere. This vertical pressure gradient develops from interference of high-pressure shock waves arriving directly from the equivalent centre and rarefactions, or tensile waves, reflected from the free surface (Melosh, 1984; Bowling et al., 2020). The equivalent centre is a point from which the shock waves propagate below the point of impact and is equal to roughly one projectile diameter. The interference of these waves reduces the overall pressure experienced by rocks near the surface, within the goldilocks zone. However, pressure increases rapidly with depth. This pressure gradient (high pressure at depth / lower pressures near the surface) is responsible for ejection of solid rocks into space, some of which are destined to become martian meteorites.

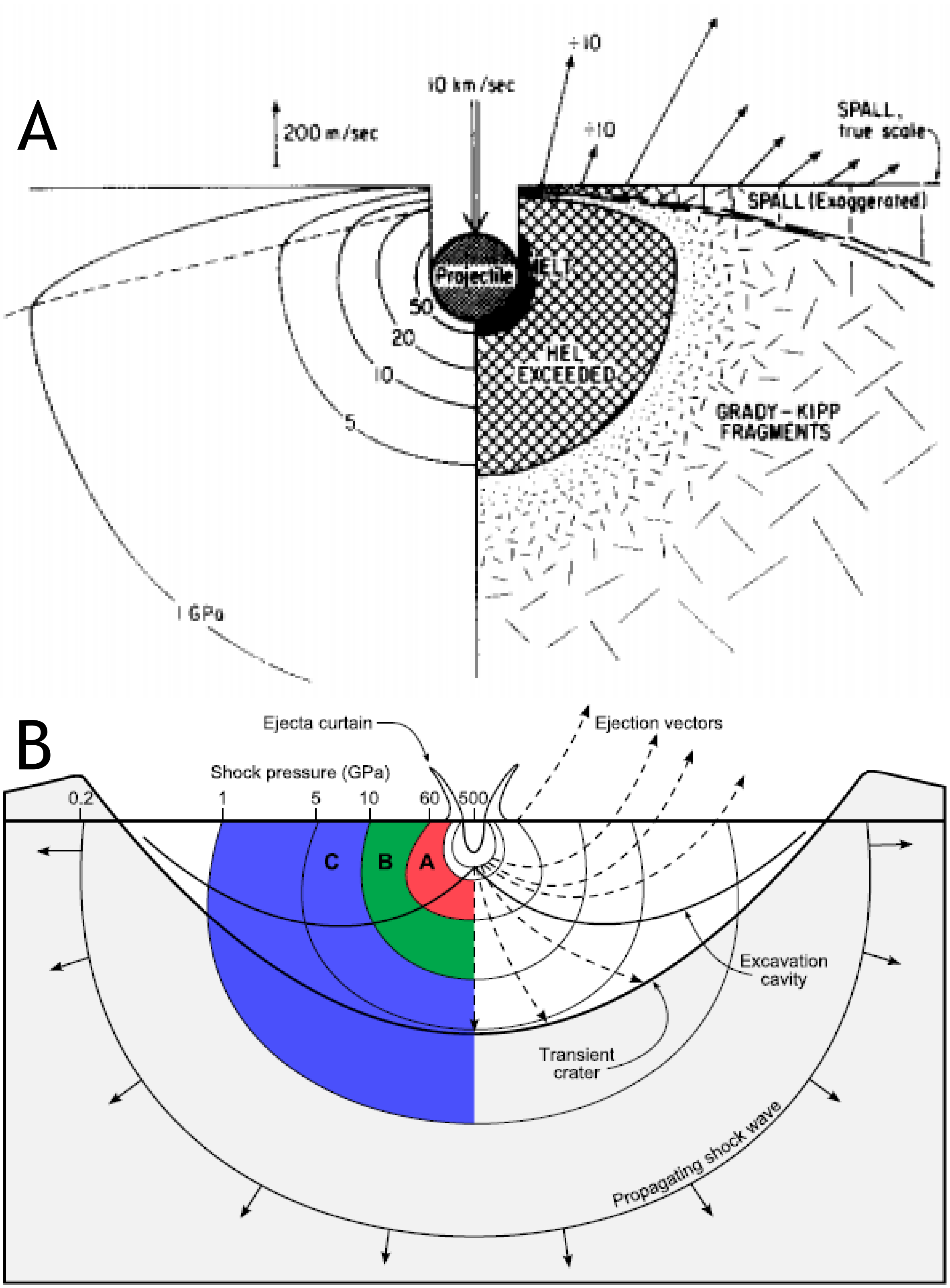

**Fig. 1.4.** A) The spallation model by Melosh (1984). B) An updated schematic of the currently accepted spallation model showing shock zoning and particle motion during an impact (Stöffler et al., 2018)

Vickery and Melosh (1987) utilized the Melosh (1984) spallation model to estimate the diameter of impact craters required to produce various fragment sizes that are accelerated to the martian escape velocity. Crater production rates and cosmic ray exposure ages were incorporated to propose probable histories for martian meteorites (Vickery and Melosh, 1987). The results suggested that martian meteorites are ejected during the formation of a large impact crater (>100 km diameter; Vickery and Melosh, 1987). The 8 martian meteorites in the world's collection in 1987 had CRE ages of 0.5 Ma – 10 Ma which is not consistent with the model age of an impact creating a >100 km diameter crater of ~200 Ma (Vickery and Melosh, 1987). Vickery and Melosh proposed that this discrepancy between ejection ages and impact ages was due to a collisional spallation of the ejected material in space sometime after ejection that resulted in a CRE age 'reset'.

A large crater origin for martian meteorites was revisited by Nyquist et al., (2001). Grouping of the martian meteorites based on their crystallization ages, cosmic ray exposure ages, and petrologic type resulted in a minimum of 3 ejection events, up to a maximum of 8 (Nyquist et al., 2001). McSween (2015) also suggested at least 4 ejection events for martian meteorites. The number of ejection events constrained by the martian meteorites through their crystallization ages, CRE ages, and lithological type, suggest a minimum of 3-4 impact ejection events, not one single large event. While a large crater origin is still plausible, it is less likely when considering the number of impact structures on the martian surface that are >100 km (i.e., crater size frequency distribution). In 1987, when Vickery and Melosh first proposed a large crater origin for martian meteorites, there were only 8 martian meteorites in the world's collection. This limited amount of data may have contributed to the large crater origin proposal.

High resolution computer simulations of the impact process demonstrated that fragments large enough (~$10^7$ dm) to result in our current collection of martian meteorites can be ejected from craters as small as ~3 kilometers in diameter (Head et al. 2002). By modifying the simplified arbitrary lagrangian-eulerian (SALE) computer program (Amsden et al., 1980) for the processes and characteristics of hypervelocity impacts on the martian surface, a smallest impactor of 150 meters diameter was shown to be capable of producing martian meteorites (Head et al., 2002). The resulting crater of 3.1 kilometers diameter (Head et al., 2002) is a quarter of the first analytical calculations for minimum crater sizes (Melosh, 1984) and nearly two orders of magnitude smaller than the required crater size suggested by Vickery and Melosh (1987). Head et al. (2002) also found that the recurrence interval of martian meteorite-producing events is short enough to fit the young cosmic ray exposure ages of the meteorites even when considering the broad range of crystallization ages (Nyquist et al., 2001).

### 1.2.4 Shock Metamorphism

Martian meteorites undergo physical and chemical changes known as shock metamorphism because of the rapid change in temperature and pressure produced by shock wave compression and decompression during a hypervelocity impact. Meteorites such as Allan Hills (ALH) 84001 and NWA 7034 are breccias and therefore record multiple shock events, but more commonly, the recorded shock in martian meteorites is from the strongest shock event – typically their ejection event (Mittlefehldt, 1994; Lapen et al., 2010; Agee et al., 2013; Sharp and deCarli, 2006). The extent of shock in a given martian meteorite can be classified based on diagnostic features including changes in petrologic texture, crystal structure, and formation of new minerals (Fig. 1.5). Classifying shock metamorphism in martian meteorites allows researchers to quantify the shock pressure experienced by the meteorite through calibration from shock-recovery experiments. Shock metamorphism will be discussed in greater detail in Chapter 2.

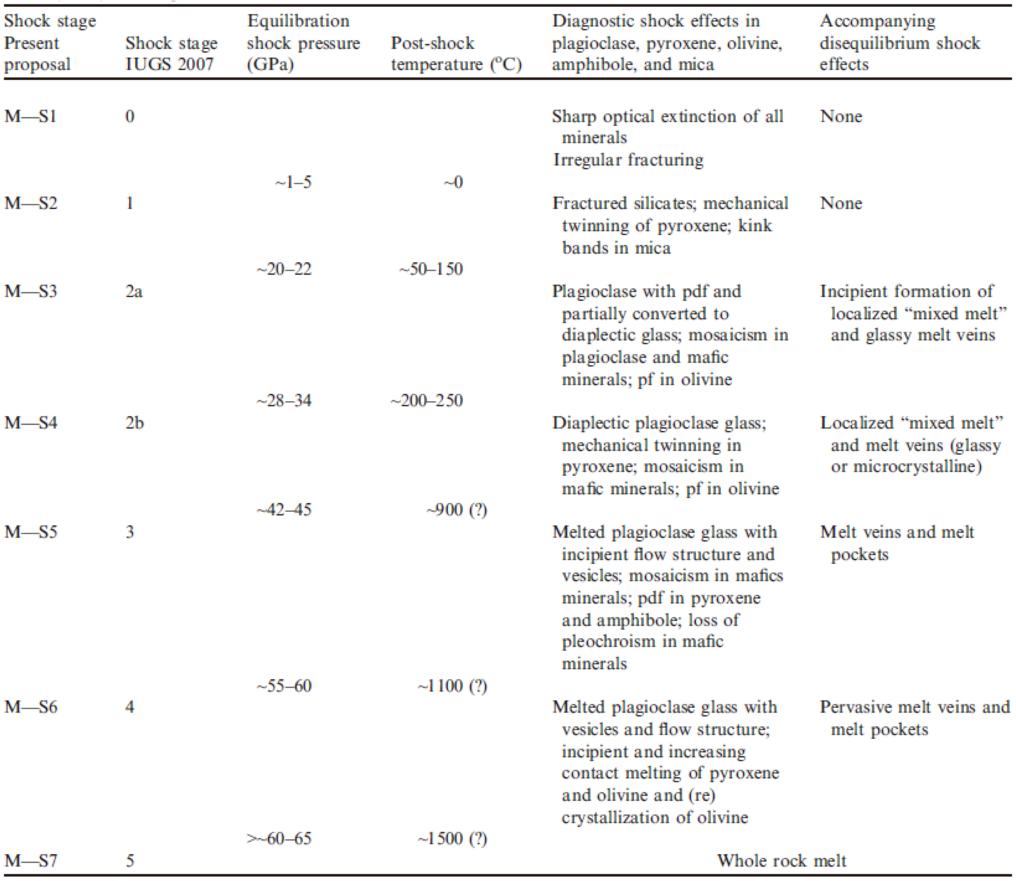

| Shock stage Present proposal | Shock stage IUGS 2007 | Equilibration shock pressure (GPa) | Post-shock temperature (°C) | Diagnostic shock effects in plagioclase, pyroxene, olivine, amphibole, and mica | Accompanying disequilibrium shock effects |
|---|---|---|---|---|---|
| M—S1 | 0 | | | Sharp optical extinction of all minerals<br>Irregular fracturing | None |
| | | ~1–5 | ~0 | | |
| M—S2 | 1 | | | Fractured silicates; mechanical twinning of pyroxene; kink bands in mica | None |
| | | ~20–22 | ~50–150 | | |
| M—S3 | 2a | | | Plagioclase with pdf and partially converted to diaplectic glass; mosaicism in plagioclase and mafic minerals; pf in olivine | Incipient formation of localized "mixed melt" and glassy melt veins |
| | | ~28–34 | ~200–250 | | |
| M—S4 | 2b | | | Diaplectic plagioclase glass; mechanical twinning in pyroxene; mosaicism in mafic minerals; pf in olivine | Localized "mixed melt" and melt veins (glassy or microcrystalline) |
| | | ~42–45 | ~900 (?) | | |
| M—S5 | 3 | | | Melted plagioclase glass with incipient flow structure and vesicles; mosaicism in mafics minerals; pdf in pyroxene and amphibole; loss of pleochroism in mafic minerals | Melt veins and melt pockets |
| | | ~55–60 | ~1100 (?) | | |
| M—S6 | 4 | | | Melted plagioclase glass with vesicles and flow structure; incipient and increasing contact melting of pyroxene and olivine and (re) crystallization of olivine | Pervasive melt veins and melt pockets |
| | | >~60–65 | ~1500 (?) | | |
| M—S7 | 5 | | | Whole rock melt | |

**Fig. 1.5.** A summary of criteria used to classify the shock stage of mafic rocks. This classification applies to martian meteorites as they are all mafic (Stöffler et al., 2018).

### 1.2.5 The Importance of Martian Meteorites

Martian meteorites are the only currently accessible rock pieces from the red planet available for laboratory-based study (e.g., McSween and Stolper, 1980; Melosh, 1985; McSween, 1994; Treiman et al., 2000; Head et al., 2002; Bowling et al., 2020). The only other methods available to study Mars are *in situ* analyses conducted by rovers and landers, and orbital analyses from various instruments. These remote methods, while useful in constraining geological context and studying surface terrain, are limited in capacity compared to laboratories on Earth. The current suite of martian meteorites is exclusively igneous providing unique insight into Mars.

Studying igneous Mars provides evidence pertaining to its geological history and evolution, its bulk composition, and the interior and surface of the planet. Our understanding of Mars' geological history is limited because the meteorites are from unknown locations on the martian surface. We can greatly enhance the scientific value of igneous martian rocks if we are able to link individual meteorites to source impact craters.

The Mars Exploration Program Analysis Group (MEPAG) has several scientific goals that can be met completely or in part by studying igneous martian rocks including both martian meteorites and a sample return mission that is currently underway (MEPAG, 2020; Beaty et al., 2019). Determining if Mars ever supported, or still supports, life has been a primary goal of martian exploration since its inception. Altered sedimentary and hydrothermal rocks are potential zones of past and present habitability and could contain evidence of past biological activity. Because igneous rocks are protoliths for sedimentary and hydrothermal rocks, studying them to constrain igneous processes can provide insight into their alteration processes. A second goal of MEPAG is to understand the processes and history of climate on Mars. One such process is the evolution of martian magmas and their degassing of volatiles leading to liquid water and other life sustaining elements in the crust. Studying martian igneous rocks also supports the MEPAG goal to understand the origin and evolution of Mars as a geological system. This goal will provide insight into both the evolution of terrestrial planets and the solar system. Because a significant portion of the martian surface is covered by volcanic rocks, studying these rocks will help constrain the processes, composition, and structure associated with the martian crust and interior. Indeed, igneous martian rocks may also reveal evidence of the timing of the martian dynamo and its subsequent demise. Until Mars sample return is a reality, martian meteorites are the only physical samples that can be studied in pursuit of these goals.

Despite the availability of 143 martian meteorites for study, research goals are limited due to a lack of geological context (Udry et al., 2020). This study aims to develop an approach to link martian meteorites to their source craters, providing the necessary geological context to constrain Mars' geological timescale and specific magmatic processes. By linking martian meteorites to their source craters, we can potentially improve martian chronology including by adding a 'golden spike' to chronology boundaries and thus alleviating the significant discrepancies of Hartmann and Neukum geological timescales (e.g., Coles et al., 2019). In the next chapter, I analyze the shock effects in a suite of understudied martian meteorites and outline how studying the shock in meteorites can be used to expand the list of martian meteorites suitable for the source crater linking process. In Chapter 3, I describe and discuss a comprehensive methodology to narrow down and prioritize candidate source craters for martian meteorites. Future work to further constrain martian meteorite source craters and the implications of this work is reviewed in Chapter 4.

# Chapter 2. Shock Metamorphism of Martian Meteorites

## 2.1 Introduction

Shock metamorphism is the process by which rocks and minerals undergo a petrologic change from propagating shock waves generated by hypervelocity impact events. These shock waves induce a virtually instantaneous increase in pressure and subsequent decompression upon arrival of a release, also called a rarefaction, wave. Shock metamorphism results in deformation and transformation processes that are recorded in the rock. The adiabatic decompression from a specific shock pressure-temperature to ambient pressure leaves the shocked materials with an elevated temperature, referred to as a post-shock temperature increase. The post-shock temperature increases with increasing shock pressure, up to the point of melting or even vaporizing. Shock pressures in impact events may exceed 100 GPa at the point of impact (Fig. 1.4). Deformation features resulting from shock metamorphism form in the pressure range of ~5 – 60 GPa (Fig. 1.4). These features consist of irregular and planar fractures, planar deformation features, development of undulatory extinction, mosaicism, and mechanical twinning (Stöffler et al., 2018). High pressures generated by an impact event (>10 GPa) can induce phase transformations of various minerals into high-pressure polymorphs or produce local shock melting by friction or void collapse, in the form of veins and pockets, respectively. High-pressure phases can form during shock as a result of a solid-state transformation, as decomposition products, or by quenching of shock melt.

Several different classification schemes for shock effects in meteorites have been developed over the past 100 years (e.g. Brezina, 1904; Stöffler et al., 1991; Fritz et al., 2017). These classification schemes relay on progressive shock effects in rock-forming minerals (feldspar-olivine-pyroxene-quartz) and are calibrated by shock-recovery experiments. Stöffler et al. (2018) proposed an updated classification scheme by combining the type of shocked rock or sediment and a numeric scale of shock metamorphism stages based on bulk shock pressure. The eight rock types are felsic (F), mafic (M), anorthositic (A), ultramafic (U), sedimentary rocks (SR), unconsolidated sediment (SE), and regoliths (RE). These eight rock types are then divided into stages of increasing pressure, and therefore shock metamorphism, from S1 – Sx where S1 is an unshocked rock and x represents whole-rock melting. The value of x ranges from S5 - S7 depending on the type of rock. For example, a complete shock classification for a mafic rock shocked to stage 5 would be written as M-S5.

Martian rocks from the near-surface units adjacent to craters created by random hypervelocity impacts can experience sufficient acceleration to be ejected from the martian atmosphere. Some of these rocks are eventually delivered to Earth as meteorites. Martian meteorites, therefore, exhibit shock metamorphism as a result of this impact launch event. The traditional classification of martian meteorites into shergottites, nakhlites, and chassignites (SNCs) has been further developed and refined to represent the petrologic diversity in the world's collection. Bulk major elemental ratios, textural qualifiers, and trace element characteristics provide a descriptive definition of the meteorite and its classification in this scheme (Walton et al., 2012). This study will focus on unbrecciated martian basaltic meteorites, commonly referred to as shergottites.

### 2.1.1 Shock Metamorphism in Shergottites

Shergottites comprise the majority of martian meteorites with ~132 out of ~143 currently in the world's collection (Irving, 2020). Shergottites are composed predominantly of high-Ca plagioclase feldspar (labradorite) and pyroxene, and also include olivine-phyric and orthopyroxene-phyric subsets. Most shergottites show evidence of strong shock metamorphism including partial to complete transformation of plagioclase to maskelynite and deformation in olivine and pyroxene (Sharp and deCarli, 2006; Walton et al. 2014; Fritz et al., 2019; Stöffler et al., 2018; Sharp et al., 2019; Walton et al., 2012). Despite this strong shock metamorphic overprint, the impact history of shergottites is typically overlooked in petrologic descriptions, and a systematic study of shock metamorphism in many shergottites is lacking.

The response of feldspar to shock has been studied in great detail due to its widespread occurrence in many rock types (felsic-mafic-chondritic). Maskelynite is a diaplectic glass of plagioclase composition (Fritz et al., 2019). Diaplectic glasses are formed by shock waves and differ from typical amorphous phases that form by quenching from a liquid – diaplectic glasses lack vesicles and flow structures while preserving grain boundaries, cleavages, chemical zoning, exsolution, and twin lamellae (von Engelhardt et al., 1967). Diaplectic glass forms by the pressure-induced collapse of the crystal lattice (Fritz et al., 2019) whereas "normal" glass forms when pressures exceed the stability of maskelynite formation, resulting in plagioclase melting and quenching upon pressure release. Constraints have been established to relate pressure and temperature conditions to maskelynite formation. A recent detailed study of maskelynite formation provided new shock-recovery experiments and a thorough review of literature data (Fritz et al. 2019).

These experiments show that the formation of diaplectic glass is temperature independent at low temperatures (<540 K) but is strongly dependent on plagioclase composition. Low-Ca feldspars transform to maskelynite at 25-45 GPa and normal glass above 45 GPa. In contrast, high-Ca feldspars transform to maskelynite at ~32-45 GPa and normal glass above 45 GPa. Martian meteorites are ejected from near-surface units within this low-temperature regime (<540 K), and plagioclase composition can be quantified using the electron microprobe; therefore, the formation of maskelynite is an effective indicator of bulk rock shock pressure (e.g. Walton et al. 2014; Freeman et al., 2008; Pittarello et al., 2020A; Pittarello et al., 2020B). Recently, several shergottites have been documented that preserve crystalline igneous plagioclase, which requires relatively low bulk shock pressures of ~15- 23 GPa (Northwest Africa (NWA) 8159, Sharp et al. 2019; NWA 7635, Lapen et al. 2017; NWA 10416, Walton et al. 2016).

In addition to maskelynite, other high-pressure phases (Table 2.1) are typically found in shergottites where they are generally restricted to areas adjacent to, and within, quenched shock melt. This association is attributed to elevated temperature gradients in the vicinity of shock melt and by non-hydrostatic (shear) stress conditions (see discussion in Walton et al. 2016). High-pressure phases in shergottites may form by a solid-state transformation from a precursor igneous mineral, as a decomposition product, or by crystallization from shock melt before pressure release. During a shock event, localized 'hot spots' are generated, experiencing pressures and temperatures that can exceed that of the bulk rock by upwards of an order of magnitude. In contrast, the bulk rock moves towards an equilibrium shock pressure (Sharp and DeCarli, 2006). These hot spots are the result of frictional melting along shear planes to form shock veins or by shock impedance contrasts, including the collapse of void space (e.g., fractures, vesicles), to form shock melt pockets. Stöffler et al. (2018) noted that high-pressure minerals are limited in constraining specific pressure or temperature conditions unless the exact formation mechanism is known. Shock effects recorded in the bulk rock more reliably constrain the shock pressure-temperature history experienced by a meteorite. High-pressure minerals may be used to constrain the crystallization conditions of the shock melt; however, because shock melt typically crystallizes during pressure release, these minerals are more indicative of the rate of pressure decay, rather than peak shock conditions.

**Table 2.1.** List of minerals that are stable at high-pressure found in martian meteorites and their corresponding parent phase.

| Parent Phase | Parent Phase Composition | High-pressure Phase |
|---|---|---|
| Silica* | $SiO_2$ | Stishovite |
| Silica* | $SiO_2$ | Coesite |
| Silica* | $SiO_2$ | Seifertite (α-$SiO_2$) |
| Feldspar | Plagioclase | Zagamiite |
| Feldspar | Plagioclase | Tissintite |
| Feldspar | Plagioclase | Hollandite |
| Feldspar | Plagioclase | Lingunite |
| Pyroxene | **N/A | Majorite |
| Feldspar | Plagioclase | Maskelynite |
| Olivine | Forsterite (Mg-rich) | Ringwoodite |
| Olivine | Fayalite (Fe-rich) | Ahrensite |
| Olivine | **N/A | Bridgmanite |
| Apatite | **N/A | Tuite |

Notes: *Silica in shergottites may be tridymite or beta-quartz; **N/A = not applicable, the associated high-pressure phases are decomposition products and therefore their chemical formula differs from the parent phase

Deformation features in meteorites form as shock waves propagate through the material. The interactions between the shock wave and any heterogeneous material such as a polymineralic rock is a complex process that becomes significantly more complex as the scale of observation decreases (Sharp and DeCarli, 2006). Planar fractures occur in olivine and pyroxene over a wide range of shock pressures (5-65 GPa; Stöffler et al., 2018) with lower pressures producing {001} fractures and higher pressures producing {001} and {hk0} fractures in olivine. Mosaicism is fine scale fracturing and plastic deformation; it occurs when small domains are highly deformed and rotated inside a former single crystal. Mosaicism is observed upon stage rotation, when viewing a thin section under cross polarized transmitted light, and has the appearance of stained glass. Pyroxene and olivine display mosaicism at moderate to high shock pressures (20-70 GPa and 15-65 GPa, respectively; Stöffler et al., 2018). Over the pressure range at which mosaicism forms in olivine and pyroxene (15-70 GPa), the intensity of mosaicism increases. This increase can be described qualitatively as weak, moderate, or strong mosaicism and is observed as an increase in the number and decrease in the size of misorientations upon stage rotation. Although the intensity of mosaicism is difficult to quantify optically in thin section, it has been documented as an increase in the number and misorientation of domains using X-ray diffraction (Hörz and Quaide 1973). Planar deformation features (PDFs) are an intermediate shock pressure product typically found in the major minerals of mafic rocks (i.e., feldspars and olivine) but can also be present in other phases such as quartz (Stöffler et al., 2018). These features consist of parallel sets of amorphous lamellae that have specific crystallographic orientations. Pyroxene displays planar deformation features at 30-70 GPa and olivine displays them at 30-60 GPa. Shock-induced undulatory extinction develops at relatively low shock pressures (<20 GPa in olivine, <30 GPa in pyroxene; Stöffler et al., 2018) and is characterized by mineral grains that exhibit waves of extinction in cross polarized light while rotating the stage. Mechanical twinning is a deformation feature found in minerals of low symmetry (Trepmann and Stöckhert, 2001); it is a common feature of plagioclase that occurs at all stages of shock resulting from shear stress applied to crystals (Stöffler et al., 2018; Kollè and Blacic, 1982) and also in pyroxene.

A rock may be assigned to a specific shock stage by observing the optical properties of two or more major minerals (Stöffler et al., 2018). For shergottites, these minerals are plagioclase, pyroxene, and olivine, with the latter restricted to olivine-phyric (porphyritic) shergottites. More advanced analytical equipment such as scanning electron microscopy (SEM), transmission electron microscopy (TEM), and Raman spectroscopy are used to place further constraints on the pressure-temperature-time history of an impact event by identifying mineral transformations, textures, and relationships (Stöffler et al., 2018; Walton et al., 2014; Sharp et al., 2019).

### 2.1.2 Shock Metamorphism and Martian Meteorite Source Craters

Shock metamorphism in shergottites is associated with the impact event that ejected them from the martian near surface (Stöffler et al., 2018). Constraining shock conditions, specifically the pressure and temperature conditions and dwell time, of a specific meteorite can constrain launch conditions, which in turn may be used to estimate the size of the source crater. A meteorite's dwell time is the time during a shock event where the bulk rock pressure is >1 GPa (Bowling et al., 2020). Dwell time, ejection depth, and ejection velocity are some of the other possible variables for equations relating to launch conditions (Bowling et al., 2020; Artemieva and Ivanov, 2004). High resolution numerical models input these variables to estimate the size of the source crater (Bowling et al., 2020). A model size of a meteorite's source crater, coupled with remote sensing observations, can help to link meteorites to specific locations on the martian surface. Only a select few martian meteorites have had their launch conditions constrained for the process of narrowing down source crater size (discussed further in Chapter 3). Expanding the suite of martian meteorites with constrained launch conditions, through a comprehensive study of their shock characteristics, will increase the number of suitable samples for source crater determination. These studies are a necessary step to refine the approach and realize sources for a multitude of unique martian meteorites – or equally, to group distinct martian meteorites into suites of samples that were ejected from the same impact event ("launch pairs").

The only tentative martian samples with a known source site are those that are set to be returned as part of the Mars Sample Return (MSR) campaign (Beaty et al., 2019). However, the samples involved with the MSR campaign are representative of a different petrologic history than the current martian meteorite suite (Beaty et al., 2019; Udry et al., 2020). Linking a martian meteorite to its source crater will significantly increase its scientific value. In this study, I conducted a detailed survey of shock deformation and transformation effects recorded in 13 shergottite meteorites that have not previously been characterized in detail using optical microscopy, SEM, and Raman spectroscopy. The surveyed shock effects are used to constrain P-T conditions experienced by the meteorites when compared with the results of shock-recovery experiments. Relevant features of each of these 13 samples are given in Table 2.2 which compiles information on classification, mineralogy, composition, and ages.

**Table 2.2.** Overview of the meteorites selected for this study.

| Meteorite Name | Classification[1] | Fall / Find | Major Minerals[2] | Minor and Accessory Minerals | Texture | Crystallization Age (Ma) | CRE age (Ma) |
|---|---|---|---|---|---|---|---|
| JaH 479 | Shergottite (Enriched Mafic Diabasic) | 2008 Find | Pyroxene (45%), plagioclase (35%) | Olivine, ilmenite, silica, orthoclase, apatite, merrillite, zircon, pyrrhotite, troilite | Coarse-grained subophitic | n.d. | 2.1 ± 0.2 |
| KG 002 | Shergottite (Enriched Mafic Diabasic) | 2010 Find | Pyroxene (37%), plagioclase (48%) | Titanomagnetite, ilmenite, chlorapatite, merrillite, Fe-sulfides, fayalitic olivine, silica, baddeleyite | Coarse-grained ophitic to subophitic | 395 ± 240 | n.d. |
| NWA 2046 | Shergottite (Depleted Permafic Olivine-Orthopyroxene-Phyric) | 2003 Find | Olivine, pyroxene, plagioclase | Olivine, Ti-chromite, chromite, ilmenite, Cr-ulvöspinel, pyrrhotite, merrillite, chlorapatite | Porphyritic | n.d. | 1.1 ± 0.2 |
| NWA 2626 | Shergottite (Depleted Permafic Olivine-Orthopyroxene-Phyric) | 2004 Find | Pyroxene, olivine, plagioclase | Ti-chromite, chromite, merrillite, ilmenite, ulvöspinel, pyrrhotite | Porphyritic | n.d. | 1.1 ± 0.2 |
| NWA 6162 | Shergottite (Depleted Permafic Olivine-Phyric) | 2010 Find | Olivine, pyroxene, plagioclase | Ti-chromite, pyrrhotite, merrillite | Porphyritic | n.d. | 1.1 ± 0.1 |
| NWA 7635 | Shergottite (Depleted Mafic Olivine-Plagioclase-Phyric) | 2012 Find | Pyroxene, plagioclase | Titanomagnetite, pyrrhotite, ilmenite | Porphyritic | 2403 ± 140 | 1.3 ± 0.1 |
| NWA 10299 | Shergottite (Enriched Mafic Fine-Intergranular) | 2015 Find | Pyroxene (62%), plagioclase (29%) | Titanomagnetite, ilmenite, merrillite, apatite, Fe-sulfides, olivine, baddeleyite, silica | Coarse-grained subophitic | n.d. | n.d. |
| NWA 11057 | Shergottite (Enriched Mafic Diabasic) | 2016 Find | Pyroxene (66%), plagioclase (24%) | Ulvöspinel, ilmenite, chlorapatite, merrillite, pyrrhotite, baddeleyite | Medium-grained | n.d. | n.d. |
| NWA 11073 | Shergottite (Enriched Mafic Diabasic) | 2016 Find | Pyroxene (65%), plagioclase (29%) | Ulvöspinel, ilmenite, chlorapatite, merrillite, pyrrhotite, baddeleyite | Medium-grained | n.d. | n.d. |
| NWA 11255 | Shergottite (Enriched Mafic Aphyric) | 2017 Find | Pyroxene (60%), plagioclase (32%) | Titanomagnetite, ilmenite, pyrrhotite, merrillite, apatite, baddeleyite | Medium-grained | n.d. | n.d. |
| NWA 11955 | Shergottite (Enriched Permafic Gabbroic) | 2018 Find | Olivine, pyroxene, plagioclase | Ti-chromite, ilmenite, merrillite, chlorapatite, pyrhotite, baddeleyite | Inequigranular gabbroic | n.d. | n.d. |
| NWA 12262 | Shergottite (Enriched Mafic Diabasic) | 2018 Find | Pyroxene (45%), plagioclase (40%) | Fe-Ti oxides, pyrrhotite, apatite, merrillite, fayalitic olivine, baddeleyite | Medium-grained diabasic | n.d. | n.d. |
| NWA 12919 | Shergottite (Enriched Mafic Fine-Intergranular) | 2019 Find | Pyroxene (56%), plagioclase (30%) | Titanomagnetite, ilmenite, merrillite, chlorapatite, Fe-sulfides, olivine, baddeleyite | Medium-grained | n.d. | n.d. |

**Notes:** [1]classification from International Meteorite Collectors Association (IMCA) based on the scheme outlined by Walton et al. (2012); [2]percentages of major minerals are modal abundances from Sheen et al. (In Review).; n.d. = no data

## 2.2 Samples and Analytical Methods

A total of 14 polished thin sections representing 13 individual meteorites were selected for this study. All 14 thin sections were scanned under transmitted plane polarized and cross polarized light at the University of Alberta’s Department of Earth and Atmospheric Sciences’ Digital Imaging Facility (DIF) using a Nikon Coolscan 5000 & 9000 at 4000 dots-per-inch (dpi) resolution. The resultant scans provided an overview of the entire thin section, which served as a base map to locate areas of interest, including shock veins and shock melt pockets. One polished thin section of each meteorite was initially investigated under transmitted and reflected light microscopy using a standard petrographic microscope equipped with 5X, 10X, 20X, 50X, and 100X objective lenses. The thin sections were observed under plane polarized and cross polarized light to investigate shock deformation features including undulatory extinction, mosaicism, planar fractures, mechanical twinning, and planar deformation features, to identify regions of localized melting (shock melt pockets and shock veins), and to assess the structural state of plagioclase (crystalline versus amorphous). Areas of interest and microtextures were characterized in detail by backscattered electron (BSE) imaging using a Zeiss Sigma 300 VP field emission scanning electron microscope (FESEM) at the University of Alberta. BSE images were acquired at a working distance of ~7.0 mm with a 20 kV accelerating voltage and Si diode detector. This FESEM is equipped with a Bruker energy dispersive X-ray spectroscopy (EDS) system containing dual silicon drift detectors each with an area of 60 mm$^2$ and a resolution of 123 eV. The composition of individual grains was measured in EDS spot mode while EDS maps were acquired to assess mineral assemblages, textures, and relationships. BSE images were used to locate individual minerals and textures of interest for phase identification using a laser micro-Raman spectrometer at MacEwan University. Raman spectra were acquired in spot mode using a Bruker SENTERRA instrument, which enables sample viewing in reflected or transmitted light. A 100X objective was used to focus the 532nm line of an Ar$^+$ excitation laser beam to an ~1 µm spot size. A laser power of 20 mW was used. The spectrum was acquired as three-10s exposures, which were then stacked to achieve the final spectrum. Repeat spectra were acquired from individual areas to ensure that the spectrum was reproducible. Backgrounds of the spectra were graphically reduced and plotted using the Spectragryph optical spectroscopy software [F. Menges "Spectragryph - optical spectroscopy software", Version 1.2.12, 2019, http://www.effemm2.de/spectragryph/]. Minerals exhibiting strong fluorescence, or those that are not Raman active, could not be identified using this instrument and were not analyzed further. Peak positions in the Raman spectrum of individual phases were used to identify high-pressure minerals by comparing the spectral signature to published standards. These standards include the online RRUFF database (Lafuente et al., 2016) and published Raman spectra (e.g. Ma et al., 2016; Dymshits et al., 2015; Ma, 2018; Bläß, 2013; Dera et al., 2002; Miyahara et al., 2013; Van de Moortèle et al., 2007; Ma et al., 2015).

## 2.3 Results

### 2.3.1 Shock Deformation and Transformation effects – Optical Microscopy

All of the studied samples contain the solidified products of shock melt in the form of isolated pockets and/or veins cutting across igneous host rock (Fig. 2.1). General observations of the entire suite of studied samples are presented here; specific results are tabulated in Table 2.3.

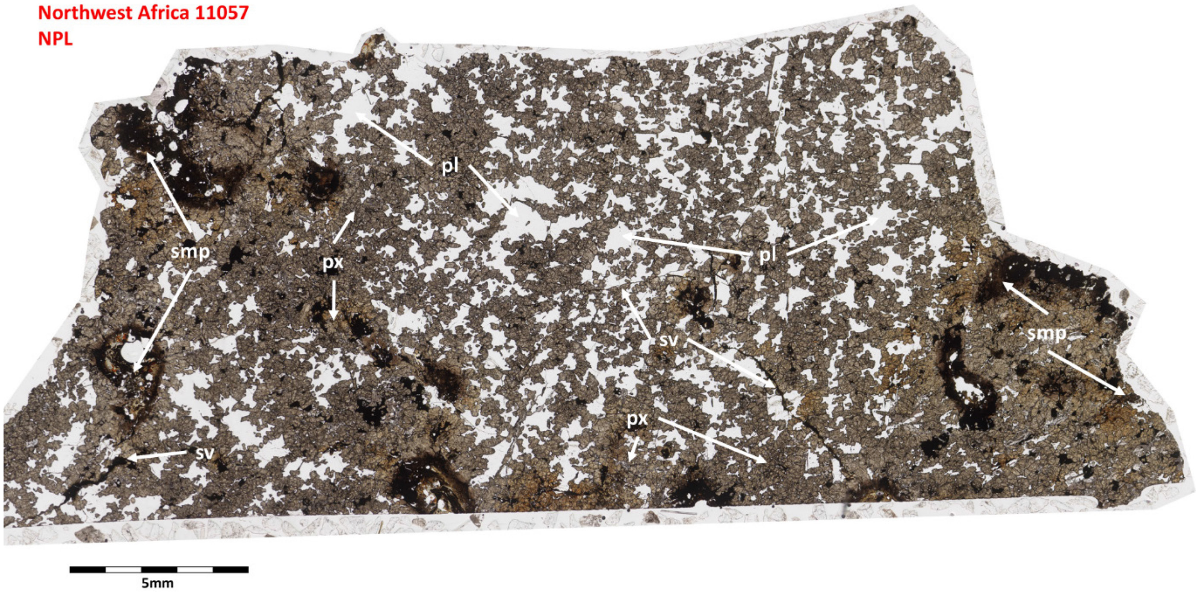

**Fig. 2.1.** Transmitted light image of the NWA 11057 thin section. NWA 11057 is a typical example of the meteorites in this study showcasing opaque shock melt in the form of shock melt pockets (smp) and shock veins (sv). The plagioclase (pl) has been completely transformed to glass and pyroxene (px) is crystalline, but shock deformed. Transmitted and cross polarized light images of all the thin sections in this study can be viewed in Appendix A.

The shock melt pockets are heterogeneously distributed throughout the thin sections and range from a few micrometers (e.g. KG 002) to centimeters (e.g. NWA 10299) in size and are rounded to amoeboid in shape (Fig. 2.1). Shock veins are observed as thin, glassy, black to brown veins that typically consist of a primary vein, upwards of 200 µm in width, that splits into thinner branches that spread outwards from the primary vein or as anastomosing patterns. In some cases, the shock veins are associated with noticeable offset and displacement of the igneous minerals in the host rock (e.g., JaH 479, NWA 12262; Fig. 2.2). However, this displacement is not observed in all samples. NWA 11057 has shock veins that crosscut the entire thin section but do not create any visible offset in the host rock minerals surrounding the shock vein in the two-dimensional space of the thin section.

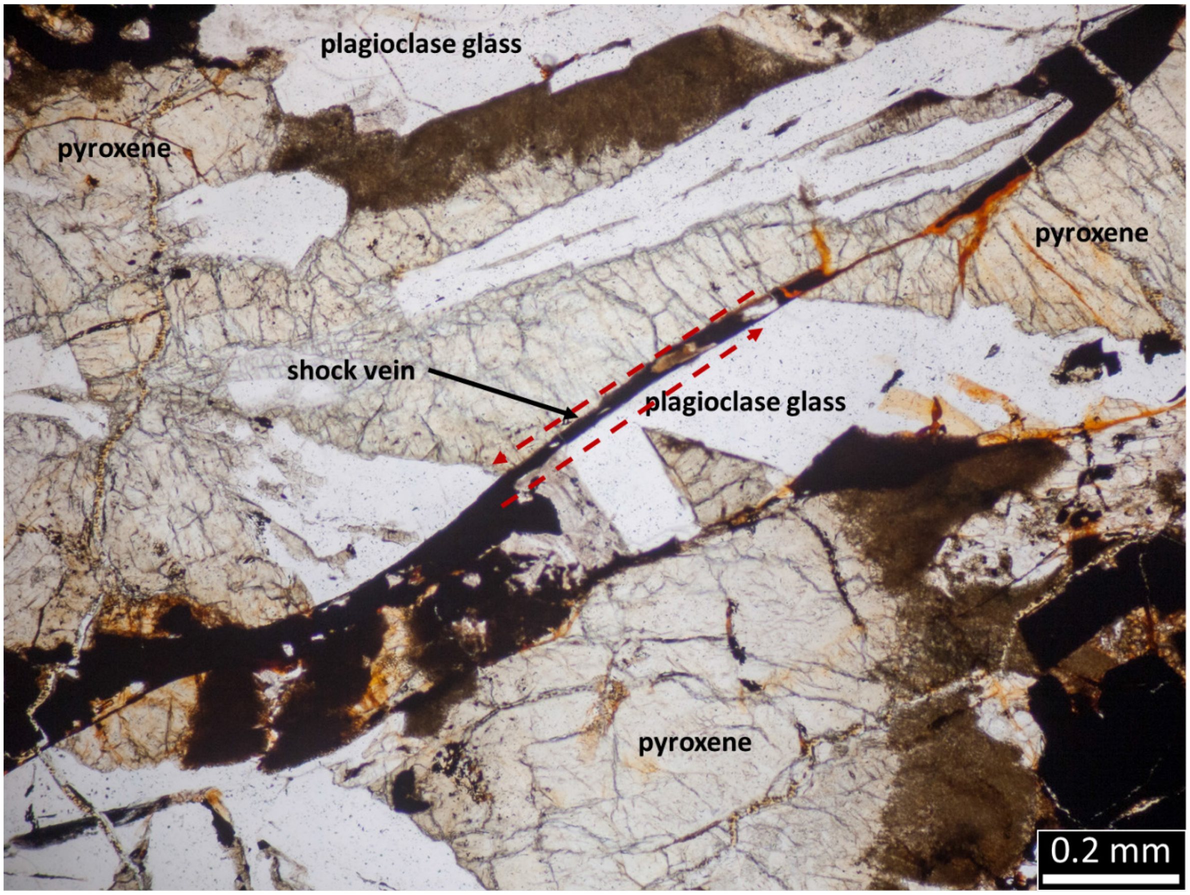

**Fig. 2.2.** Plane polarized light (PPL) image of JaH 479 showing displacement produced by a shock vein. The red lines show the approximate displacement of plagioclase.

Pyroxene crystals exhibit planar fractures and varying degrees of mosaicism (weak to strong) in all samples (Fig. 2.3, Fig. 2.4). Sets of planar fractures cut across the entirety of grains in some cases and are restricted to the interior portions of grains in other cases; the former is more common in this sample suite. In NWA 2046, NWA 2626, NWA 6162, NWA 10299, NWA 11255, and NWA 11955, the pyroxene crystals display mechanical twins (Fig. 2.5). The twins are deformed into several different patterns and arrangements including wave-like and chevron patterns, and sheared twins.

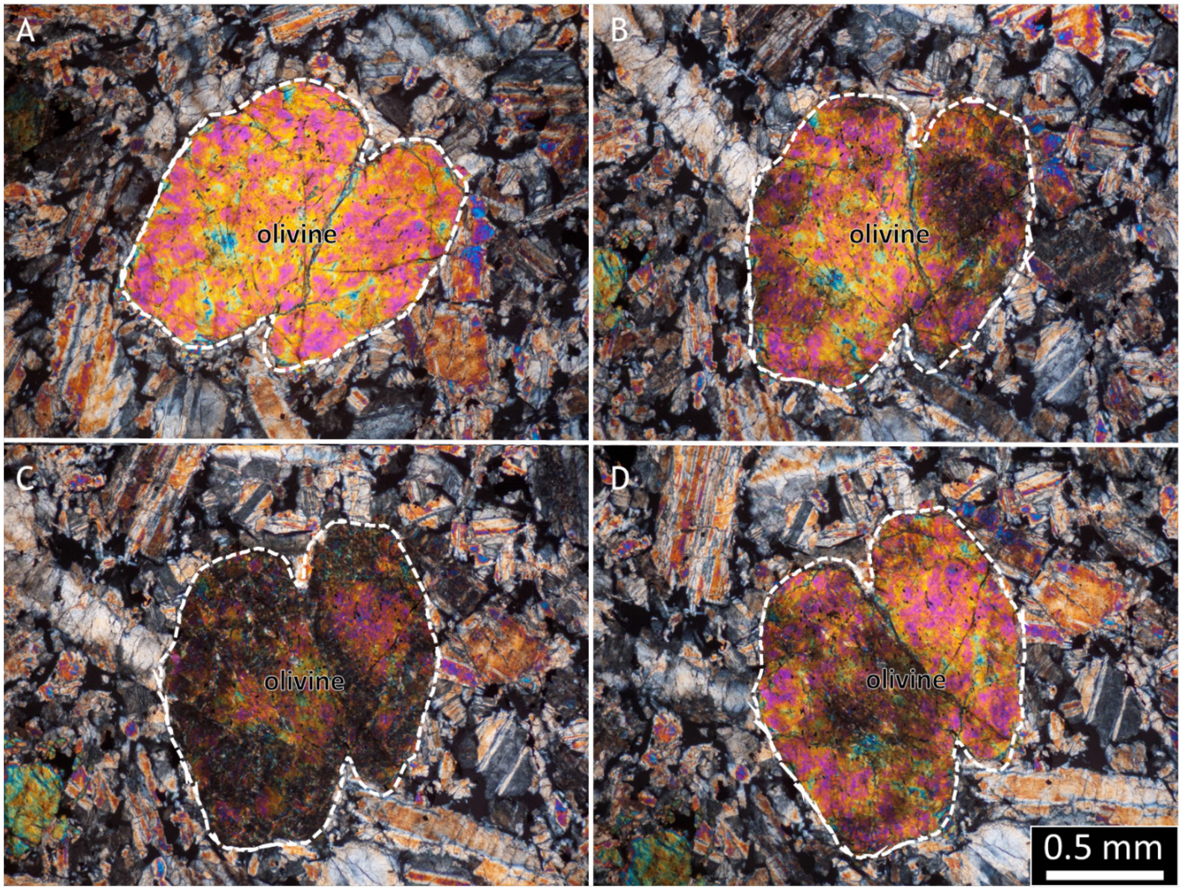

**Fig. 2.3.** Strong mosaicism observed in an olivine phenocryst, in a cross polarized light (XPL) view of NWA 11073. Frames a, b, c, d show small domains of the olivine grain going extinct at different orientations as the grain is rotated counter clockwise.

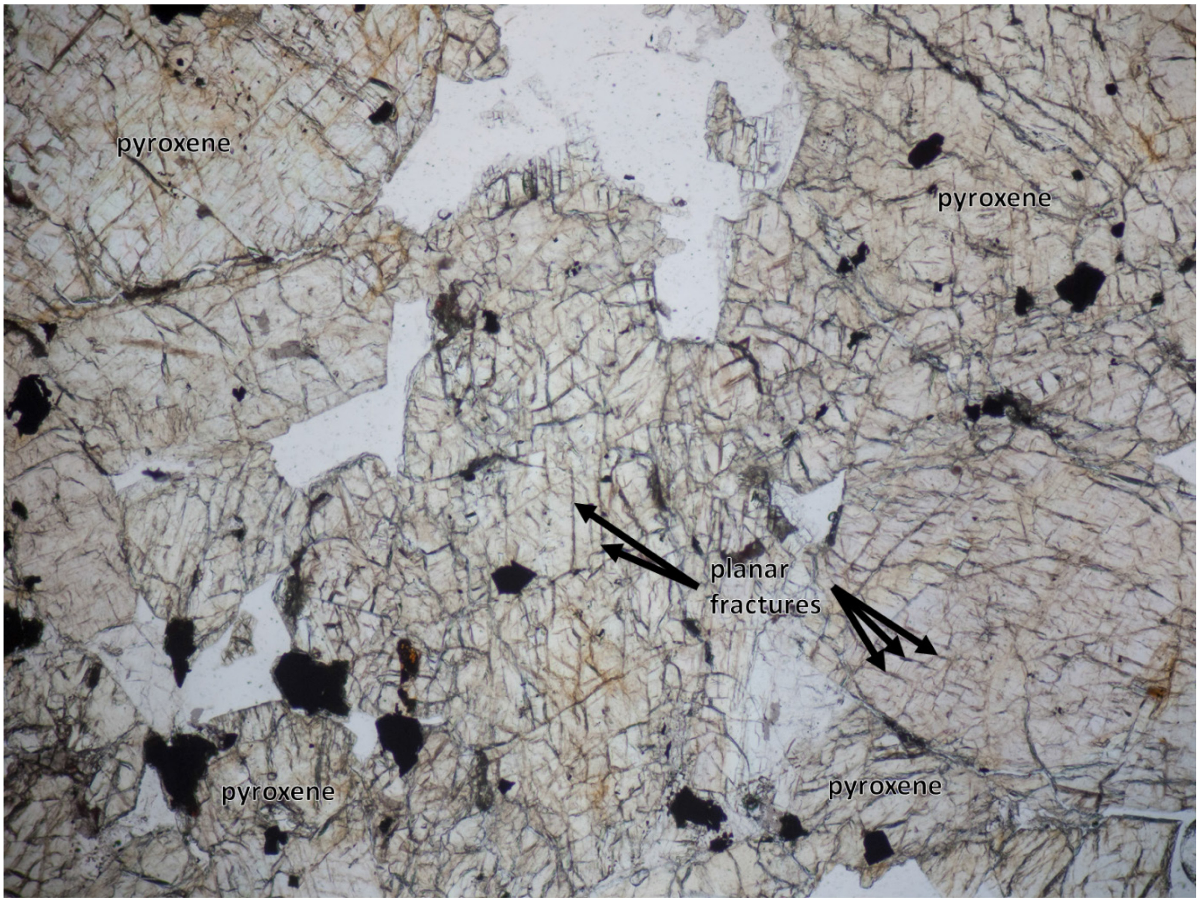

**Fig. 2.4.** Sets of planar fractures observed throughout pyroxene in NWA 11255. Unlike cleavage, the planar fractures observed in pyroxene grains are not uniform and do not cut across the entire crystal. Measurements of the orientation of planar fractures are needed to confirm they are not cleavage planes in cases where the fracture cuts across the entire crystal.

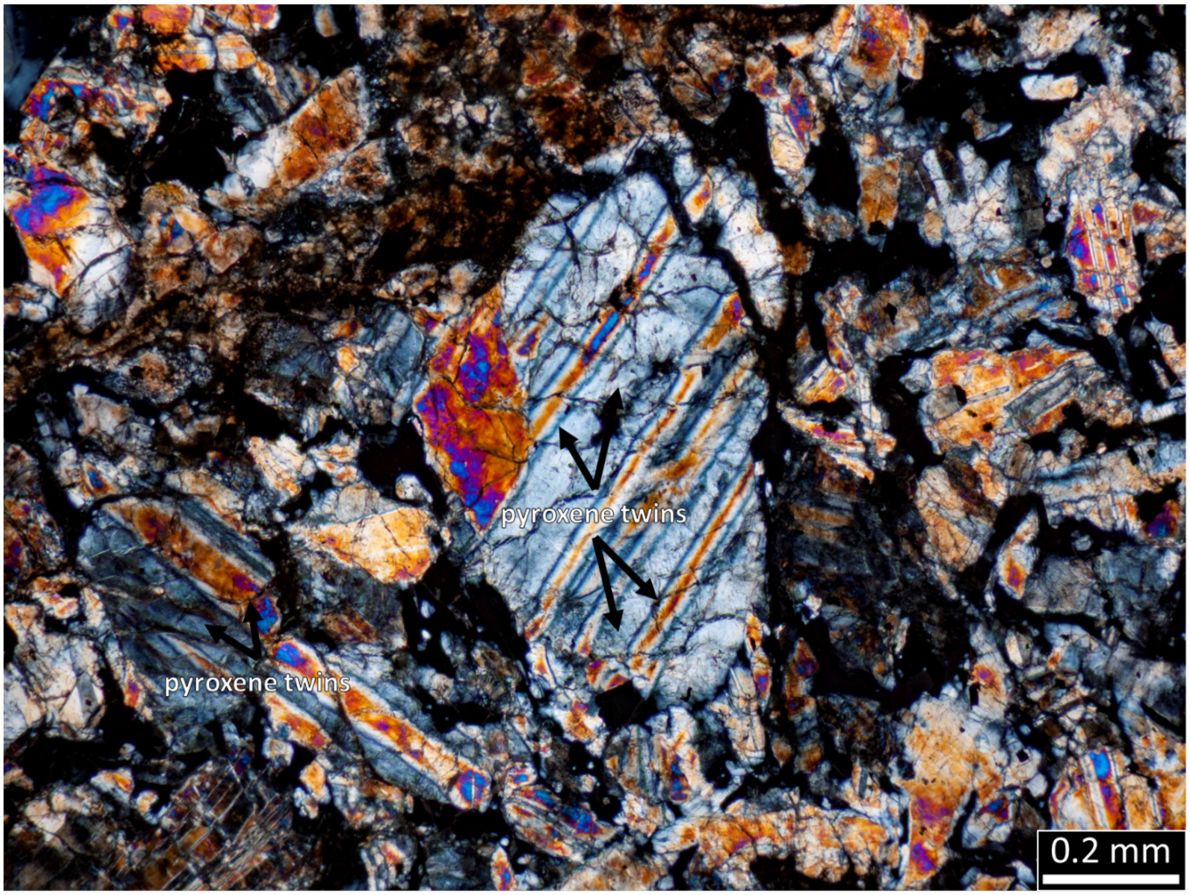

**Fig. 2.5.** Mechanical polysynthetic twinning produced in pyroxene grains of NWA 2626 viewed in XPL.

Plagioclase was optically assessed to determine its structural state – in all the studied meteorites, this mineral has been completely transformed to glass as indicated by its isotropic nature (Fig. 2.6). Irregular fractures extend from the grain boundary of this glass into neighbouring igneous minerals. The glass was characterized by scanning electron microscopy (section 2.3.2) to assess whether it is a diaplectic (maskelynite) or normal glass.

Olivine is abundant in NWA 2046, NWA 6162, and NWA 11955 (Table 2.2). In all three samples, olivine phenocrysts exhibit planar fractures and mosaicism (Fig. 2.3). Planar fractures are generally parallel but may deviate by up to 15° within a single grain in samples such as NWA 11955, and appear in multiple orientations, including at right angles to each other, in samples such as NWA 11073. In both cases, the planar fractures cut across the entire grain. Spacing of the sets of planar fractures appears loosely correlated to crystal size with larger crystals displaying sets that are 0.1-0.2 mm apart and smaller crystals displaying sets that are tens of micrometers apart. Large olivine phenocrysts have been observed to display both types of widely and thinly spaced planar fractures. The olivine in

NWA 2046 is stained dark brown, unlike NWA 6162 and NWA 11955 where this mineral is clear and colourless (Fig. 2.7).

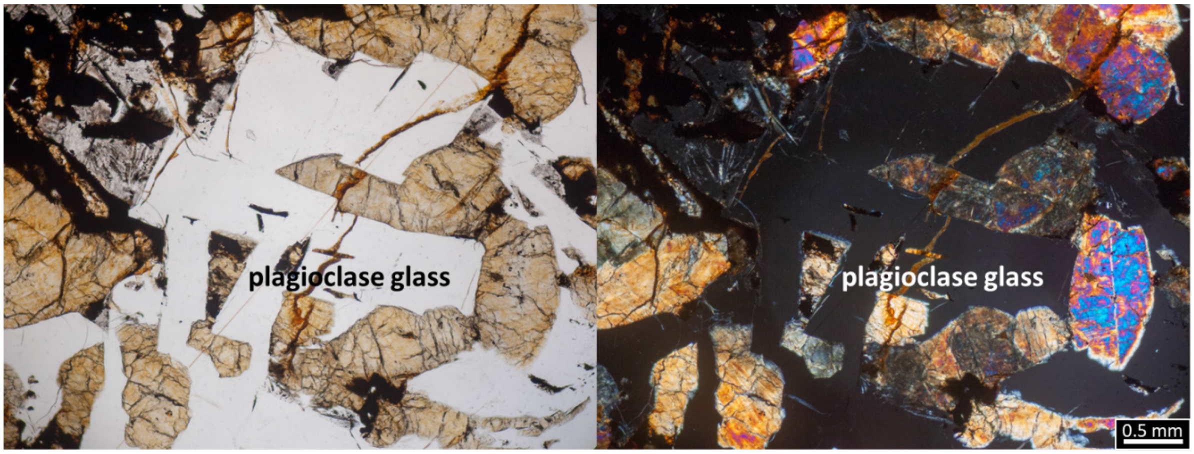

**Fig. 2.6.** PPL (left) and XPL (right) images of the same area in NWA 12262 showing the isotropic nature of former plagioclase indicated by complete extinction under XPL.

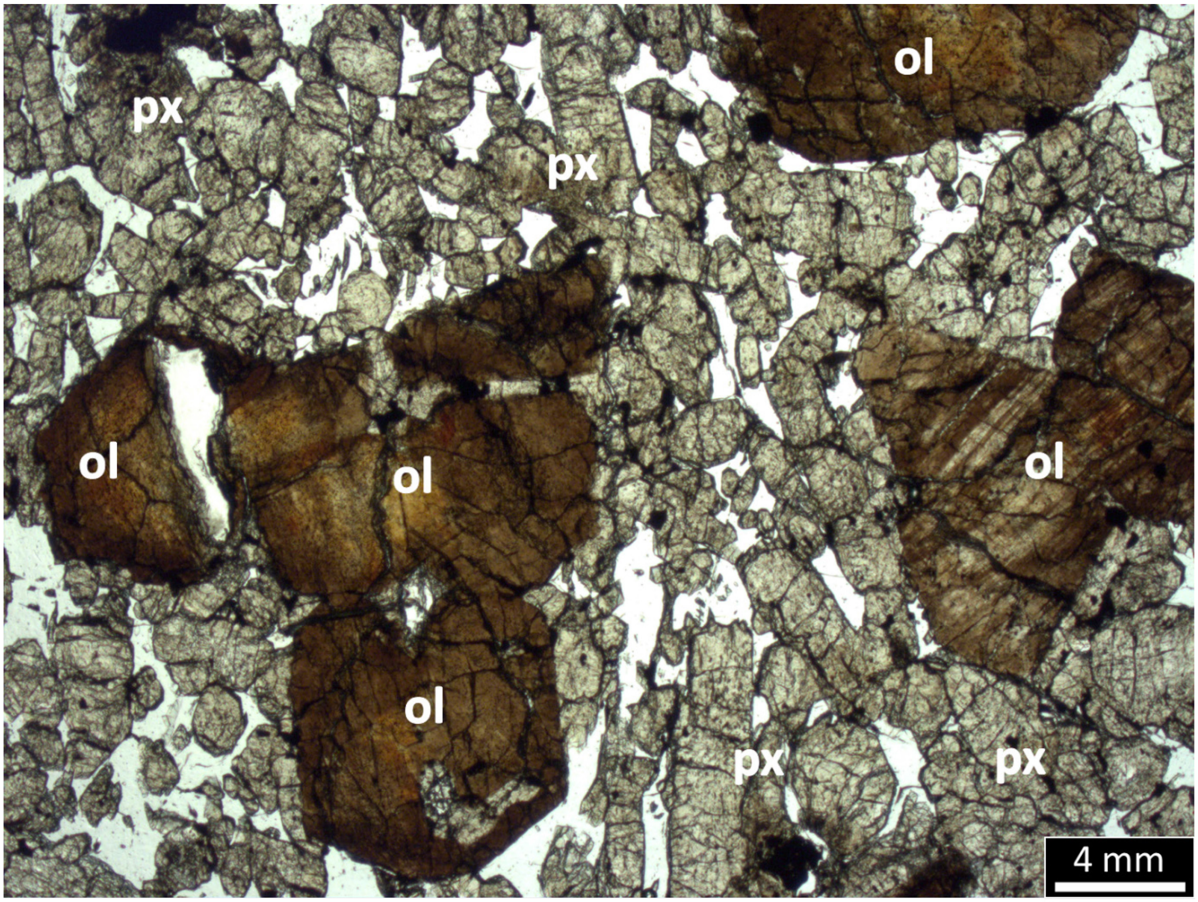

**Fig. 2.7.** Brown-stained olivine (ol) and pyroxene (px) in NWA 2046 viewed under plane polarized light. The colourless grains are isotropic plagioclase.

### 2.3.2 Shock Transformation - Scanning Electron Microscopy

Scanning electron microscopy, in BSE imaging mode, was used to characterize the microtextures of plagioclase glass and silica in the bulk rock and the minerals associated with shock veins and shock melt pockets. These latter minerals include igneous plagioclase and olivine in direct contact with shock melt – along margins or entrained as fragments – and minerals within the shock melt matrix.

Samples JaH 479, KG 002, NWA 12919, NWA 2046, NWA 2626, NWA 6162, NWA 7635, NWA 11057, NWA 11073, NWA 11255, NWA 11955, and NWA 12262 show complete transformation of plagioclase to a glass based on optical properties. BSE images confirm that this glass is maskelynite, as it retains the crystal habit of the precursor plagioclase, is smooth and unfractured (Fig. 2.8), and does not show any microtextures attributed to melting. In contrast, the former plagioclase in NWA 10299 is a schlieren-rich glass with flow structures and containing vesicles (Fig. 2.9). These vesicles are roughly spherical and range in size from 10s to 100s of micrometres. BSE images confirm the presence of seifertite, a silica polymorph, in JaH 479, NWA 10299, and NWA 11255 (Fig. 2.10). The $SiO_2$-rich composition was confirmed by EDS analyses (>98 wt% $SiO_2$). Seifertite grains are enclosed by maskelynite and exhibit a crosshatch pattern of alternating bright and dark lamellae in BSE images. These silica grains are up to a few tens of micrometers in size while the individual lamellae are narrow (<0.5 μm), similar to those found in Shergotty (El Goresy et al., 2008). Fractures from the margins of seifertite radiate into enclosing maskelynite. This phase is extremely sensitive to the electron beam, with visible damage induced by acquiring BSE images and EDS spot analyses.

The products of shock melting are largely opaque in thin section, owing to their glassy or fine-grained nature. Samples NWA 2046 and NWA 6162 contain shock melt with a predominantly glassy, vesiculated matrix and blebs of Fe-sulphides. The glass exhibits a strong fluorescence using Raman that overwhelms the spectral signatures of fine-grained minerals that could therefore not be identified. Other meteorites contain shock melt with a microcrystalline matrix and are characterized further here. Minerals in the matrix of shock veins and shock melt pockets are predominantly silicates from EDS spot analyses, with compositions consistent with olivine, high-Ca pyroxene, and silica (~98 wt% $SiO_2$). These minerals exhibit a range of shapes including equant euhedral, spherical, bladed, dendritic, and skeletal and are embedded in a silicate glass. Grain sizes are typically in the 5 – 100 micrometers size range. Larger crystals (minimum 1 μm in size) are often zoned, observed as a change in greyscale from core to rim, although EDS spot analysis does not have the resolution required to characterize the zoning trends.

In the majority of meteorites, larger mm- to cm-size melt pockets exhibit a glassy, schlieren-rich, vesiculated centre with the degree of crystallinity (number of crystals per area) increasing toward the shock melt margin. Bladed crystals are observed in the shock melt pockets JaH 479 KG 002, and NWA 11073 in addition to spheres of Fe-sulphides and silica glass. Additionally, fragments of the host rock are incorporated into shock melt pockets and shock veins throughout the entire suite of samples. These fragments include both silicates and oxides and range in size from 5 µm to a few millimeters – a noticeably larger grain size than any of the minerals in the shock melt matrix. The shock melts in two meteorites - NWA 11255 and NWA 2626 - are discussed in detail below.

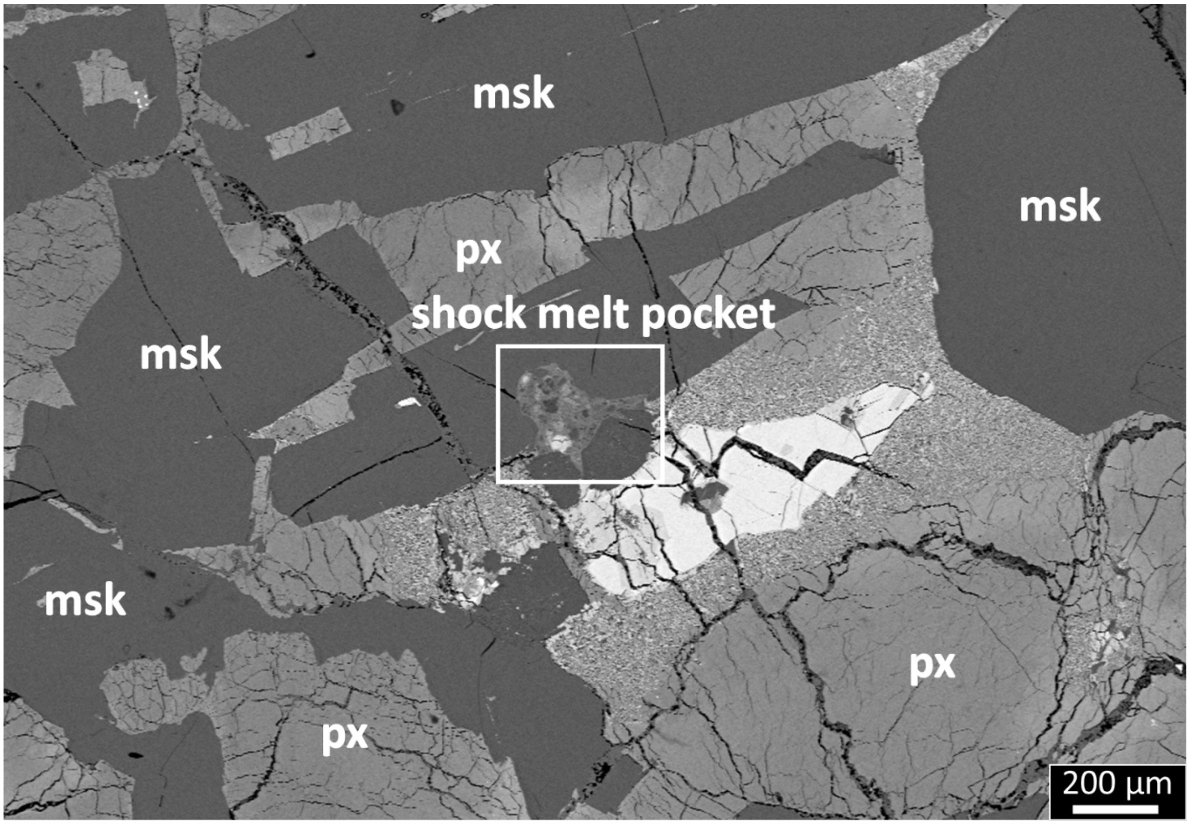

**Fig. 2.8.** Backscattered electron (BSE) image of KG 002 showing the preservation of plagioclase crystal habit in the form of a smooth, unfractured glass (maskelynite, msk) and heavily fractured pyroxene (px) in the host rock. The location of a shock melt pocket is shown by the white box.

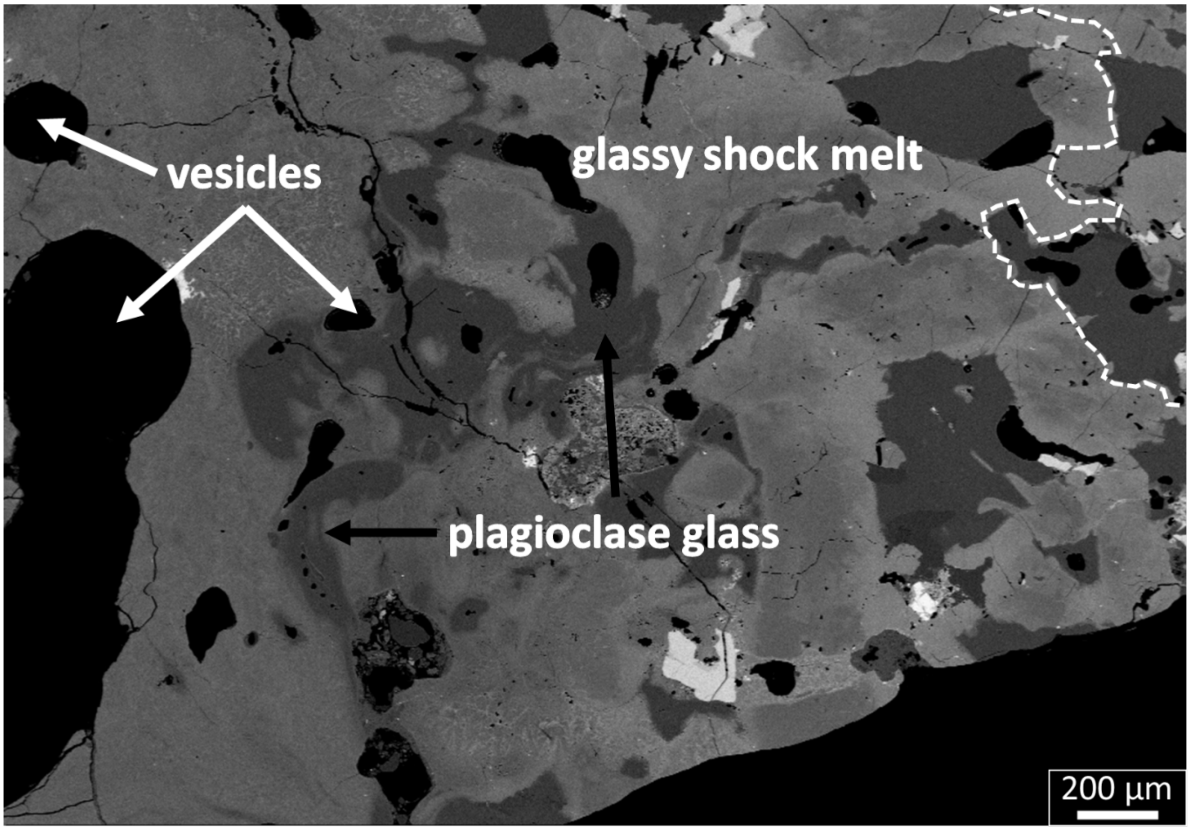

**Fig. 2.9.** BSE of quenched plagioclase glass and glassy shock melt in NWA 10299. The white dashed line shows the boundary between shock melt and host rock although the contact is gradational and this boundary is therefore approximate.

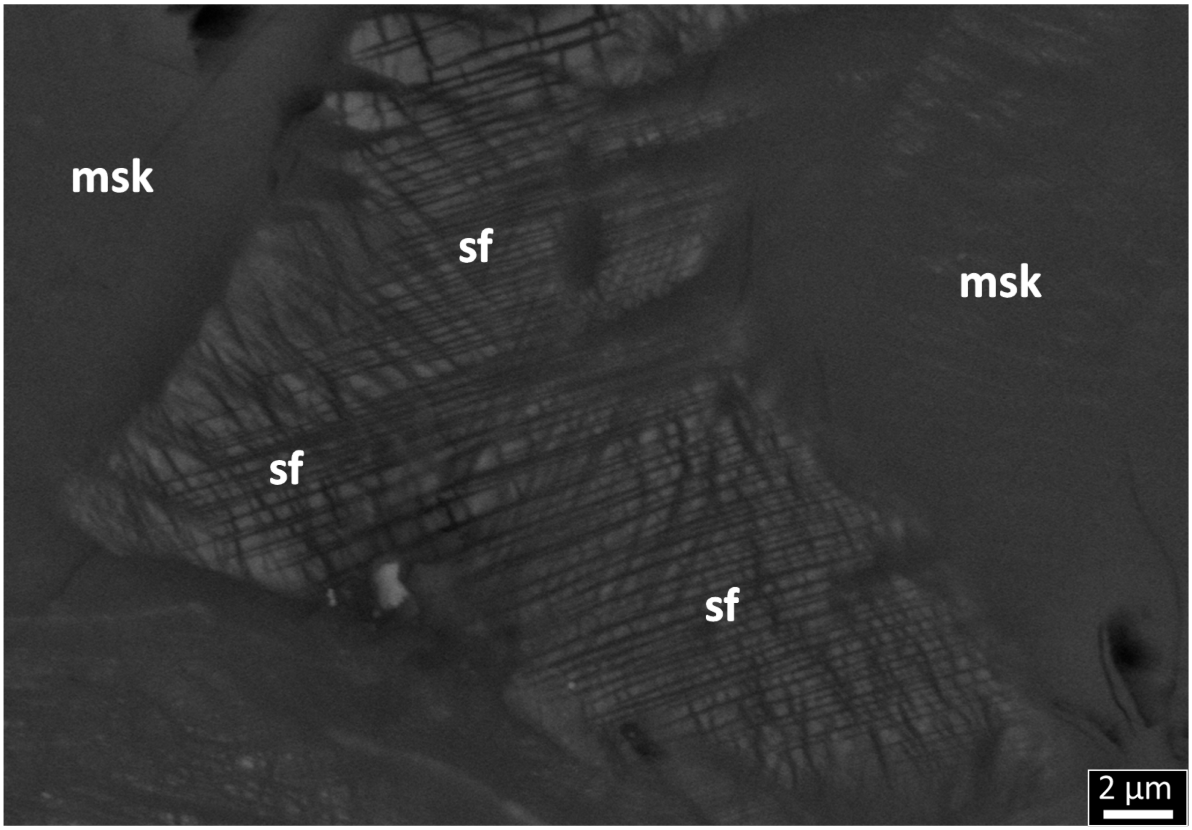

**Fig. 2.10.** BSE of the cross hatch pattern characteristic of seifertite (sf) surrounded by maskelynite (msk) in JaH 479.

NWA 11255 contains a shock vein that is ~0.3 mm at its widest crosscutting the entire thin section (Fig. 2.11). Large fractures up to 20 µm wide cut perpendicular across the vein (Fig. 2.11). Fractures that crosscut shock veins are not isolated to NWA 11255 and are found at least sporadically in the other meteorites containing shock veins in this study. In plane polarized light, the shock vein has a brownish-grey centre that becomes darker, approaching opacity, towards the margins. This change in shock vein colour from its centre to margin is correlated with a decrease in grain size as the shock vein margin is approached. The interior of the shock vein is composed primarily of Al- and Fe-rich zoned silicate grains with rounded crystal shapes. These grains are 0.1-3 µm in diameter, averaging ~2 µm at the vein centre, but are 0.1-0.5 µm size towards the vein margin and sub-micrometer within a few micrometers of the contact with the host rock. Raman spectroscopy was employed to identify these grains in the matrix of NWA 11255 shock veins (Section 2.2.3). The shock vein has a distinct, sharp contact with the adjacent igneous host rock.

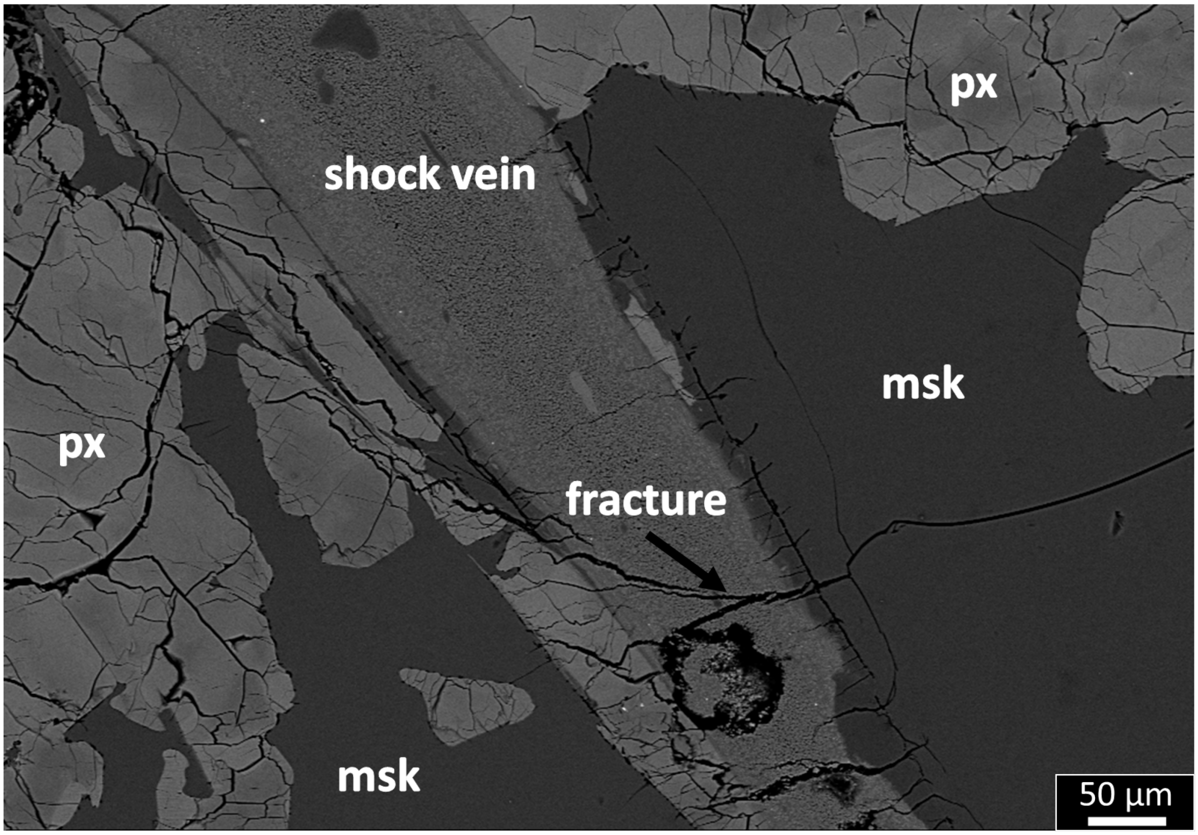

**Fig. 2.11.** BSE image of a prominent shock vein in NWA 11255. See text for details.

The studied thin section of NWA 2626 has a shock vein that is 100 µm at its widest and a series of microcrystalline shock veins (Fig. 2.12). Microcrystalline shock veins are internally zoned, with a fining of crystal sizes towards the margin, as described in NWA 11255. These shock veins crosscut the entire thin section, while micro-fractures are observed in entrained fragments of host rock minerals. Intermediate (tens of micrometers) to wide (millimeters) shock veins in NWA 2626, NWA 11255, and NWA 7635 have widths that vary across the length of the vein.

Transformation of igneous minerals along shock vein and shock melt pocket margins is observed as a change in texture and /or greyscale where the former igneous mineral is in direct contact with the shock melt. These transformations are observed in plagioclase and olivine where they border the shock melt margins or have been entrained as fragments in shock melt. Tissintite [$(Ca,Na,\square)AlSi_2O_6$] is identified in JaH 479, NWA 11057, and NWA 12262 based on textural characteristics that are identical to those described in the type specimen (Tissint) by Ma et al. (2015; Fig. 2.13) and confirmed as plagioclase composition by EDS spot analysis (CaO- and $Al_2O_3$-rich). Tissintite is documented in maskelynite grains that are in contact with shock melt, and also as individual grains within shock melt pockets; the latter are observed in former plagioclase fragments entrained within the shock melt and as crystals within the shock melt matrix. Dendritic aggregates of tissintite have a broad range in size depending on the amount of plagioclase incorporated into the shock melt from as small as a few micrometers upwards of a few millimeters. The rims formed in maskelynite along shock melt contacts are up to 100 µm wide (Fig. 2.13). The margins of olivine crystals bordering shock veins in NWA 7635 appear bright in BSE images indicating transformation. In BSE images, ringwoodite, the high-pressure olivine polymorph, can be delineated by a brighter greyscale (Fig. 2.17) attributed to the higher density of this mineral. EDS spot analyses do not show any appreciable difference in composition between the brighter rim and adjacent olivine. This olivine transformation is characterized further using Raman spectroscopy in section 2.3.3.

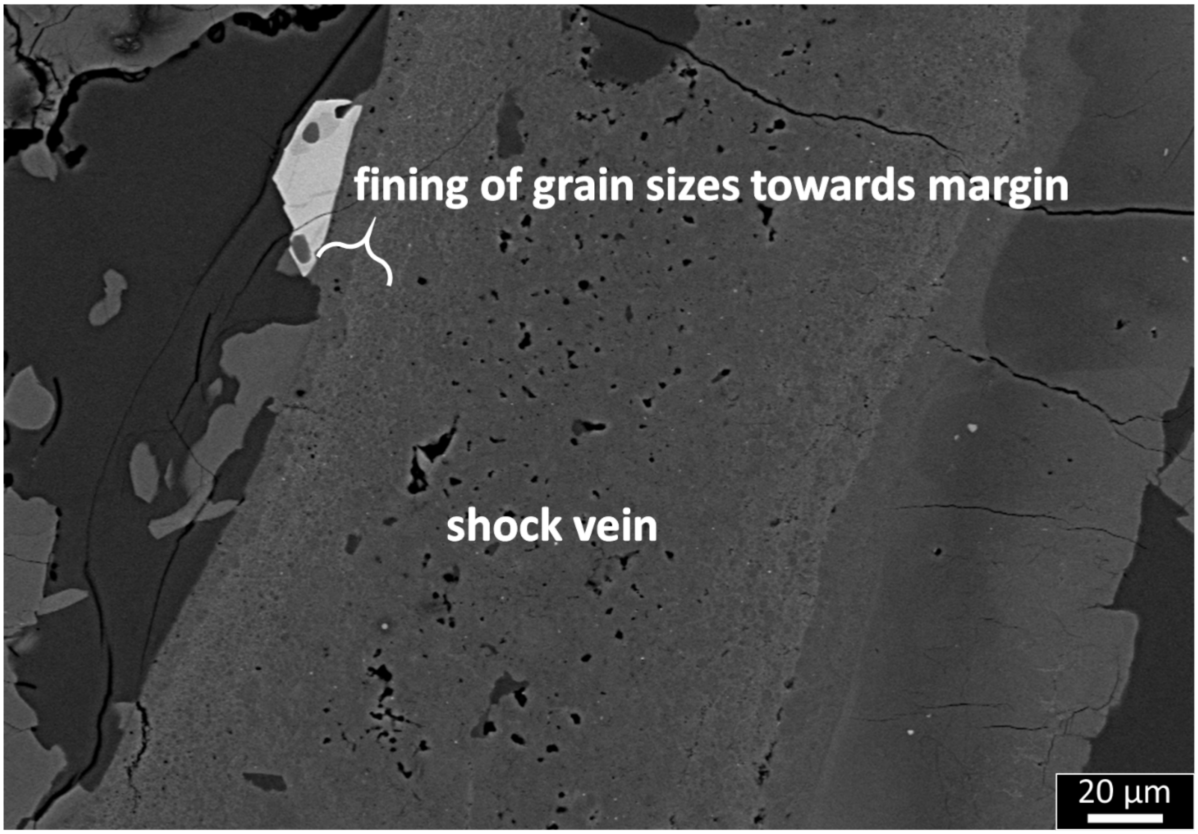

**Fig. 2.12.** BSE image of the most prominent shock vein and its boundaries in NWA 2626. Grains within the shock vein fine towards the margins and accompany many vesicles, which appear as black areas in the BSE image.

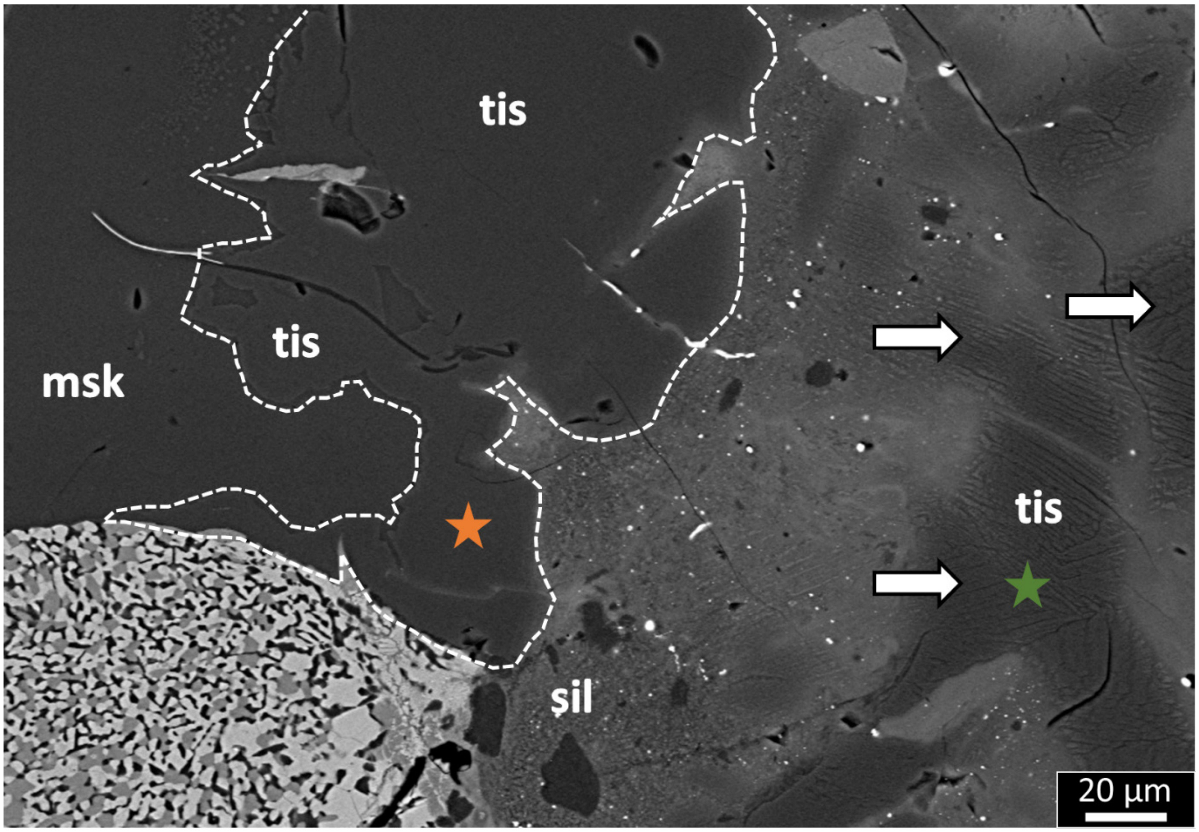

**Fig. 2.13.** Tissintite (tis) in JaH 479 shows two textural forms documented in the sample suite. The white dashed line shows a rim of tissintite in maskelynite (msk) where maskelynite is in contact with the shock melt. The white arrows show aggregates of tissintite found within the matrix of the shock melt.

### 2.3.3 Mineralogy of Shock Melt – Laser micro-Raman Spectroscopy

Minerals within the shock melt matrix or those formed by the transformation of neighbouring igneous minerals (along walls or as entrained fragments) are discussed in this section. NWA 2046, NWA 6162, NWA 11955, and NWA 12919 have predominantly glassy and fine-grained shock melt yielding a strong fluorescent background. For these samples, peaks in the Raman spectrum could not be resolved or were flat indicating Raman-inactive phases - these meteorites will not be discussed further in this section. In contrast, minerals analyzed in meteorites JaH 479, KG 002, NWA 2626, NWA 7635, NWA 10299, NWA 11057, NWA 11073, NWA 11255, and NWA 12262 yielded a Raman spectrum with sharp, distinguishable peaks and these results are presented here.

The Raman spectrum collected from individual grains in the matrix of shock melt pockets and veins yielded several distinct spectral signatures throughout this suite of meteorites. Pyroxenes, primarily clinopyroxenes, were found abundantly throughout all the study samples as identified by doublets at ~650-690 and ~990-1050 cm$^{-1}$ in the spectrum (Fig. 2.14). In JaH 479, NWA 11057, and NWA 12262, tissintite was confirmed with Raman peak positions similar to jadeite at 370 and 690 cm$^{-1}$. These peak positions match those from tissintite analyzed in the type specimen meteorite, Tissint, by Ma et al. (2015; Fig. 2.15). The bladed crystals were identified as stishovite by a single peak at 750 cm$^{-1}$ (Fig. 2.16), which is consistent with EDS spot analyses showing these grains to be almost pure $SiO_2$ (wt% oxides). Stishovite was confirmed in JaH 479, KG 002, and NWA 11073. Ringwoodite in NWA 7635, delineated as a bright rim in BSE images, was confirmed by peak positions at 670, 790, and 830 cm$^{-1}$ (Fig. 2.17). Dendritic olivine is found in the matrix of shock melt in NWA 2626 with intergrowths of pyroxene (Fig. 2.18).

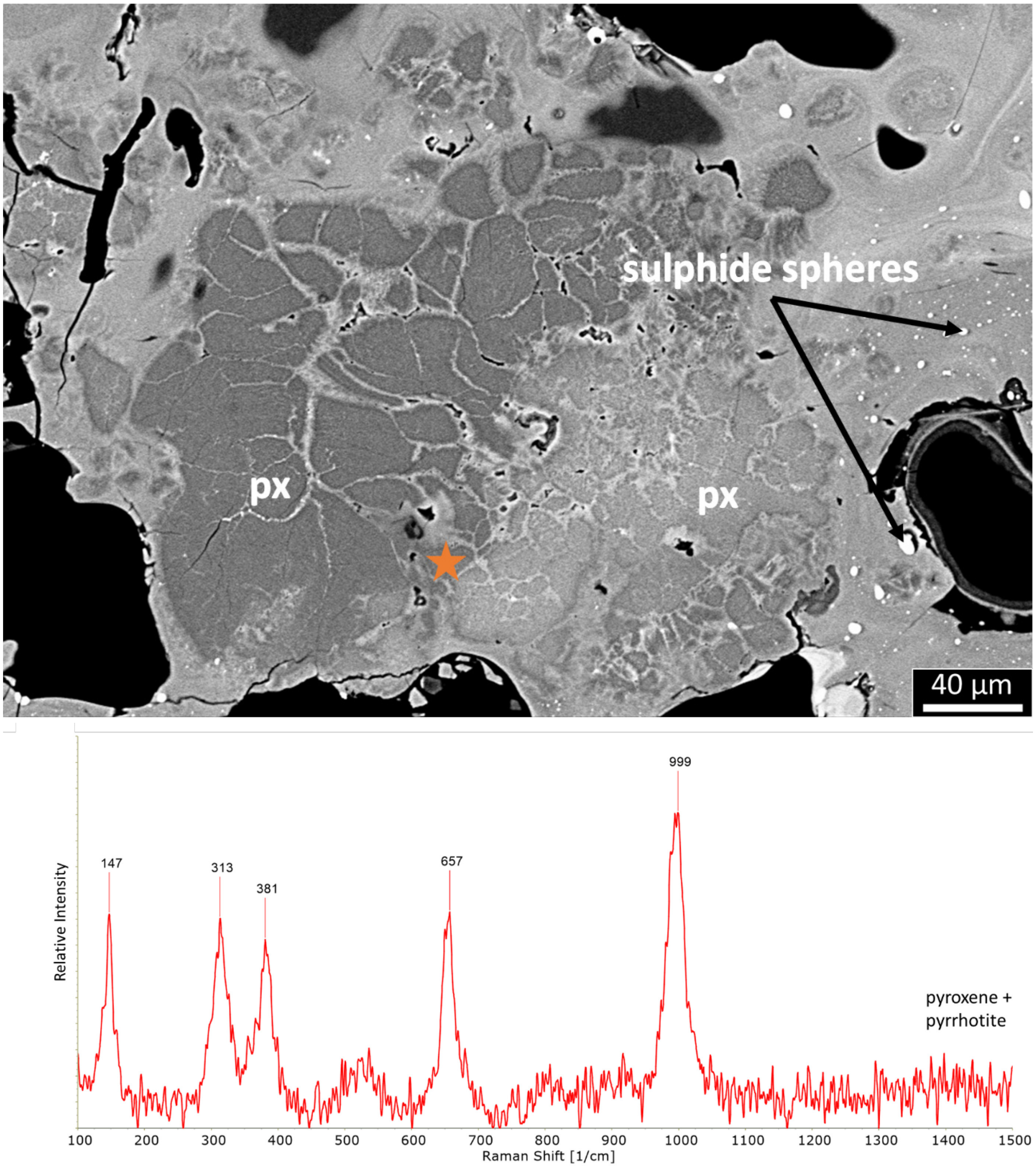

**Fig. 2.14.** BSE image of (px) and pyrrhotite in NWA 11073 shock melt. The red star approximates the location where the corresponding Raman spectrum was obtained.

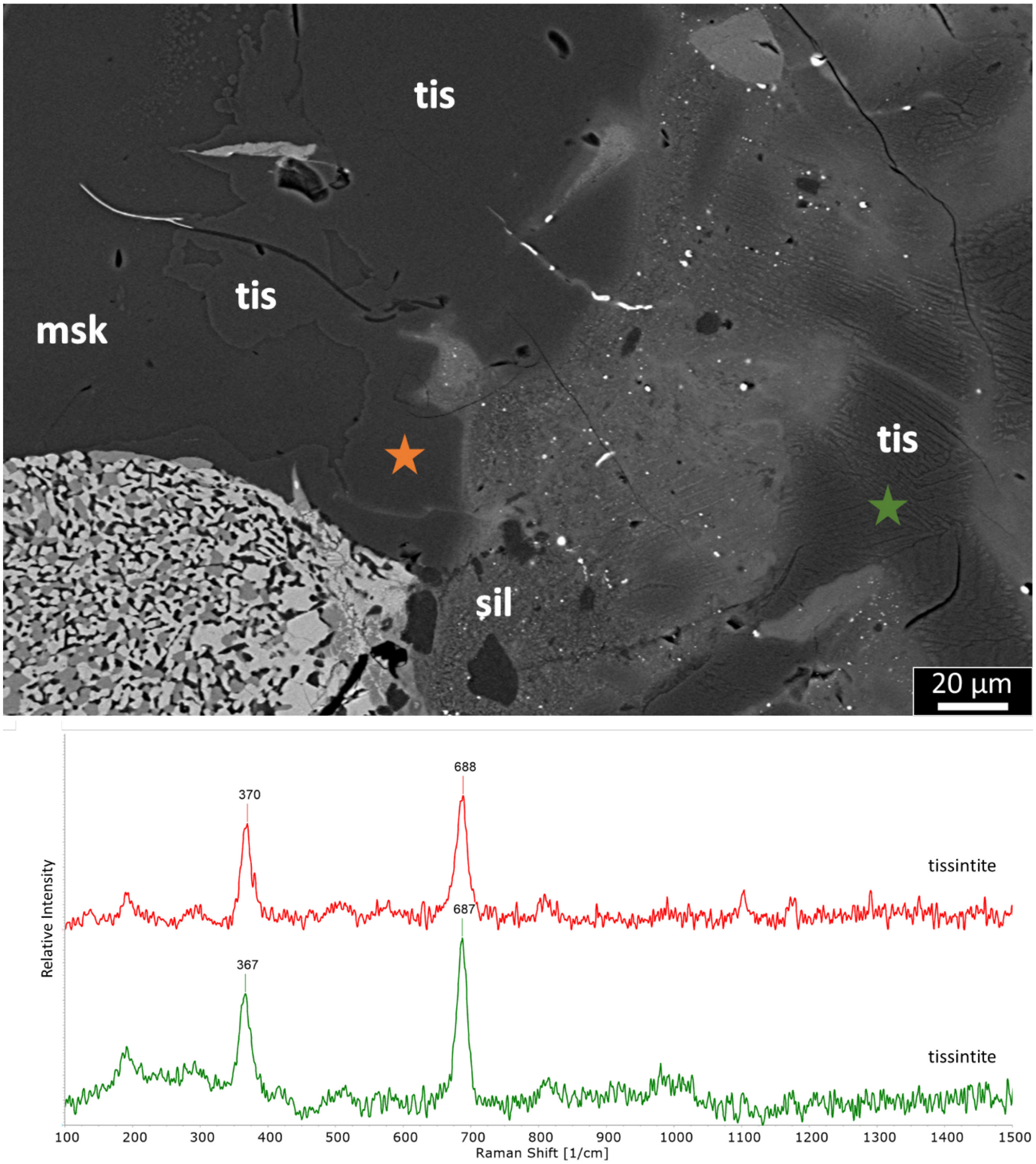

**Fig. 2.15.** BSE image of a shock melt pocket and the Raman spectrum of tissintite (tis) in JaH 479 (same area as shown in Fig. 2.13). The margin of maskelynite (msk) in direct contact with the shock melt pocket has transformed to tissintite. This shock melt pocket matrix is composed of a mixture of silicates (sil) and tissintite aggregates. The orange and green stars show the approximate location of individual Raman spot analyses and their corresponding colour-coded spectra. Tissintite is confirmed along shock melt margins (orange) and as dendritic or skeletal grains within the shock melt (green).

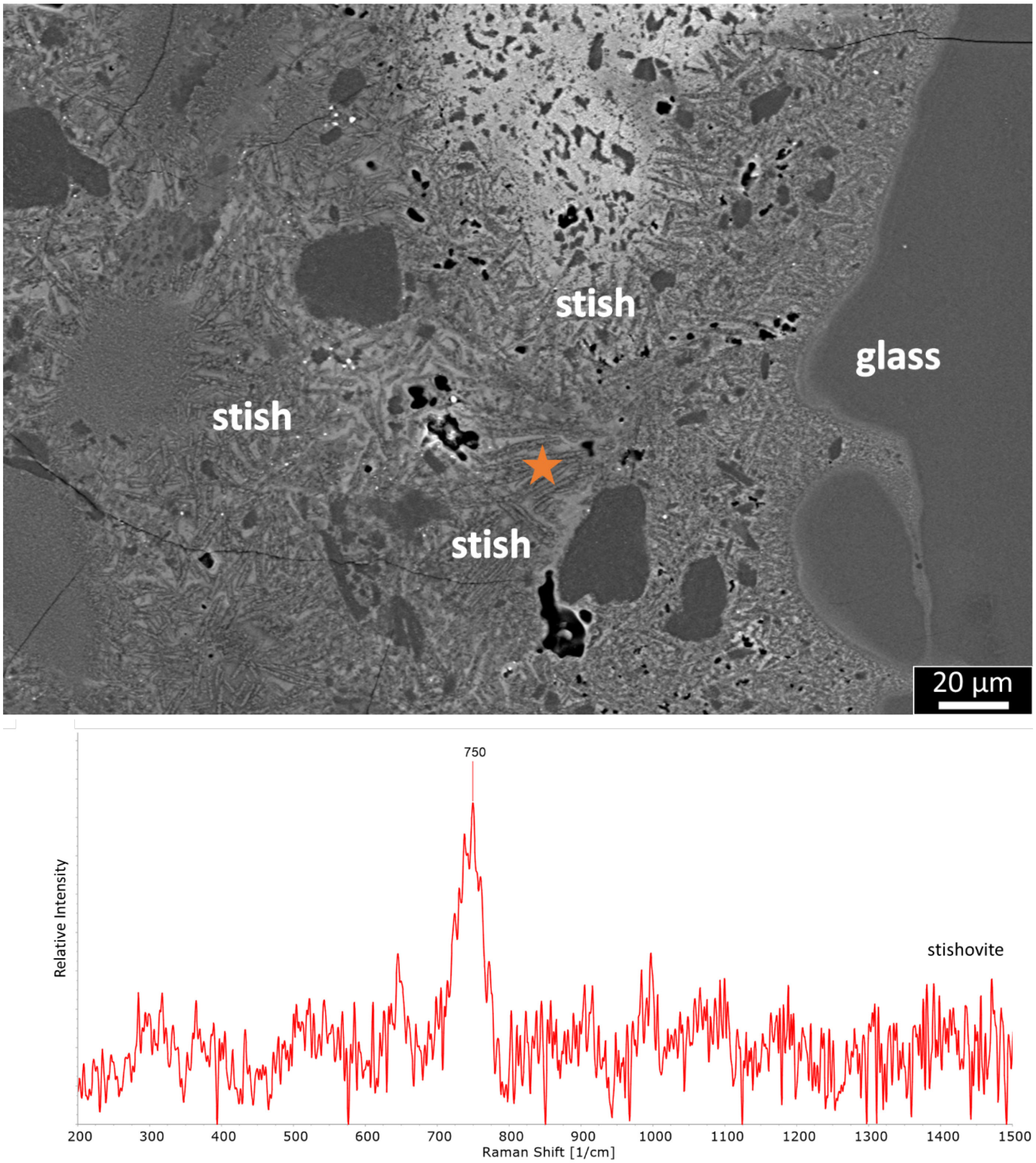

**Fig. 2.16.** BSE image of the matrix of a shock melt pocket in KG 002. The bladed crystals are silica (from EDS), confirmed to be stishovite by Raman spectroscopy. The red star indicates the location where the corresponding Raman spectrum was obtained.

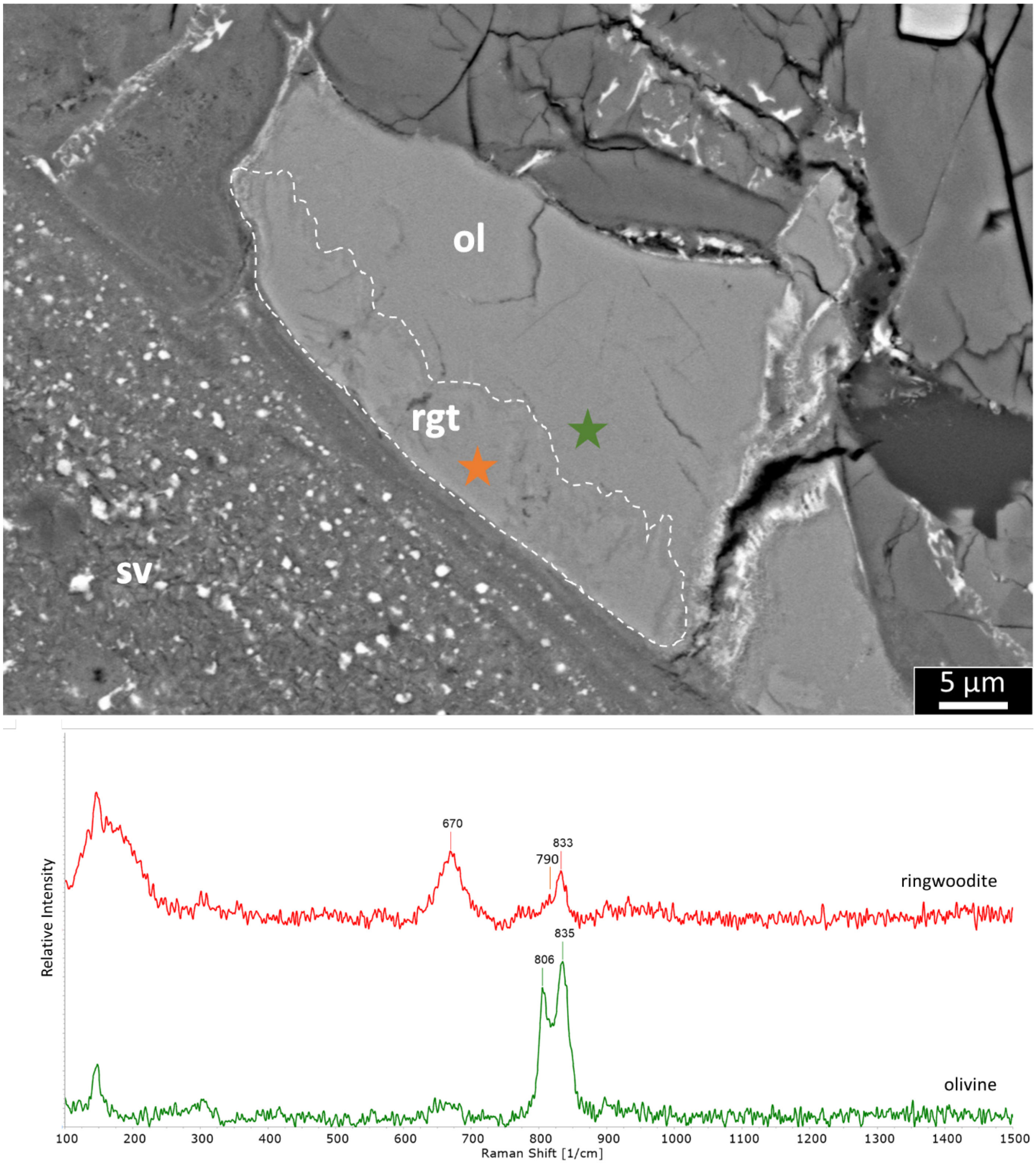

**Fig. 2.17.** BSE image of a partial transformation from olivine (ol) to ringwoodite (rgt) in NWA 7635. Ringwoodite is only observed in the portion of the olivine grain that is in direct contact with the shock vein (sv). The red and green stars indicate the location where the corresponding Raman spectra were obtained.

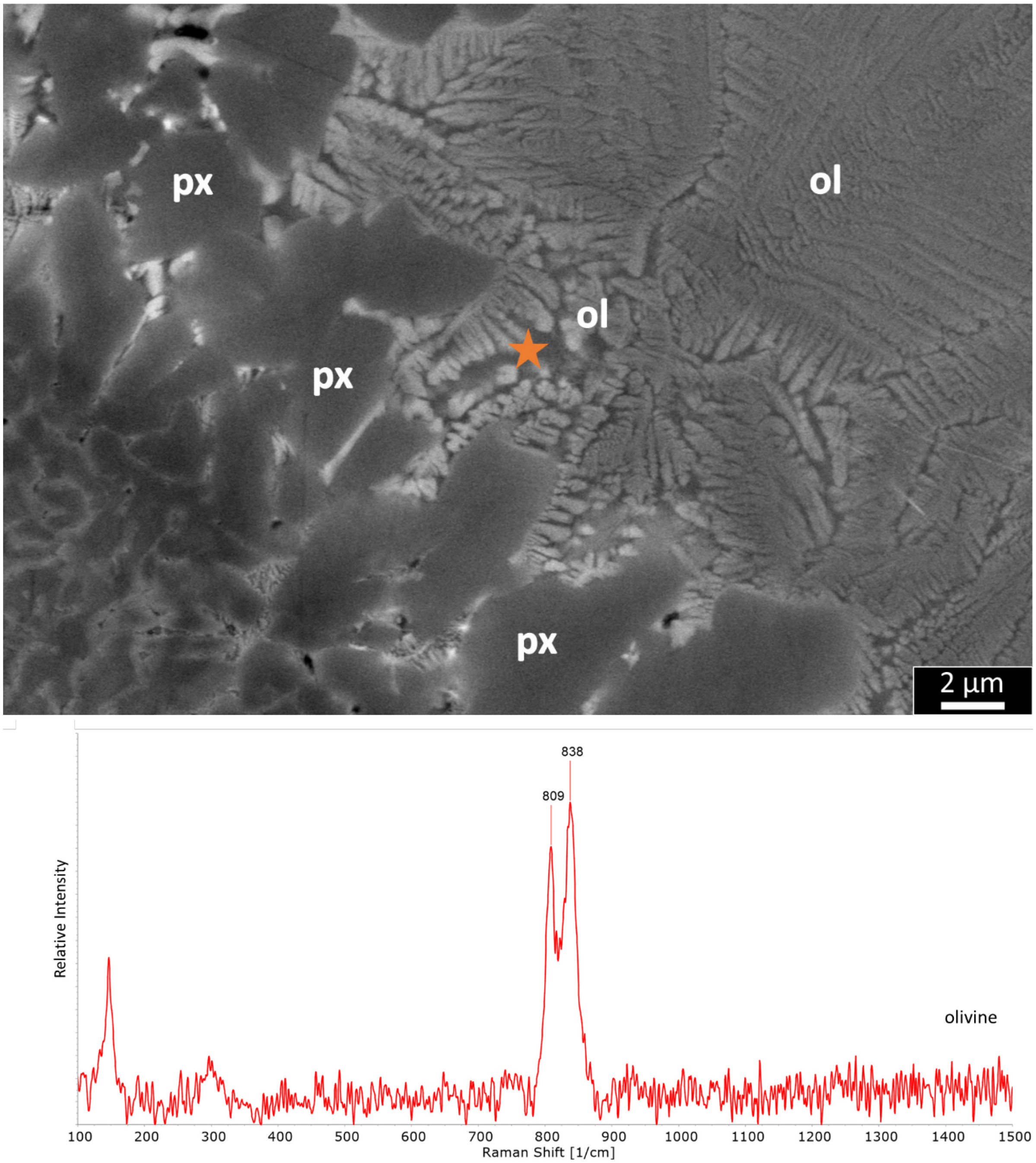

**Fig. 2.18.** BSE of dendritic olivine (ol) and euhedral pyroxene (px) mineral assemblages that were observed in NWA 2626. The red star indicates the location where the corresponding Raman spectrum was obtained.

**Table 2.3.** Summary of shock effects in this study.

| Sample | Deformation | | Plagioclase | Transformation | | Mineralogy associated at shock veins / melt pockets |
|---|---|---|---|---|---|---|
| | Olivine | Pyroxene | Composition* | Bulk | Local | |
| JaH 479 | mosaicism | pf, mosaicism, mt | $An_{76}Ab_{18}Or_{6}$-$An_{66}Ab_{31}Or_{3}$ | pl → msk<br>sil → seif | sv, smp | pyroxene, tissintite, olivine, maskelynite, stishovite, pyrrhotite, augite, oxides |
| KG 002 | mosaicism | pf, mosaicism | $An_{39-58}Ab_{41-49}Or_{1-7}$-$An_{94}$ | pl → msk | smp | pyroxene, tissintite, augite, maskelynite, ringwoodite, olivine, stishovite, oxides, glass |
| NWA 2046 | pf | pf, mosaicism, mt | $An_{74.4}Ab_{25.5}Or_{0.1}$-$An_{62.4}Ab_{36.5}Or_{1.1}$, zoned | pl → msk<br>brown ol | smp | pyroxene, maskelynite, olivine |
| NWA 2626 | n.o. | pf, mosaicism, mt | $An_{66.0-71.0}Or_{0.4}$ | pl → msk | sv, smp | olivine, maskelynite, pyroxene, pigeonite |
| NWA 6162 | n.o. | pf, mosaicism, mt, pdfs | $An_{62.1-65.8}Or_{0.5-0.3}$ | pl → msk | smp | pyroxene, maskelynite |
| NWA 7635 | mosaicism | pf, mosaicism | $An_{60.7-61.8}$ | pl → msk | sv, smp | pyroxene, olivine, ringwoodite, maskelynite, sulphides, oxides |
| NWA 10299 | n.o. | pf, mosaicism, mt | $An_{55\pm4}Ab_{43\pm4}Or_{2.4\pm1.8}$-$An_{48-61}Ab_{38-51}Or_{0.9-6.3}$ | pl → msk<br>sil → seif | sv, smp | pyroxene, maskelynite, sulphides, glass |
| NWA 11057 | n.o. | pf, mosaicism | $An_{46.0-56.3}Or_{1.8-0.7}$ | pl → msk | smp | pyroxene, maskelynite, oxides |
| NWA 11073 | mosaicism | pf, mosaicism | $An_{46.6-47.8}Or_{2.7-2.0}$ | pl → msk | sv, smp | pyroxene, olivine, maskelynite, stishovite, oxides |
| NWA 11255 | n.o. | pf, mosaicism, mt | $An_{37.9-52.3}Or_{4.5-2.1}$ | pl → msk<br>sil → seif | sv, smp | pyroxene, maskelynite |
| NWA 11955 | n.o. | pf, mosaicism, mt, pdfs | $An_{50.9-55.0}Or_{2.0-1.9}$ | pl → msk | sv, smp | pyroxene, maskelynite |
| NWA 12262 | mosaicism | pf, mosaicism | $An_{50.9-52.1}Or_{2.1}$ | pl → msk | smp | pyroxene, olivine, maskelynite, oxides |
| NWA 12919 | n.o. | pf, mosaicism | $An_{40-56}Ab_{43-57}Or_{1-4}$ | pl → glass | smp | pyroxene, hollandite, ringwoodite, maskelynite |

**<u>Notes:</u>** n.o. = not observed; An = anorthite; ab = albite; or = orthoclase; pl = plagioclase; msk = maskelynite; sil = silica; seif = seifertite; ol = olivine; sv = shock vein; smp = shock melt pocket; pf = planar fractures; mt = mechanical twinning; pdfs = planar deformation features

## 2.4 Discussion

All meteorites studied show evidence of moderate to strong shock metamorphism. The observed deformation and transformation features are used to constrain the shock conditions (pressure and post-shock temperatures) experienced by the 13 meteorites in this study. Shock pressures are calibrated from shock-recovery experiments (Fritz et al. 2019; Stöffler et al. 2018) or by the crystallization products of shock melting based on their stability from static, high-pressure experiments (Sharp and deCarli, 2006). These two ways of constraining shock conditions experienced by a meteorite are discussed in the following sections.

### 2.4.1 Shock Pressures and Post-shock Temperature – Bulk Rock

Bulk shock pressures in the studied thin sections are constrained by deformation in pyroxene and olivine, and the structural state of feldspar is noted in Table 2.3. Olivine is found as phenocrysts in JaH 479, KG 002, NWA 7635, and NWA 12262 only. In these four meteorites, olivine displays mosaicism, which indicates shock pressures of 15–65 GPa (Fig. 2.19). Pyroxene grains in all studied samples display varying degrees of mosaicism and multiple sets of planar fractures (Table 2.3). Mosaicism develops in broad pressure ranges from 20–70 GPa (Fig. 2.19) in which higher pressures correlate to stronger mosaicism (Stöffler et al. 2018). Strong mosaicism is characterized by larger numbers and smaller sizes of 'windows' of misorientations within the crystals. Planar fractures in pyroxene are produced at moderate and high shock pressures (Stöffler et al., 2018). Because of the limitations of using planar fractures in pyroxene to constrain shock pressures, their crystallographic orientation was not measured to confirm their identification. Mechanical twins attributed to shock have been documented in pyroxene, as well as simple twins that are likely igneous (Fig. 2.5). These mechanical twins are documented in JaH 479, NWA 2046, NWA 2626, NWA 6162, NWA 10299, NWA 11255, and NWA 11955 and form at shock pressures of 5-70 GPa (Fig. 2.19). Pyroxene has also been observed to contain planar deformation features and planar elements. Shock-related planar features form over the pressure range 30-60 GPa (Fig. 2.19) and are distinguished by the deformation of mechanical twins.

In all studied samples, with the exception of NWA 10299, plagioclase has been completely transformed to maskelynite throughout the bulk rock. Using previously reported plagioclase compositions and experimental data, shock in these meteorites is constrained by maskelynite to have been a minimum of ~27 – 30 GPa and a maximum of <45 GPa (Table

2.4; Fig. 2.20). Plagioclase in NWA 10299 is fully melted, as evidenced by the presence of flow lines and vesicles in BSE images (Fig. 2.21), which constrains the shock pressure to have been ≥45 GPa (Stöffler et al., 2018; Fritz et al., 2019).

Brown olivine was documented in one meteorite, NWA 2046, in this study. Brown coloring in martian meteorites is induced by iron nanoparticles (Treiman et al., 2007; Van de Moortèle et al., 2007; Bläß et al., 2010). The brown olivine is suggested to form at pressures of ~55 GPa based on observations of chassignite NWA 2737 and poikilitic shergottite NWA 1950 (Takenouchi et al., 2017; Takenouchi et al., 2018). However, this shock pressure (55 GPa) is not consistent with our findings of maskelynite throughout NWA 2046, which constrains shock pressure to have been <45 GPa (Fritz et al., 2019). Instead, the presence of brown olivine may arise due to chemical reactions during the shock event. Both the oxidation of $Fe^{2+}$ following H devolatilization during shock and the reduction of olivine during shock have been cited as possible mechanisms for the production of brown olivine that do not require extreme shock pressures (those above maskelynite-formation; Peslier et al., 2010). In either case, the presence of brown olivine does not distinguish NWA 2046 in terms of bulk rock shock pressures from the other samples in this study.

Seifertite was positively identified in JaH 479, NWA 10299, and NWA 11255 by its distinct cross-hatched appearance in BSE images, by fractures radiating into neighbouring maskelynite indicating a volume increase upon decompression, and by its electron beam sensitivity. These attributes are all consistent with seifertite, confirmed by transmission electron microscopy selected area diffraction patterns (El Goresy et al. 2008). Initial studies of seifertite suggested transformation pressures of cristobalite to a denser structure (seifertite) at pressures >60 GPa; however, identification of seifertite in Zagami and Shergotty and the pressure conditions of other high-pressure phases in these meteorites refined the estimate of seifertite formation pressure to >35 GPa (Dera et al., 2002; El Goresy, 2008). The formation of seifertite by shock metamorphism is attributed to solid-state processes transforming either tridymite or cristobalite at pressures below seifertite's thermodynamic stability field of ~100 GPa (Bläß, 2013; Kubo et al., 2015). Given the moderate shock pressures, stishovite should be the more thermodynamically stable phase of $SiO_2$ in Shergotty, Zagami, JaH 479, NWA 10299, and NWA 11255. Bläß (2013) proposed a solid-state transition model to produce metastable seifertite below its thermodynamic stability field, without breaking bonds or formation of quenchable intermediate phases. In this model, part of the crystal structure of the precursor $SiO_2$ phase collapses due to induced shock, and the shock then causes structural changes that amorphize, preventing phase reversal. However, Bläß (2013) cautions against using seifertite to constrain peak shock pressures until a detailed understanding of the transition process is resolved because seifertite is a metastable, and not thermodynamically equilibrated high-pressure phase that is dependent on the transition process itself. For example, seifertite has appeared metastably in pressures as low as ~11 GPa in an experimental shock study (Kubo et al., 2015). While this study does not exactly mimic shock during impact events, it reaffirms the need for a greater understanding of the transition process before seifertite can be used to effectively constrain bulk rock shock pressures.

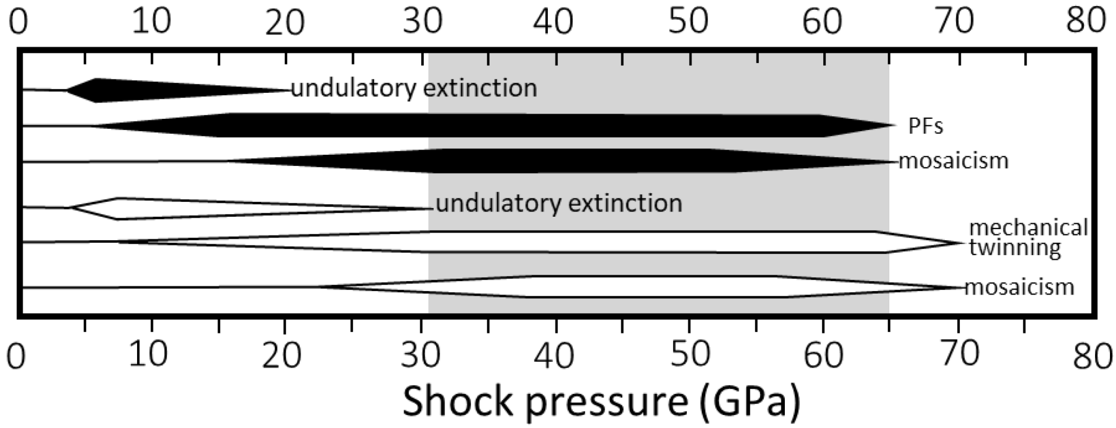

**Fig. 2.19.** Shock effects in olivine (black bars) and pyroxene (white bars) relative to shock pressure scales and data compiled by Stöffler et al. (2018). The grey area corresponds to the pressure range of JaH 479 based on the shock deformation features described.

**Table 2.4.** Plagioclase compositions and the associated minimum pressure required for the complete transformation of plagioclase to maskelynite as noted in the observations of these meteorites (Fritz et al., 2019).

| Sample | Plagioclase Composition | Maskelynite Minimum Formation Pressure (GPa) |
|---|---|---|
| JaH 479 | $An_{76}Ab_{18}Or_{6}$-$An_{66}Ab_{31}Or_{3}$ | ~27 - 28 |
| KG 002 | $An_{39-58}Ab_{41-49}Or_{1-7}$-$An_{94}$ | ~28 - 30 |
| NWA 2046 | $An_{74.4}Ab_{25.5}Or_{0.1}$-$An_{62.4}Ab_{36.5}Or_{1.1}$, zoned | ~27 - 28 |
| NWA 2626 | $An_{66.0-71.0}Or_{0.4}$ | ~27 - 28 |
| NWA 6162 | $An_{62.1-65.8}Or_{0.5-0.3}$ | ~27 - 28 |
| NWA 7635 | $An_{60.7-61.8}$ | ~28 |
| NWA 11057 | $An_{46.0-56.3}Or_{1.8-0.7}$ | ~28 - 30 |
| NWA 11073 | $An_{46.6-47.8}Or_{2.7-2.0}$ | ~29 |
| NWA 11255 | $An_{37.9-52.3}Or_{4.5-2.1}$ | ~28 - 30 |
| NWA 11955 | $An_{50.9-55.0}Or_{2.0-1.9}$ | ~28 |
| NWA 12262 | $An_{50.9-52.1}Or_{2.1}$ | ~28 |
| NWA 12919 | $An_{40-56}Ab_{43-57}Or_{1-4}$ | ~28 - 30 |

<u>**Notes:**</u> Plagioclase composition obtained from the meteoritical bulletin.

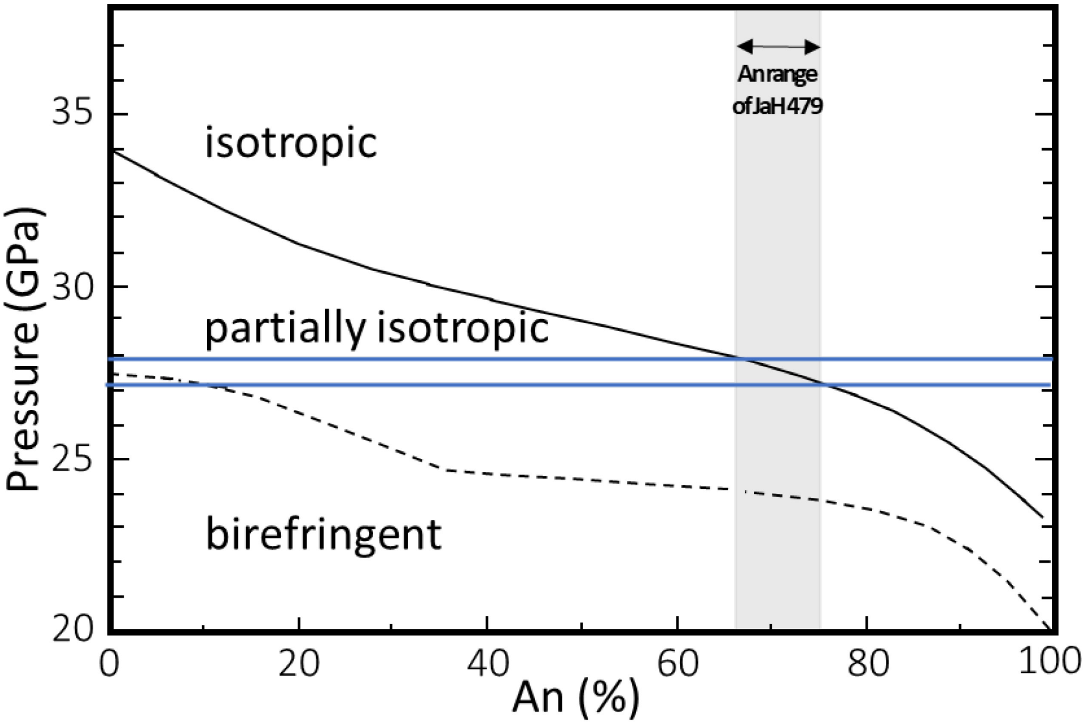

**Fig. 2.20.** Pressure versus anorthite (An) content for experimentally shocked plagioclase (Fritz et al., 2019). The dashed line indicates where the transformation of plagioclase to maskelynite begins, and the solid line indicates where the total transformation of plagioclase to maskelynite occurs. Pressures greater than ~45 GPa (not shown) lead to the melting of maskelynite, which quenches to glass. The grey area shows the An content of JaH 479. The minimum pressure for maskelynite formation is given by the blue lines (27-28 GPa).

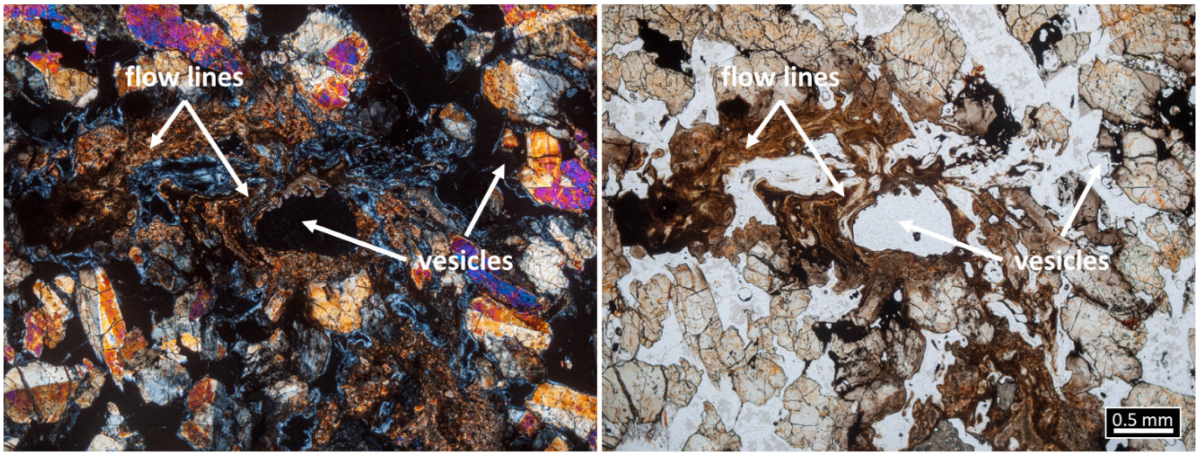

**Fig. 2.21.** XPL (left) and PPL (right) image of the same area in NWA 10299 showing the flow lines and vesicles associated with melting of plagioclase.

Combined, the shock deformation and transformation features described indicate approximately two distinct groupings for the bulk rock shock pressures. The first group, with shock pressures of ~27–45 GPa, consists of JaH 479, KG 002, NWA 12919, NWA 2046, NWA 2626, NWA 6162, NWA 7635, NWA 11057, NWA 11073, NWA 11255, NWA 11955, and NWA 12262. NWA 10299 comprises the second group, with a peak shock pressure of >45 GPa. The shock classification system of Stöffler et al. (2018) can be applied consistently and accurately to these meteorites. The first group is classified as M-S4 and NWA 10299 is classified as M-S6; post-shock temperatures indicated by these groups are ~200-250°C and ~1,100°C, respectively (Table 2.5; Stöffler et al., 2018).

**Table 2.5.** Bulk rock shock pressures experienced by the meteorites in this study and their corresponding shock classification (Stöffler et al., 2018). N/A = not applicable

| Sample | Bulk Olivine Pressure (GPa) | Bulk Pyroxene Pressure (GPa) | Maskelynite Formation Pressure (GPa) | Shock Classification* |
|---|---|---|---|---|
| JaH 479 | 15 – 65 | 20 - 70 | ~27 - 45 | M-S4 |
| KG 002 | 15 – 65 | 20 – 70 | ~28 - 45 | M-S4 |
| NWA 2046 | 55 – 65 | 20 – 70 | ~27 - 45 | M-S4 |
| NWA 2626 | N/A | 20 – 70 | ~27 – 45 | M-S4 |
| NWA 6162 | N/A | 30 – 70 | ~27 – 45 | M-S4 |
| NWA 7635 | 15 – 65 | 20 – 70 | ~28 – 45 | M-S4 |
| NWA 10299 | N/A | 20 – 70 | >45 | M-S6 |
| NWA 11057 | N/A | 20 – 70 | ~28 – 45 | M-S4 |
| NWA 11073 | 15 – 65 | 20 – 70 | ~29 – 45 | M-S4 |
| NWA 11255 | N/A | 30 – 70 | ~28 – 45 | M-S4 |
| NWA 11955 | N/A | 30 – 70 | ~28 – 45 | M-S4 |
| NWA 12262 | 15 – 65 | 20 – 70 | ~28 – 45 | M-S4 |
| NWA 12919 | 15 – 65 | 20 - 70 | ~28 - 45 | M-S4 |

## 2.4.2 Shock Conditions – Shock Melt and High-Pressure Phases

Shock melt, as veins and pockets, has been documented in all of the studied meteorites. The mineral transformations associated with shock melt and stability of minerals that have crystallized from shock melt provide an additional constraint on pressure experienced by meteorites during the shock event (Chen et al., 1996; Beck et al., 2005; Sharp and DeCarli, 2006; Walton et al., 2014; Sharp et al., 2019). Shock melt experiences localized initial temperatures of up to 2500°C (Walton et al., 2014), significantly higher than the post-shock temperatures recorded by the bulk rock as discussed in the previous section. Here, the thermal history and evolution of shock melt and minerals associated with shock melt are discussed. These minerals include those formed from igneous minerals along shock melt margins in the host rock, within former igneous fragments entrained in the melt, and minerals in the shock melt matrix. These observations, summarized in Table 2.3, are used to further constrain shock pressures of the meteorites in this study.

Localized shock melt is dominated by fine-grained silicate minerals embedded in silicate glass (Table 2.3). These fine-grained minerals in the shock melt matrix are interpreted to have crystallized from the melt based on grain size, shape, and compositional zoning observed as a greyscale change within a single crystal from core to rim. Host rock fragments incorporated into the shock melt are generally pyroxene – due to the high modal abundance of pyroxene in the host rock – but plagioclase, phosphates, and oxides are also entrained in shock melt. Mineral transformations in former igneous minerals in contact with quench crystallized shock melt are interpreted to form by solid-state mechanisms, based on identical textures reported in other shergottites (e.g. Walton et al. 2014).

Shock melt pockets typically contain spheres of Fe-sulfides and crystallization products including assemblages of high-pressure phases, olivine, and pyroxene. The dominant mineral assemblages in this study's sample suite are pyroxenes, similar to those found in the shock vein of NWA 11255, plus olivine or stishovite. Pyroxene crystals are submicrometer to submillimeter in size and are generally zoned and rounded. Olivine crystals generally form dendritic assemblages with pyroxene, the assemblages of which are up to a few tens of micrometers in size while the width of individual 'fingers' are <1 µm. Stishovite was observed exclusively in shock melt pockets as bladed crystals, up to 0.5–2 µm in length. The shock melt pockets containing stishovite were dominated by the stishovite in addition to minor amounts of pyroxene and host rock fragments. Pyroxene dominant shock melt pockets and shock veins, especially those presenting ringwoodite transformations along the margins, likely crystallized at pressures of ~16-18 GPa (Walton et al., 2014). Those assemblages containing olivine in addition to pyroxene are crystallized at pressures ≤14 GPa (Herzberg and Zhang, 1996; Walton et al., 2014). Mineral assemblages containing stishovite will be discussed in more detail later in this section.

In NWA 2626, olivine was found in dendritic assemblages with pyroxene in the shock melt matrix (Fig. 2.18). Dendritic olivine has been produced in dynamic crystallization experiments on run products representative of shock melt in shergottites (Walton and Herd, 2007). These experiments show that this olivine morphology forms by rapid crystallization from the melt. High-pressure phases associated with shock veins typically only occur in host rock olivine and plagioclase along the vein margins. Ringwoodite and tissintite, formed from igneous olivine and plagioclase respectively, occur along the margins of shock veins and shock melt pockets (Fig. 2.15 and Fig. 2.17). Tissintite is also found in former plagioclase fragments entrained within the melt, and in the shock melt matrix with dendritic morphology up to 40 µm in length. The tissintite textures along the shock vein margins and in fragments entrained within the melt are consistent with the occurrence of this mineral, documented in other shergottites (Walton et al., 2014). Tissintite forms under pressures of 6-8 GPa with plagioclase composition – higher pressures result in a wadeitelike structure + stishovite (Ma et al., 2015; Rucks et al., 2018). Because maskelynite formation occurs at a minimum of 27-28 GPa for plagioclase compositions relevant to the meteorites studied (An ~65-78), one of two scenarios may explain tissintite formation at lower pressures than recorded in the bulk rock, as discussed by Fritz et al., (2019). Tissintite forms towards the end of the shock event during pressure release or a secondary wave of lower pressure creates the conditions for tissintite formation after the primary wave. Formation of tissintite in both scenarios is also a possibility.

Ringwoodite places controls on localized shock melt. This mineral is unstable at temperatures of >900°C and pressures of 0 GPa (Fritz et al., 2017; Greshake et al., 2013; Kimura et al., 2004). This indicates that at least portions of the meteorites experienced pressures high enough to form ringwoodite (>18 GPa) while cooling that same area in a timeframe similar to the shock wave itself to prevent decomposition of the ringwoodite as the overall rock cools (Fritz et al., 2017).

Stishovite was identified as bladed silica crystals in the shock melt pockets of several of the meteorites in this study (JaH 479, KG 002, and NWA 11073). This high-pressure $SiO_2$ polymorph typically forms under shock pressures >34 GPa and may undergo a transition to post-stishovite polymorphs at pressures greater than 48 GPa (El Goresy et al., 2000; Pozuelo et al., 2019). However, stishovite can be formed at pressures as low as ~5 GPa in manufactured $SiO_2$ phases such as soda-lime glass (Pozuelo et al., 2019). The practical applications of this low-pressure stishovite formation in naturally occurring solids is still unknown, but suggest that there is still more to be understood when using stishovite as a means of constraining shock pressure. Stishovite was the only high-pressure $SiO_2$ polymorph observed in KG 002 and NWA 11073 leading to the suggestion that peak shock pressure was in fact <40 GPa. The variety of high-pressure phases in these meteorites suggest localized pressures ranging from 5- >35 GPa that rapidly quenched and cooled in a process unrelated to observed solid-state transformations.

NWA 11255 has a shock vein that crosscuts the entire thin section and is 200 µm at its widest (Fig. 2.22a). Within this shock vein matrix reside a series of zoned, rounded grains from 0.1-5 µm (Fig. 2.22b). EDS and Raman spectroscopy show these spherical crystals were newly formed Na-, Mg-, and Al-rich zoned pyroxenes (measured as wt% oxides). It is important to note however, that mineral assemblage composition in these samples is not a function of vein thickness as noted in Tissint (Walton et al., 2014). Instead, grain size is related to vein thickness and will be discussed next.

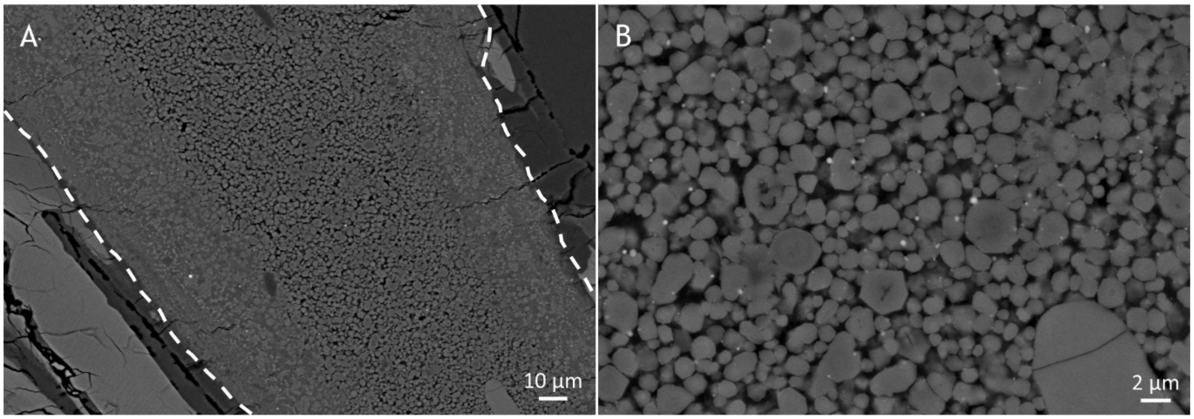

**Fig. 2.22.** BSE images of the wide shock vein in NWA 11255 showing the boundaries of the shock vein as white dashed lines (a) and the fine-grained minerals in the vein matrix (b). Pyroxene crystals closer to the center of the vein are and have noticeably more void space (black portions) between them. This void space was likely occupied by interstitial silicate glass which was removed during thin section preparation.

The thermal history of shock melt is a function of a number of variables including the proportion of host rock fragments entrained within the melt, the volume of shock melt formed, which may be approximated by the width of shock veins and shock melt pockets, and the temperature difference between the melt and host rock (Shaw and Walton, 2013). Host rock fragments are colder than the surrounding shock melt and affect the quench rate leading to smaller grains crystallizing in the adjacent shock melt. Shock melt pockets and shock veins that are finer grained contain an abundance of entrained host rock fragments compared to those melts that are coarser grained. Fragments of host rock that are >10 µm in size likely affect localized cooling rates, which is observed as a change in crystal size. Independent of entrained host rock fragments, crystal sizes are largest at the center of the shock veins and become smaller towards the boundaries where cooling rates were faster. This texture found in both NWA 2626 and NWA 11255 is typical of quench crystallized shock veins. However, unlike shock veins, I note that there is no apparent correlation between crystal size and shock melt pocket size. For example, JaH 479 contains a ~50 µm wide shock melt pocket with grain sizes ≤1 µm, while NWA 11057 contains an ~20 µm wide shock melt pocket with dendritic intergrowths up to 1-2 µm in size.

In contrast to shock veins, shock melt pockets in this suite of meteorites occur as isolated pockets heterogeneously distributed throughout the rock and have gradational boundaries with the surrounding host rock. These textural features are consistent with shock melt pockets in other martian meteorites (e.g. Walton and Shaw 2009) and indicate their formation by shock impedance contrasts (including open space) in the host rock. The shock vein formation history in these meteorites is more variable and will be discussed next.

Walton et al. (2014) describe three scenarios for shock melt crystallization and its relation to shock duration for shock veins in the Tissint meteorite. Here, I will discuss these three scenarios which are a function of shock vein thickness and provide examples for each scenario from the meteorites in this study. Larger shock veins such as those documented in NWA 11255 quench after decompression within 1s, while shock veins of intermediate thickness, representing smaller volumes of shock melt, quench during pressure release at 20-50 ms. The thinnest shock veins, such as those splayed throughout JaH 479, quench at the peak shock pressure in 10 ms. A reasonable estimate for the shock duration of NWA 11255 would be 10-20 ms, similar to Tissint (Walton et al., 2014). However, those meteorites with thin, splayed shock veins (e.g. JaH 479) indicate small volumes of shock melt that rapidly quenched (i.e. 10-20 ms). The shock vein mineral assemblages in JaH 479 consisting primarily of pyroxene also suggest that the shock veins experienced lower pressures than the bulk rock and the dwell time of the shock event was shorter than the quench time. Those meteorites with shock veins in the 10s of micrometer width range (e.g. NWA 7635, NWA 11073) were subject to quenching of the shock veins during pressure release forming mineral assemblages that are stable at pressures less than those that quenched at the peak shock pressure. For example, the pyroxene + olivine mineral assemblages (<14 GPa) in shock veins of NWA 11073 are stable below the peak shock pressure experienced by the bulk rock (~28-45 GPa). Additionally, Kubo et al. (2015) note that a shock period of at least ~0.01 s is required to initiate transformation of silica to seifertite. This observation supports the expected shock durations in JaH 479, NWA 10299, and NWA 11255, and other moderately shocked shergottites to be ~10-20 ms (Walton et al., 2014).

The crystallization pressure of the shock melt, indicated by the stability of minerals that have crystallized from melt – olivine + pyroxene (≤14 GPa), stishovite (~5- <40 GPa), tissintite (6-8 GPa), pyroxene (≤14 GPa) – record generally lower pressures than those recorded in the bulk rock via deformation in mafic minerals and complete transformation of plagioclase to maskelynite (27 – 45 GPa). Fritz et al. (2019) note that meteorites that are the result of high velocity impact events are derived from regions outside the “isobaric core”. Rocks within the isobaric core of an impact cratering event experienced a broad plateau of approximately equal pressure, while those outside the isobaric core are shocked by a wave without a broad pressure plateau. As the shock wave propagates away from the point of impact it begins to interact with the release wave, shortening and eventually removing the pressure plateau while simultaneously decreasing the shock pressure as a function of distance. Martian meteorites are not derived from within the isobaric core of an impact event because the rocks within this zone experience shock pressures that would melt or vaporize the rock upon decompression (>60 GPa; Fritz et al. 2017). Therefore, martian meteorites are derived from zones outside the isobaric core, where the shock wave has lost its broad pressure plateau, and mineral assemblages in shock melts form at a lower shock pressure, at a later time, compared to those recorded by shock effects in the bulk rock. This observation is consistent with the variety of localized high-pressure phases in meteorites such as JaH 479 (e.g. pyroxene + olivine assemblages, stishovite, ringwoodite solid-state transformation). As noted in NWA 11073 and applicable to the other meteorites in this study, this shock pressure-time scenario is consistent with the mineral assemblages, bulk rock shock, and localized shock features that were observed.

### 2.4.3 Future Directions for Shock Studies

Martian meteorites are ejected from the near-surface units adjacent to craters by random, hypervelocity impacts on the surface of Mars (McSween and Stolper, 1980; Melosh, 1985; Treiman et al., 2000; Head et al., 2002; Bowling et al., 2020). During impact ejection, constituent minerals experience shock metamorphism. Detailed study of these shock effects, combined with high-resolution numerical simulations of impact events, can yield information on the size of the crater from which the meteorites were ejected. Observations made in this chapter constrain the peak shock pressure experienced by 13 shergottites, which is one variable required to model the impact ejection event (Bowling et al., 2020). An additional variable is dwell time, defined as the time that material spends above 1 GPa during a shock event (Fig. 2.23). The dwell time of a given rock varies based on the size of the impactor, the distance – both horizontally and vertically – from the point of impact, and the target material. Combining detailed studies of shock effects with thermal models for the post-shock thermal evolution of the shergottite Tissint has been successful in constraining the dwell time (10-20 ms; Walton et al. 2014). While our study did provide an estimate of dwell time, higher resolution thermal modeling of shock melt crystallization times is needed to better constrain this variable.

Bowling et al. (2020) conducted high resolution numerical modeling to determine dwell times for mafic martian rocks. Longer dwell times correspond to more energetic impact events and thus larger craters. Therefore, it is important to determine accurate dwell times for proper estimation of source crater diameter. Several shergottites (Tissint, Zagami, Shergotty) have had their dwell times constrained to be ~10 ms, corresponding to a crater that is ~14 km in diameter (Bowling et al. 2020).

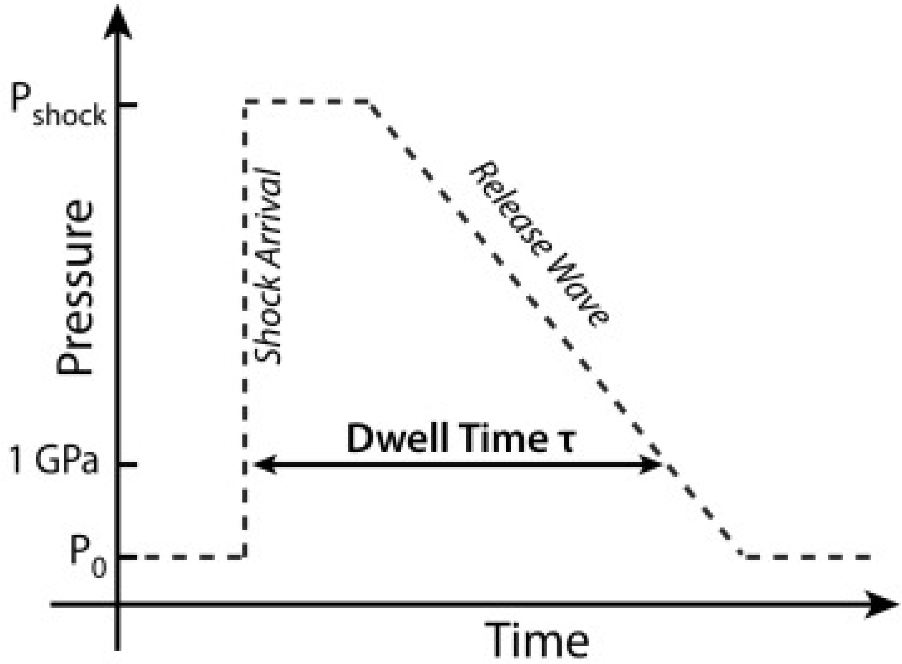

**Fig. 2.23.** Schematic showing the definition of dwell time τ as described by Bowling et al. (2020). While the shock duration experienced by a meteorite does not exactly equal the dwell time, it can be used as a near-estimate for it.

While shock effects in martian meteorites can be used to estimate the size of the source crater, determining which meteorites belong to the same ejection groups is constrained by their ejection age. The timing of ejection from the surface of Mars can be determined by summing the terrestrial residence age and cosmic ray exposure (CRE) age of the meteorites (Nyquist et al., 2001; McSween, 2015; Udry et al., 2020). Because meteorites in this study show no evidence of multi-generational impact processing, such as brecciation observed in polymict martian meteorite NWA 7034, it can be assumed that the timing of ejection coincides with the timing of shock (Agee et al., 2013; Walton et al., 2014). CRE ages have previously been determined for JaH 479, NWA 2046, NWA 2626, NWA 6162, and NWA 7635 (Table 2.2). As noted by Table 2.2, NWA 2046, NWA 2626, NWA 6162, and NWA 7635 share nearly identical CRE ages of ~1.1 Ma. Indeed, this grouping of meteorites has already been suggested to be launched from a single impact event (Lapen et al., 2017). Determining the CRE ages of the remaining meteorites in this study will refine the number of ejection events for shergottites from its current estimation noted in Section 1.2.2. In the next chapter, I will discuss other variables that may impact the number of ejection events for a given group of meteorites.

## 2.5 Conclusions

Detailed analysis of shock effects in 13 previously understudied shergottites has provided the background information required to perform impact modeling. This study used a combination of optical microscopy, scanning electron microscopy, and laser micro-Raman spectroscopy to constrain peak shock pressures experienced by the bulk rock, as well as high-pressure minerals associated with shock melt.

I find two distinct groups of meteorites based on shock deformation and transformation in the bulk rock. The first group (NWA 12919, NWA2046, NWA 2626, NWA 6162, NWA 7635, NWA 11057, NWA 11073, NWA 11255, NWA 11955, and NWA 12262) contain plagioclase that has completely transformed to maskelynite, a diaplectic plagioclase glass, indicating a minimum pressure of ~27-29 GPa and a maximum pressure of ~45 GPa (and post-shock temperatures of ~200-250°C and ~1,100°C, respectively) based on shock-recovery experiments and plagioclase composition (Stöffler et al., 2018; Fritz et al., 2019). NWA 10299 encompasses the second group and is a highly shocked meteorite as evidenced by melted plagioclase that forms from shock pressures of at least 45 GPa (Stöffler et al., 2018; Fritz et al., 2019). Shock melt in all of the meteorites contains various assemblages of high-pressure minerals that form under different pressure and temperature conditions. These observations suggest impact mechanics consistent with findings by Fritz et al. (2017). The meteorites experienced pulses of shock that cause multiple instances of microsecond pressure peaks, rather than a large and sustained pressure plateau for a few milliseconds. Shock pulses produce localized melting wherein the mineralogy is dominated by the original material and conductive cooling can produce high-pressure phases such as ringwoodite that normally decompose at 0 GPa and high temperature time periods associated with whole-rock cooling of a meteorite.

Despite the different bulk rock shock groups of the meteorites in this study, more data are needed to determine whether they come from different ejection events. Determination of their CRE ages will constrain the number of ejection events both with this suite of meteorites and with all known shergottites. Using the information in this chapter, future studies can determine dwell times to input into impact modeling to proceed towards determining these meteorites' source craters. In the next chapter, future directions of shock studies can be applied to determining source craters for martian meteorites will be discussed.

# Chapter 3. Mapping of Candidate Source Craters for Martian Meteorites

## 3.1 Introduction

Martian meteorites are solid rock fragments ejected from near-surface units by random, hypervelocity impact events (Melosh, 1984). Currently, there are 143 unpaired martian meteorites in the world's collection composed of 11 different classes (IMCA, 2020; Walton et al., 2012). The previous chapter worked to expand the number of samples suitable for determining candidate source craters. In this chapter, a selection of four previously characterized martian meteorites (Table 3.1) are studied to determine the most probable source craters for martian meteorites. The four meteorites considered in this study are Zagami, Tissint, Chassigny, and Northwest Africa (NWA) 8159 (Table 3.1). The following description of these meteorites follows the igneous classification scheme of Walton et al. (2012).

Zagami is an enriched mafic intersertal shergottite. Its bulk mineralogy consists of approximately equal amounts of pyroxenes (augite and pigeonite) and plagioclase (completely transformed to maskelynite), with minor titanomagnetite, ilmenite, olivine (fayalite), and pyrrhotite (Stolper and McSween, 1979; McCoy et al., 1999). The crystallization history and complexity of lithologies in Zagami suggests a history of magmas that were dry and progressively more enriched in incompatible elements and FeO (McCoy et al., 1999). Tissint is a depleted permafic olivine-phyric shergottite, characterized by zoned olivine macrocrysts increasing in fayalite from core to rim, embedded in a fine-grained matrix of pyroxene (augite, pigeonite, and orthopyroxene cores) and plagioclase (completely transformed to maskelynite) (Aoudjehane et al., 2012). Minor phases include titanomagnetite, pyrrhotite, apatite, Ti-poor chromite, and merrillite (Aoudjehane et al., 2012).

Chassigny is a cumulate Fe-rich dunite with pyroxene (clinopyroxene and orthopyroxene), plagioclase (completely transformed to maskelynite), and minor oxides (chromite and ulvöspinel) (Prinz et al., 1974; Mason et al., 1976; Floran et al., 1978; Wadhwa and Crozaz, 1995). Other minor phases include igneous melt inclusions, pigeonite, chlorapatite, troilite, marcasite, amphibole, pentlandite, ilmenite, rutile, and baddeleyite (Floran et al., 1978; McSween, 1994; Treiman et al., 2007). Melt inclusions contain the phases augite, low-Ca pyroxene, baddeleyite, kaersutite, pyrrhotite, Al-rich chromite, pentlandite, Ti-biotite, F-rich apatite, alkali maskelynite, silica, and ilmenite (Floran et al., 1978; Johnson et al., 1991; Treiman et al., 2007; McCubbin et al., 2013). The Mg/Fe of olivine in Chassigny is 49.1, contains <1 wt% $Al_2O_3$, $TiO_2$, $Cr_2O_3$, MnO, and CaO (Papike et al., 2009), and infrequent occurrences of small symplectic exsolutions have been observed (Greshake et al., 1998). Chassigny's formation is a highly contended topic and was initially thought to have formed from a low-Ca ultramafic magma (Floran et al., 1978). Johnson et al. (1991) later suggested that Chassigny was formed by an $Al_2O_3$-poor lava with ~1.5 wt% dissolved water, similar to boninite lavas found on Earth. However, experiments on liquids, discussed by Johnson et al. (1991), have failed to produce phases and melt-inclusion assemblages found in Chassigny (Filiberto, 2008). A more recent study analyzed rocks at Gusev crater and suggested they are from the same parental magma as Chassigny (Filiberto, 2008), but this hypothesis is argued to not comprehensively explain all of Chassigny's petrologic observations (Nekvasil et al., 2010).

NWA 8159 is an augite-rich shergottite and a unique member of the martian meteorites (Herd et al., 2017). Its bulk mineralogy comprises augite, plagioclase (partially transformed to maskelynite), Mg-rich olivine, magnetite, maghemite, and pyroxene (orthopyroxene) (Herd et al., 2017). Minor phases in NWA 8159 are ilmenite, merrillite, chlorapatite, and Cr-spinel (Herd et al., 2017). NWA 8159 crystallized from a melt that was depleted in incompatible elements that sampled a mantle source that is unique relative to other known martian meteorites (Herd et al., 2017).

These four meteorites sample Amazonian age (<~3.37 Ga) lava flows and have ejection ages <12 Ma (Table 3.1) suggesting that the crater(s) that produced the ejection event(s) are relatively young and most likely amongst the very best-preserved on Mars. It is unlikely that the four meteorites in this study share a common ejection event even though they share these similar characteristics. Here, I will propose an approach to evaluate source crater variables that builds on previous work and discuss the likelihood that a given crater is the source crater for one or any of these four martian meteorites.

### 3.1.1 The Source Crater Problem

Mouginis-Mark et al. (1992) noticed the basaltic composition of martian meteorites, and both their young crystallization and ejection ages, and modeled constraints on the size of crater needed to launch/escape Mars, all helping to constrain the source region and crater(s) for these meteorites by providing the composition and age of the target surface as well as the size and approximate age of the crater(s). These constraints resulted in the identification of 25 candidate source craters on the martian surface that then had their best and worst attributes described. The most recent estimates at the time suggested a minimum crater size of 100 km to eject rock fragments from the surface (Vickery and Melosh, 1987). Mouginis-Mark et al. (1992) noted that there were no craters preserved on lava flows in the Tharsis region that met the >100 km diameter size requirements and therefore relaxed the size constraint to craters >10 km diameter. Even with the relaxed size requirements only 9 of the 25 candidate source craters were located on young, volcanic terrain that was capable of producing the 11 martian meteorites in the world's collection at the time of publication (Mouginis-Mark et al., 1992). In contrast, the most recent ejection models for martian meteorites now indicate that with an oblique impact, a crater diameter as small as ~2.5 km can be responsible for an ejection event (Head et al., 2002). Updated impact modeling and a more comprehensive collection of martian meteorites have challenged the proposal by Mouginis-Mark et al. (1992) that a single crater is responsible for the ejection of the martian meteorites (Nyquist et al., 2001; McSween, 2015; Head et al., 2002). However, I propose that the core idea discussed in the Mouginis-Mark et al. (1992) study to restrict potential source regions on Mars based on the characteristics of the martian meteorites is an appropriate and potentially fruitful method to determine source craters for martian meteorites given the present availability of more comprehensive data.

Some recent attempts to link martian meteorites to specific launch events have met with limited success (e.g. Werner et al., 2014; Ody et al., 2015; Kereszturi and Chatzitheodoridis, 2016). Werner et al. (2014) used reflectance spectroscopy to match surface mineralogy with that of shergottites, concluding that the <5 Ma, 55-km diameter Mojave Crater is the source for shergottites. This conclusion relies on results from reflectance spectroscopy, and two critical assumptions: 1) that shergottites were ejected in a single launch event, and 2) that the crystallization ages of shergottites have been affected by impact resetting and are much older (~4.3 Ga) than previously realized. Additionally, the spectral signature is not sufficiently unique to specifically identify shergottites - the shergottite spectral signature can be found in numerous locations on Mars. Indeed, a basaltic surface is one of the most abundant surface compositions on Mars (e.g., Christensen et al. 2001; Ody et al. 2015; Viviano et al., 2019). Thus, spectral matching is acceptable as a minor criterion for identifying candidate source craters, but cannot be relied upon. The age at which a meteorite is ejected from Mars is estimated by its cosmic ray exposure (CRE) age plus its terrestrial residence time. The CRE ages of shergottites range from ~0.7 Myr to ~20 Myr (Nyquist et al. 2001; Christen et al. 2005) and therefore argue for ejection in multiple small impact events, rather than a single large –

and therefore more energetic – impact event, as argued by Werner et al. (2014). The ancient age of shergottites has been ruled out as resulting from the nuances of Pb loss and/or contamination in these meteorites (Belluci et al., 2016). Ody et al. (2015) mapped spectral analogues of martian meteorites to determine their source regions. Reflectance spectroscopy is hindered by dust coverage especially in the Tharsis and Elysium regions where the most probable candidate source craters are found (Christensen et al., 2001). Despite accounting for dust and other spectral effects, obtaining accurate spectral signatures is improbable. However, gaps and dust-free areas can be found and thus remain a potential piece of supporting evidence (Viviano et al., 2019). The Kereszturi and Chatzitheodoridis (2016) study surveyed rayed craters on Amazonian lava plains to identify possible source craters for nakhlites. However, well-preserved crater morphologies, including ejecta, and the lack of overprinted small craters are not enough evidence on their own to provide accurate relative ages for potential source craters (Tornabene et al., 2006, 2012; Herd et al., 2018).

Our approach to the determination and evaluation of candidate source craters is similar to the one presented by Tornabene et al. (2006) after Mouginis-Mark et al. (1992) but with more recent and higher resolution datasets, additional characteristics for identifying the impact craters, and a more comprehensive understanding of the shock history of the meteorites and how that specifically relates to a modeled crater diameter. The Mouginis-Mark et al. (1992) approach was further modified to include the identification of key physical characteristics of martian craters that supported that they are extremely well-preserved and most likely youthful; these include far-traversing secondary crater rays identified in thermal images (Tornabene et al. 2006), craters with very few superposed craters of any size, and is being modified in this study to include the presence of well-preserved pitted impact melt deposits (e.g., Tornabene et al. 2012).

### 3.1.2 New Insights

Advancements in martian imagery and new meteorite samples have led to more pieces of the source crater puzzle being put together. McEwen et al. (2005) and Tornabene et al. (2006) identified thermally or thermophysically distinctive crater rays on Mars, which correlate with far-traversing dense radial clusters of secondary craters as a feature unique to some of the best-preserved craters on Mars, which are likely young craters. Tornabene et al. (2006) demonstrated that the Martian secondary crater rays are physical manifestations, or proof, of a high-velocity ejection process (>1 km/sec) that took place during crater formation. Furthermore, while the secondary crater rays are likely the result of ejected material with velocities lower than the martian escape velocity (<5 km/sec) they are produced by coherent ejecta blocks released via the same spallation process that is responsible for martian meteorites. Estimates of the number of these secondaries or coherent ejecta blocks produced by impacts suggest a higher probability that craters that specifically preserve secondary crater rays produced by numerous coherent blocks, some of which very likely achieved escape velocity. This specifically makes craters with preserved far-traversing secondary carter rays the strongest candidates as martian meteorite sources as they preserve the evidence that they produced numerous coherent blocks that achieved high-velocity. It should be noted that not all radial features around craters are secondary crater rays; indeed, craters also exhibit other radial features, some far-traversing, associated with other aspects of the ejection process that do not produce numerous secondary craters, including airblast scouring of the surface that occurs during an impact on atmosphere-bearing bodies (Schultz and Gault, 1979; Quintana et al., 2018). Werner et al. (2014) identified Mojave Crater as a rayed crater; however, a closer inspection reveals that the radial features that they claimed as rays are airblast scour and not associated with dense clusters of secondaries (L. Tornabene, personal communication, December 10, 2020).

One of the best indicators of a crater's preservation is the presence of crater-related pitted materials, which are consistent with primary volatile-rich impact melt bodies produced during the impact process (Tornabene et al., 2012). Pitted impact melts are quite distinctive and easy to identify as they consist of clusters of pits that lack or only possess slightly raised rims; they range from ~10 meters to ~3 kilometers in size and are found exactly where impact melts observed on other bodies accumulate: on the crater floor, atop ejecta, and trapped between crater walls/terraces. The pits likely form during impact from degassing of volatile-rich pipes creating the negative relief depressions into the accumulated impact melt deposits (Tornabene et al., 2012).

In summary, results from the Tornabene et al. (2006, 2012) studies suggest that craters that retain both pitted impact melts and display secondary crater rays are a high priority for candidate source craters for martian meteorites; this is due to the fact that they both provide physical evidence for high crater preservation, which may relate to youthfulness, while the secondary rays specifically provide the physical evidence for the production of numerous high-velocity ejecta blocks.

In order to place constraints on the size of the craters that likely produced a specific meteorite, shock-related impact modeling must be conducted. Bowling et al. (2020) simulated impacts on the martian surface with iSALE-2D, a specialized version of the original SALE program (Amsden et al., 1980) for modeling fluid flow and shock processes in complex geologic settings. With shock characteristics from a given meteorite, the program can calculate dwell times, which are used to determine impactor sizes required for the ejection of the meteorite (Bowling et al., 2020), which in turn may be used to estimate the size of the crater. Dwell time is the period of time that material spends at pressures above 1 GPa during a shock event (Section 2.4.3). Because the dwell time varies for materials at different distances from the point of impact, it cannot be directly related to the impactor size without additional information (Bowling et al., 2020). This includes the peak shock pressure, as discussed in chapter 2, ejection velocity and/or ejection depth. The effective crater diameter range for the selection of martian meteorites used in this study has been constrained with these parameters in mind and are presented in Table 3.1.

**Table 3.1.** Ages, modeling results, and query results for selected martian meteorites.

| Meteorite | Martian Type[1] | Crystallization Age (Ma) | Ejection Age (Ma) | Effective crater diameter range (km)[2] | N[3] |
|---|---|---|---|---|---|
| Zagami | Shergottite (Enriched Mafic Fine-Intergranular) | 177 ± 3[a] | 2.89 ± 0.2[c,d,e,f,g] | 10 - 33 | 13 |
| Tissint | Shergottite (Depleted Permafic Olivine-Phyric) | 574 ± 20[a] | 0.7 ± 0.3[h] | 10 - 164 | 19 |
| Chassigny | Chassignite (Dunite) | 1396 ± 51[a] | 11.1 ± 0.6[c,d,e,I,j,k,l,m] | 2.5 - 89 | 30 |
| NWA 8159 | Shergottite (Depleted Mafic Aphyric / Augite-Rich) | 2370 ± 250[b] | 1.2 ± 0.1[b] | 2.5 - 156 | 33 |

Notes: [1]As described by IMCA (2020); see Walton et al. (2012) for nomenclature guide. [2]based on iSale 2-D modeling as per Bowling et al. (2020) and Herd et al. (2018). [3]Number of candidate source craters on Amazonian igneous terrains and within the effective crater diameter range. [a]Belluci et al. (2018) weighted averages of references therein; [b]Herd et al. (2017); [c]Herzog and Caffee (2014); [d]Eugster et al. (1997); [e]Eugster et al. (2002); [f]Schnabel et al. (2001) [g]Park et al. (2003) [h]Aoudjehane et al. (2012); [i]Terribilini et al. (1998); [j]Terribilini et al. (2000); [k]Marty et al. (2006); [l]Ott (1988); [m]Korochantseva et al. (2011).

In their models, Bowling et al. (2020) ran simulations between a 10 km spherical basalt impactor and a Mars-like basaltic target in two-dimensional axial symmetry. This model geometry was necessary to obtain a high spatial resolution of 5 meters in order to resolve the region of material ejected above the martian escape velocity. However, the simulations were restricted to vertical impacts (those occurring at 90° to the target surface), despite widespread evidence of impacts occurring at oblique angles, typically closer to 45° (Bowling et al., 2020; Shoemaker, 1962). Bowling et al. (2020) suggest that the impactor size could be changed by a factor of 2-3 on the lower margin in an oblique impact; a factor of 2 is used for the lower crater diameter in Table 3.1.

## 3.2 Methods

### 3.2.1 Querying Potential Source Craters – Relational Database

Identification of candidate source craters was accomplished by querying a subset of the database of the most well-preserved craters, which includes craters that preserve and have well-expressed pitted impact melts (Tornabene et al., 2012). Officially unnamed craters within the database take their designations from the crater database produced by Robbins and Hynek (2012). Well-preserved craters typically have a younger relative age than those that are less well-preserved. However, varying erosional rates, deposition, mass-wasting, and presence of subsurface volatiles can obscure this correlation. Tornabene et al. (2012) establish a correlation between the preservation of pitted material and its host crater. Craters near the polar caps, in this case a latitude higher than 60° or lower than -60°, present no evidence of pitted materials and are subsequently excluded from the primary database (Tornabene et al., 2012). This observation is also consistent in the context of this study because the upper few meters of polar deposits are thick layered deposits of ice and dust, a characteristic that is inconsistent with the basaltic martian meteorite compositions. The initial survey contained over 1000 craters, of which 800 have been imaged in sufficient detail to identify pitted materials (Tornabene et al., 2012); 290 craters are confirmed to have pitted material and are therefore included in the database (Tornabene, personal communication, 2020). Craters are assigned a rating of 1-5, where 5 is the most well-preserved and 1 is the least well-preserved (Tornabene et al., 2012). The database was loaded into a Structured Query Language (SQL) server alongside other crater characteristics including Thermal Emission Spectrometer (TES; Christensen et al., 2001) derived Dust Cover Index (DCI; Ruff and Christensen, 2002), albedo, and thermal inertia (Tornabene et al., 2012). The differences between the criteria of the Tornabene et al. (2012) and Robbins and Hynek (2012) databases will now be discussed as it has implications on the rating of craters.

A significant disparity in the distribution of crater rankings between the two databases arises because of the different criteria used when rating craters (Fig. 3.1). As a test of the effectiveness of the Robbins and Hynek (2012) classification scheme, I compare the rank five and rank four craters in the Tornabene et al. (2012) database with the preservation rating assigned to these craters in the Robbins and Hynek (2012) database (Fig. 3.2). Given that all class 5s and 4s have the very best-preserved crater-related pitted deposits (interpreted to be primary impact melt-bearing deposits emplaced during the crater's formation) and that there is a strong correlation between pitted deposit preservation and the preservation of the host crater (e.g., Tornabene et al. 2012; Sizemore et al., 2018), all these craters should fall under the preservation 4 rating of Robbins and Hynek (2012), representing the very best-preserved craters on Mars.

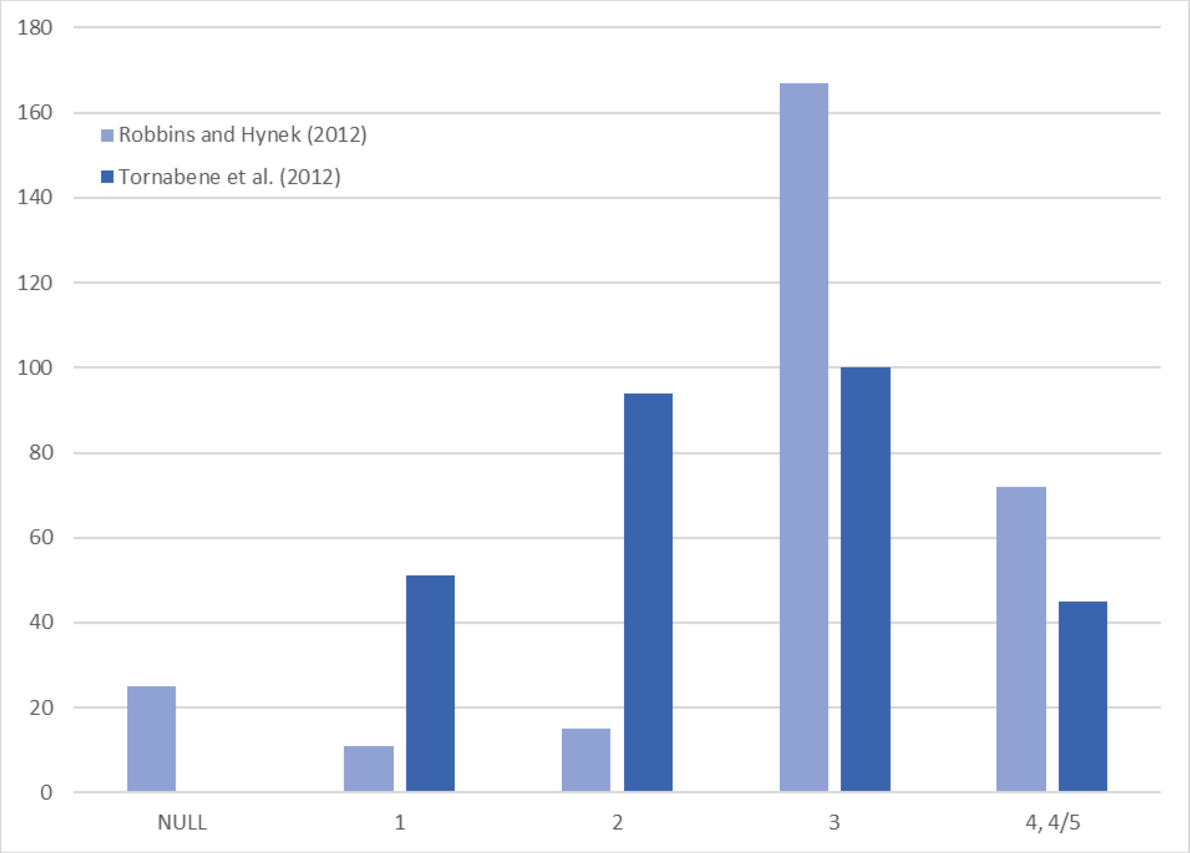

**Fig. 3.1.** Preservation (Tornabene et al., 2012) and degradation (Robbins and Hynek, 2012) rankings of all craters shared by the two databases. The Tornabene et al. (2012) database 5s and 4s are combined due to sharing well-preserved crater-related pitted deposits as a primary feature and indication of relatively recent formation. NULL values in the Robbins and Hynek (2012) database are those for which no degradation classification was assigned.

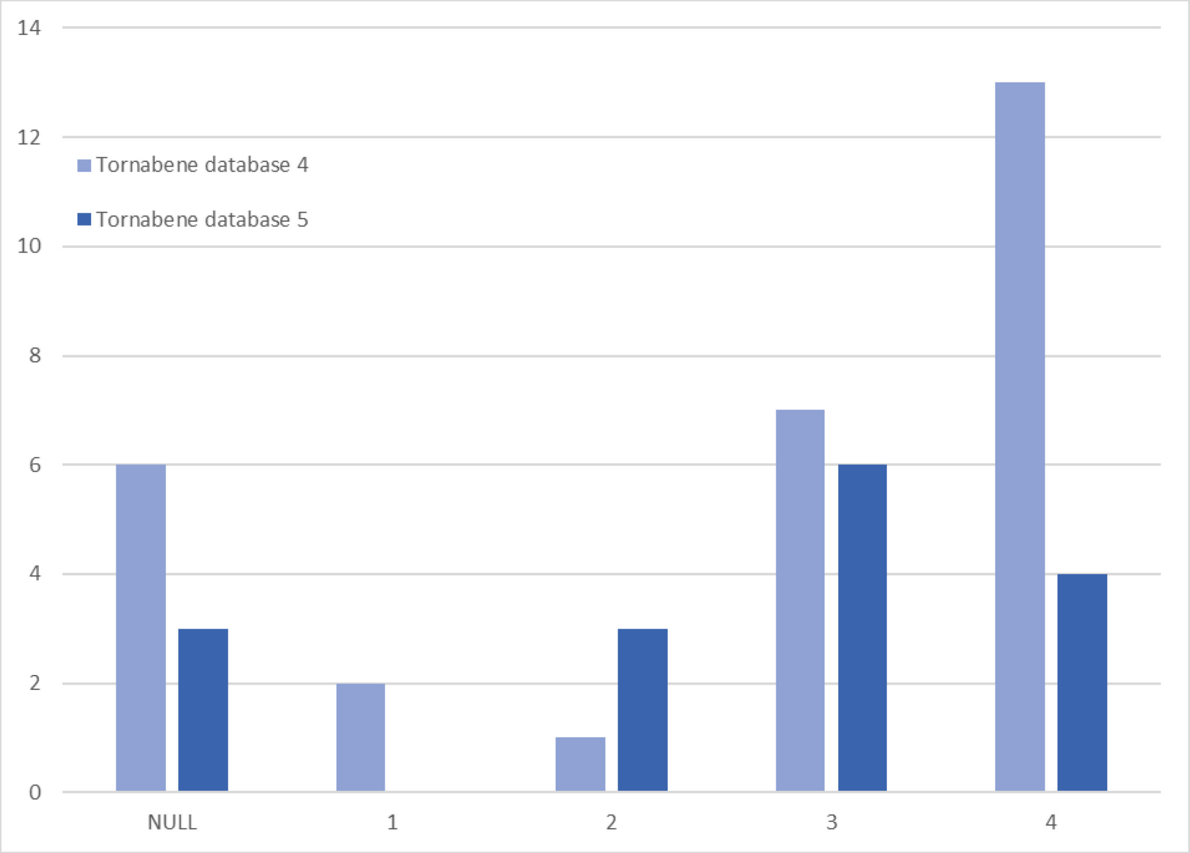

**Fig. 3.2.** The Tornabene et al. (2012) database 5s and 4s and their associated Robbins and Hynek (2012) classification. Nine of the forty-five most well-preserved craters in the Tornabene et al. (2012) database have no classification (as indicated by NULL) in the Robbins and Hynek (2012) database.

However, 62% of the 5s and 4s in the Tornabene et al. (2012) database are classified as 3 or below in the Robbins and Hynek (2012) database (Fig. 3.2). This suggests that the preservation rating of Robbins and Hynek (2012) has insufficient fidelity with respect to identifying the very best-preserved craters on Mars. Indeed, a close inspection of the classification criteria for preservation by Robbins and Hynek (2012) reveals that they did not consider the presence of impact-melt deposits within their craters, which is arguably the most diagnostic characteristic for identifying the best-preserved craters on any planetary body (e.g., Hawke and Head, 1977; Tornabene et al. 2012). This assertion is further supported by the fact that many Robbins and Hynek (2012) craters show no sign of impact melt preservation and yet are rated as a 4 (see discussion in Tornabene et al. 2018). The Tornabene et al. (2012) database provides greater clarity concerning relative crater ages compared to the Robbins and Hynek (2012) database; therefore, it is used exclusively in this study to compare the relative preservation of source craters.

Each of the craters within the database includes its corresponding surface geologic unit (Tornabene et al., 2012) as described by Scott and Tanaka (1986). The equivalent surface geologic unit in the more recent Tanaka et al. (2014) is also recorded. Of note, between the two versions of the map, are minor boundary changes to geologic units, and the addition of the Amazonian and Hesperian impact unit (AHi; Tanaka et al., 2014) that maps the surface coverage of craters and their surrounding ejecta. Because AHi does not describe the material that was impacted, it is included in the list of volcanic units. I then manually evaluated any craters that were identified as AHi in the resulting queries to determine whether the underlying material was Amazonian volcanic.

The specific characteristics related to Zagami, Tissint, Chassigny, and NWA 8159 (see Table 3.1) were applied to queries of the crater database for this study. To obtain the candidate source craters that are the most likely sources of any of these martian meteorites, a more exclusive query was established that accounts for the characteristics of all four meteorites. This query is as follows: the crater must be located on an Amazonian volcanic unit, the crater must have a 'preservation' rating of ≥3 as described by Tornabene et al. (2012), and the crater diameter must fall between 10 and 33 km. This crater diameter range encompasses permissible diameters for all four of the martian meteorites (Table 3.1). In total, 52 craters were candidates for at least one of the meteorites in this study (see Appendix B). Only 17 craters satisfied the criteria of all four of the martian meteorites in this study. The most well-preserved craters (8 out of 17), boasting a preservation rating of 4 or 5, were selected for further analysis.

### 3.2.2 Crater Mapping

Examination of candidate source craters was accomplished via mapping based on multiple image datasets and the use of Geographic Information Systems (GIS) software. High Resolution Imaging Science Experiment (HiRISE) images provided the highest spatial resolution (~30 cm/pixel) (McEwen et al. 2007) and were accessed using the Planetary Data System (PDS) directory [https://hirise-pds.lpl.arizona.edu/PDS/]. The images were processed on the fly via Integrated Software for Imagers and Spectrometers (ISIS) to correct and calibrate the raw image data. Image IDs were gathered using Java Mission and Remote Sensing (JMARS; Gorelick et al., 2003; Christensen et al., 2009) and exported into a comma-separated value (CSV) file format. Python was used to semi-automate the acquisition and to process over 1000 HiRISE images. Processed Context Camera (CTX) images were retrieved in a similar fashion using the United States Geological Survey's (USGS) Planetary Image

Locator Tool [https://pilot.wr.usgs.gov/]. CTX images were split into two groups for each crater: low emission, constituting images with a maximum emission angle of 5°; and high emission containing the remainder. Additionally, a global CTX mosaic from the Murray Lab [http://murray-lab.caltech.edu/CTX/] was used as a base map. Both HiRISE and CTX images were gathered in an ~200 km$^2$ area around each of the candidate source craters investigated in this study. Other rasters and global datasets including a blended digital elevation model (DEM) derived from the global Mars Orbiter Laser Altimeter (MOLA) and High-Resolution Stereo Camera (HRSC), Robbins and Hynek (2012) crater catalogue, and global geologic map of Mars (Tanaka et al., 2014) were displayed in Environmental Systems Research Institute's ArcGIS for Desktop® 10.7.1 (ArcGIS). Images in this study, despite being tied to MOLA, are not orthorectified and therefore do not align properly in ArcGIS as they have distinctive camera models and were map-projected in different ways by their respective teams. However, this variation caused little to no effects in relative mapping accuracy. HiRISE images were used primarily to characterize lava flows and to identify post-dating impacts on the crater floors and superimposed on the ejecta blanket. Multiple sets of imagery for each of the candidate source craters were used to visually describe and interpret craters, geologic features, and structural features.

## 3.3 Results and Observations

### 3.3.1 Results of Crater Queries

Queries based on characteristics from individual meteorites return 52 craters that are potential sources for at least one of the four meteorites in this study (Appendix B). Of those 52 craters, 17 satisfy the criteria of all four of the meteorites making them the most probable candidates for at least one of the martian meteorites. From those 17 craters, 8 are the most well-preserved (preservation rating 4 or 5), and therefore the most likely sources of martian meteorites (Table 3.2). This is because the most well-preserved craters are likely to be youthful, an observation that is consistent with the young (<20 Ma) ejection ages of martian meteorites (Tornabene et al., 2006; Nyquist et al., 2001). Craters not listed in Table 3.2 or Appendix B are not ruled out as candidate source craters for martian meteorites. Results of mapping of each of the eight candidate craters are presented in the following sections. The mapping will provide detail on the morphology and geology of the craters and nearby surfaces that can be used to further prioritize the 8 candidate craters selected for evaluation.

**Table 3.2.** Locations, sizes, dust coverage, relative preservation level, and surface units of candidate source craters for martian meteorites. Craters in bold were selected for further evaluation in this study. Italicized craters have been previously suggested as candidate sources for martian meteorites (Mouginis-Mark et al., 1992; Tornabene et al., 2006; Mouginis-Mark and Boyce, 2012).

| Crater Name | Robbins and Hynek (2012) ID[a] | Latitude | Longitude | Region | Diameter (km) | TES DCI[b] | Preservation[c] | Degradation[d] | Skinner ID[e] | Tanaka ID[f] |
|---|---|---|---|---|---|---|---|---|---|---|
| ***Zunil*** | ***15-000240*** | ***7.7*** | ***166.2*** | ***Elysium*** | ***10.2*** | ***0.94*** | ***5*** | ***4*** | ***Aps*** | ***lAvf*** |
| Unnamed | 02-000166 | 40.5 | 231.7 | Alba | 10.8 | 0.927 | 4 | 4 | Hal | AHv |
| *Canala* | *10-000384* | *24.3* | *279.9* | *Tempe* | *11.2* | *0.947* | *5* | *2* | *Hr/Ht2* | *eHh* |
| Unnamed | 03-000226 | 55.3 | 253.6 | Alba | 12.0 | 0.948 | 3 | n.d. | Hal | AHv |
| **Unnamed** | **03-000205** | **32.6** | **254.0** | **Alba** | **12.2** | **0.94** | **4** | **3** | **Nf/NHcf** | **AHv** |
| Unnamed | 10-000307 | 18.0 | 272.2 | Ascraeus | 13.2 | 0.944 | 3 | 4 | At5 | AHv |
| ***Corinto*** | ***15-000165*** | ***16.9*** | ***141.7*** | ***Elysium*** | ***13.5*** | ***0.945*** | ***5*** | ***4*** | ***Ael1*** | ***AHv*** |
| **Domoni** | **02-000116** | **51.4** | **234.4** | **Alba** | **14.0** | **0.95** | **5** | **3** | **Hal** | **AHv** |
| Unnamed | 03-000153 | 31.8 | 296.4 | Tempe | 15.3 | 0.946 | 3 | 3 | Hr | AHi |
| Unnamed | 02-000095 | 39.1 | 238.6 | Alba | 15.4 | 0.954 | 3 | 4 | Hal/Aam | AHv |
| Unnamed | 17-000058 | -18.5 | 228.6 | Daedalia | 19.0 | 0.941 | 3 | 4 | At4 | AHv |
| Unnamed | 03-000099 | 30.8 | 297.6 | Tempe | 19.0 | 0.968 | 3 | 4 | Hchp | AHv |
| ***Unnamed*** | ***09-000015*** | ***19.3*** | ***260.1*** | ***Ascraeus*** | ***19.6*** | ***0.934*** | ***5*** | ***3*** | ***At5*** | ***AHv*** |
| Unnamed | 09-000010 | 14.0 | 264.0 | Ascraeus | 20.7 | 0.948 | 3 | 3 | At5 | AHv |
| ***Unnamed*** | ***03-000082*** | ***44.6*** | ***253.0*** | ***Alba*** | ***21.2*** | ***0.95*** | ***4*** | ***4*** | ***Aau*** | ***AHv*** |
| ***Unnamed*** | ***09-000007*** | ***18.0*** | ***249.1*** | ***Ascraeus*** | ***22.2*** | ***0.948*** | ***4*** | ***4*** | ***At5*** | ***AHv*** |
| ***Tooting*** | ***08-000060*** | ***23.2*** | ***207.8*** | ***Amazonis*** | ***28.9*** | ***0.939*** | ***5*** | ***4*** | ***Aa3*** | ***AHi*** |

Notes: [a]Data source from Robbins and Hynek (2012). [b]Dust Cover Index (DCI) of the crater shown as a deviated value from 1 where 1 is considered dust-free (Ruff and Christensen, 2002). [c,d]Relative preservation of the crater as defined by Tornabene et al. (2012) and Robbins and Hynek (2012), respectively – Preservation is scaled from 1-5 with 5 being the most well-preserved and degradation is scaled from 1-4 with 4 being the most well-preserved. [e,f]Surface unit as described by Scott and Tanaka (1986) and Tanaka (2014), respectively. n.d. = no data

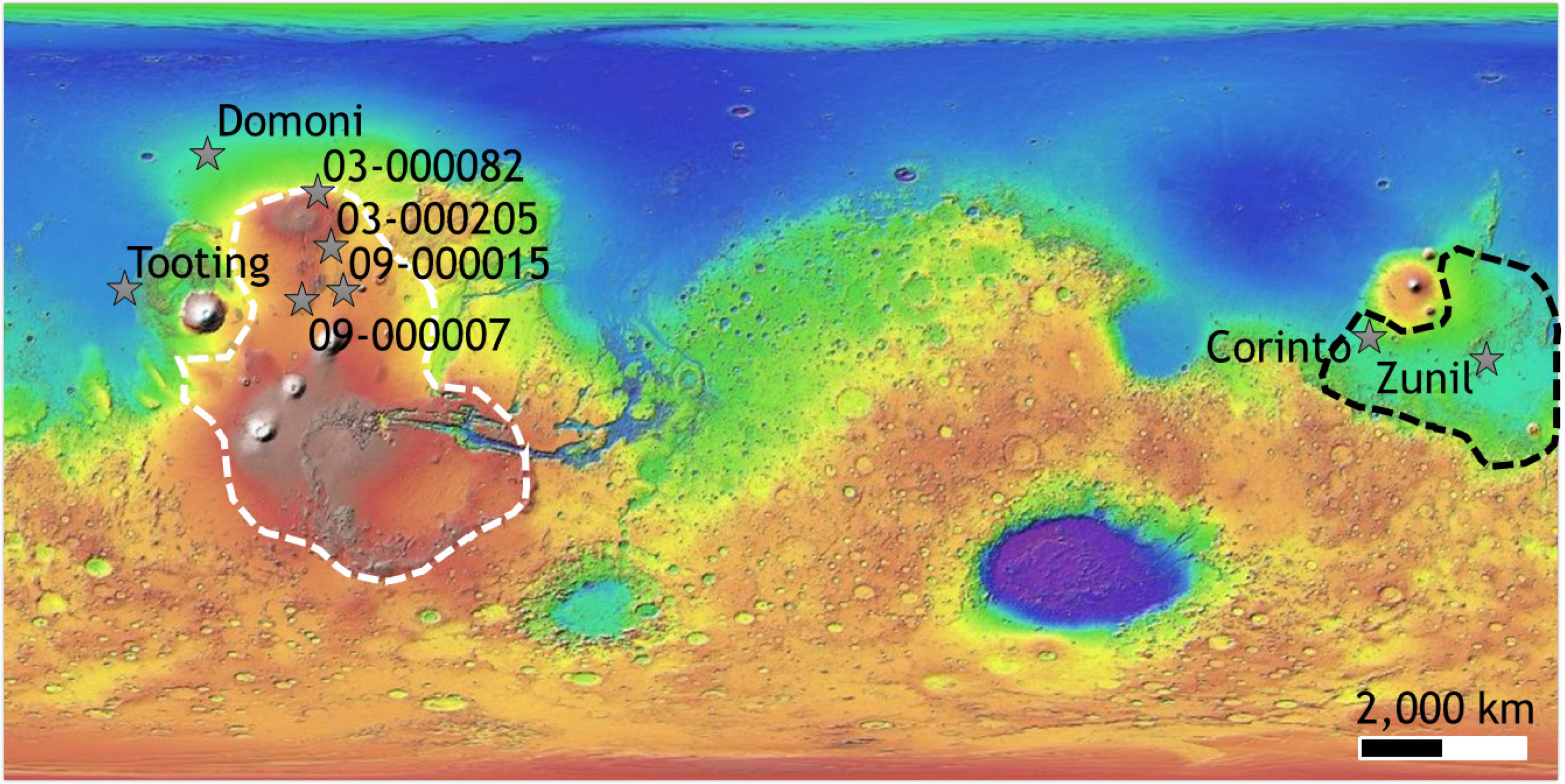

**Fig. 3.3.** Locations of the 8 candidate craters on a colourized shaded relief map. See Fig. 1.1 for further context.

### 3.3.2 Tooting Crater

Tooting is the largest of the 8 candidate source craters, with a rim-to-rim diameter of 29 kilometers (Table 3.2). It is located west of Olympus Mons within Amazonis Planitia (Fig. 3.4A/B; MC-8, Coles et al., 2019). The impact event that formed Tooting occurred on flat lava plains. Chaotic, ridged material from a gravitational failure of an older, more extensive shield (Carr, 2008) fans out on the northern and western flanks of Olympus Mons to within 100 km of Tooting. The subtle morphologies of the immediate terrain surrounding Tooting hinder the mapping of individual volcanic flows adjacent to the crater, but abundant megameter scale Amazonian age flows have been observed to dominate the greater area of Amazonis Planitia (Coles et al., 2019). HiRISE imagery of a nearby fluvial pit shows stacked layers of volcanic flows in the pit wall (Fig. 3.4C). The layers are composed of alternating coherent layers and slope-forming layers. Although significantly more dust-covered, this observation is consistent with deep-seated bedrock exposures of alternating packages of ash and coherent volcanic materials based on HiRISE observations of complex crater central uplifts throughout the Tharsis region (Caudill et al., 2012).

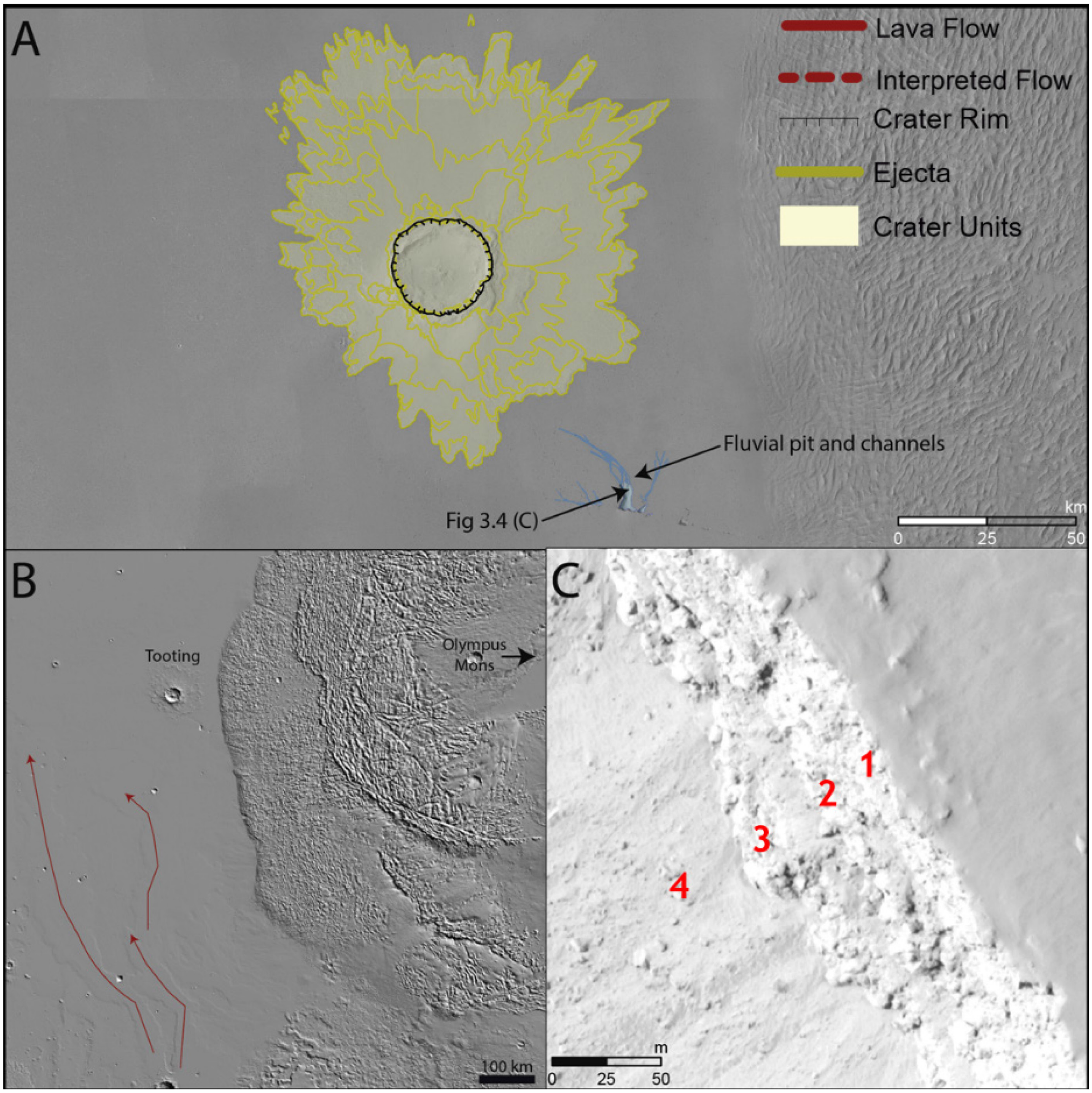

**Fig. 3.4.** A) CTX mosaic showing an overview of Tooting with mapping by Mouginis-Mark and Boyce (2012). The surrounding terrain is virtually flat and individual lava flows are nearly indistinguishable. (B) MOLA hillshade showing Tooting, the western flank of Olympus Mons, and megameter scale lava flows extending from the southern edge of the lava plains. Arrows indicate the inferred direction of flow. (C) HiRISE image (PSP_010333_2025) of the edge of a fluvial pit observed by Mouginis-Mark and Boyce (2012) showing at least 4 coherent layers of volcanic flows (numbered).

### 3.3.3 Domoni

Domoni Crater (D = 14 km) lies approximately halfway between Alba Mons and Milankovic Crater. Diacria, the region that Domoni is found within, (Fig. 3.5A/B; MC-2, Coles et al., 2019) is primarily characterized by terrain that is heavily worn down by cratering and pitting, and elongated lava flows and tubes originating from fissures and vents on the northwestern flank of Alba Mons (Crown et al., 2019A; Crown et al., 2019B).

Thick dust coverage (Ruff and Christensen, 2002) and the worn nature of the surface create a series of poorly defined lava flows that cannot be readily traced more than a few km in most cases. A single flow channel is observed trending southeast-northwest immediately northeast of Domoni (Fig. 3.5A). The ejecta infills a ~4 km diameter crater and is composed of multiple, well-preserved layers (Fig. 3.5A). A meter-scale impact crater (or possibly volcanic skylight) that superimposes the ejecta is observed to the northeast of the crater rim (Fig. 3.5C).

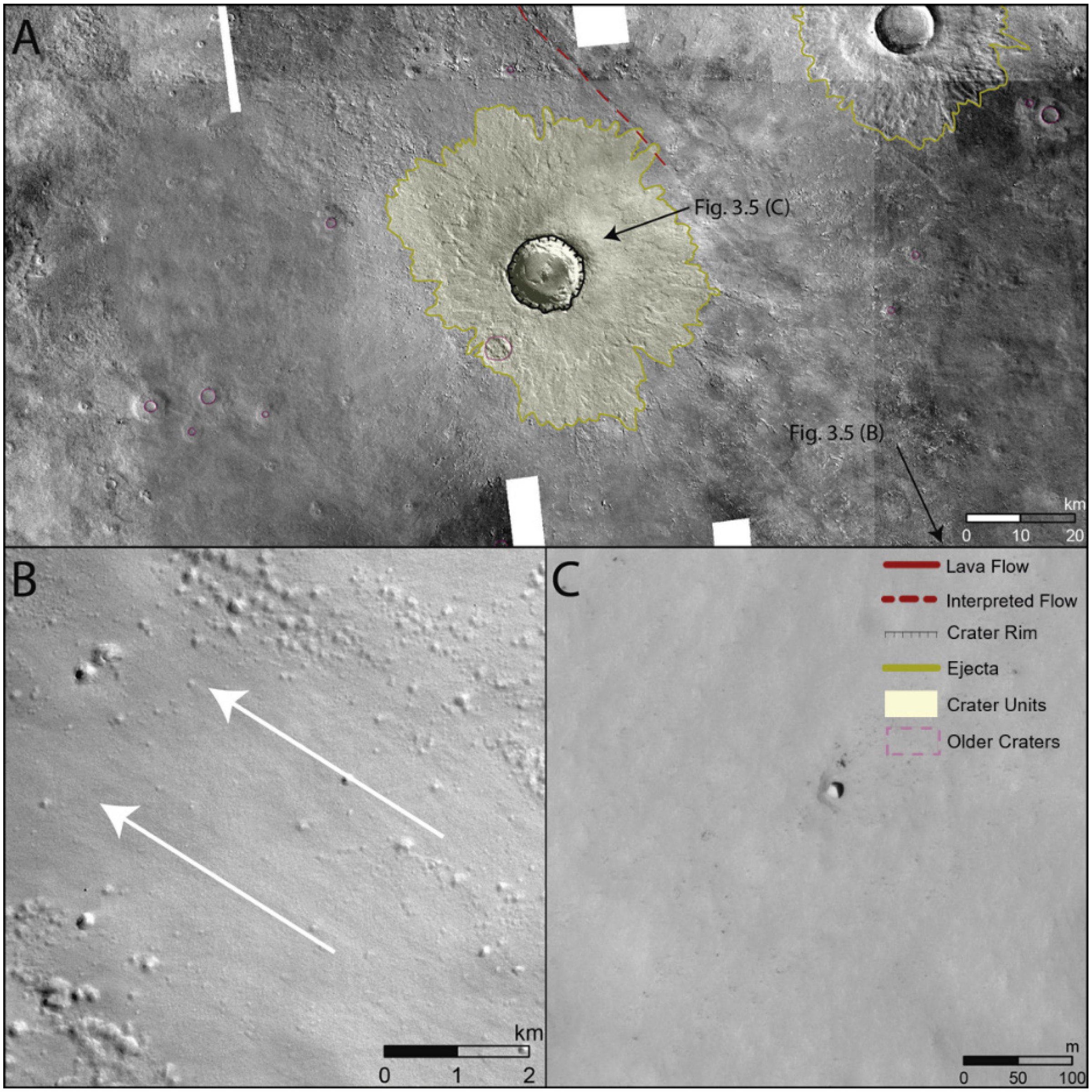

**Fig. 3.5.** A) CTX mosaic showing an overview of Domoni. The nearby terrain is heavily impacted by clusters of secondary craters and unremarkable in terms of major volcanic features. (B) CTX image (B17_016292_2314) showing poorly defined lava flows (white arrows) trending from Alba Mons in the southeast to Domoni in the northwest. (C) CTX

image (ESP_053794_2320) showing a small, circular depression superimposed on the ejecta blanket of Domoni.

### 3.3.4 03-000082

Crater 03-000082 is situated directly on the northern flank of Alba Mons (D = 21.2 km; Fig. 3.6; Fig. 3.7A; MC-3, Coles et al., 2019). Volcanic features including catenae and the caldera of Alba Mons dominate the terrain adjacent to this crater. Stress-related extensional faults and grabens are observed northeast of 03-000082 and continue for hundreds of kilometers (Coles et al., 2019). Mappable lava flows generally trending radially away from the Alba Mons caldera are found on either side of the crater, but specific source vents and fissures are not identifiable over the mapping area (Fig. 3.7A; Tanaka et al., 2014). Flows are typically either smooth and platy or form wrinkle ridges and are observed at the regional scale; individual ridges are not definable locally (Fig. 3.7B/C). Several impacts pre-dating 03-000082 are observed in the ejecta that are upwards of ~4 km in diameter (Fig. 3.7A).

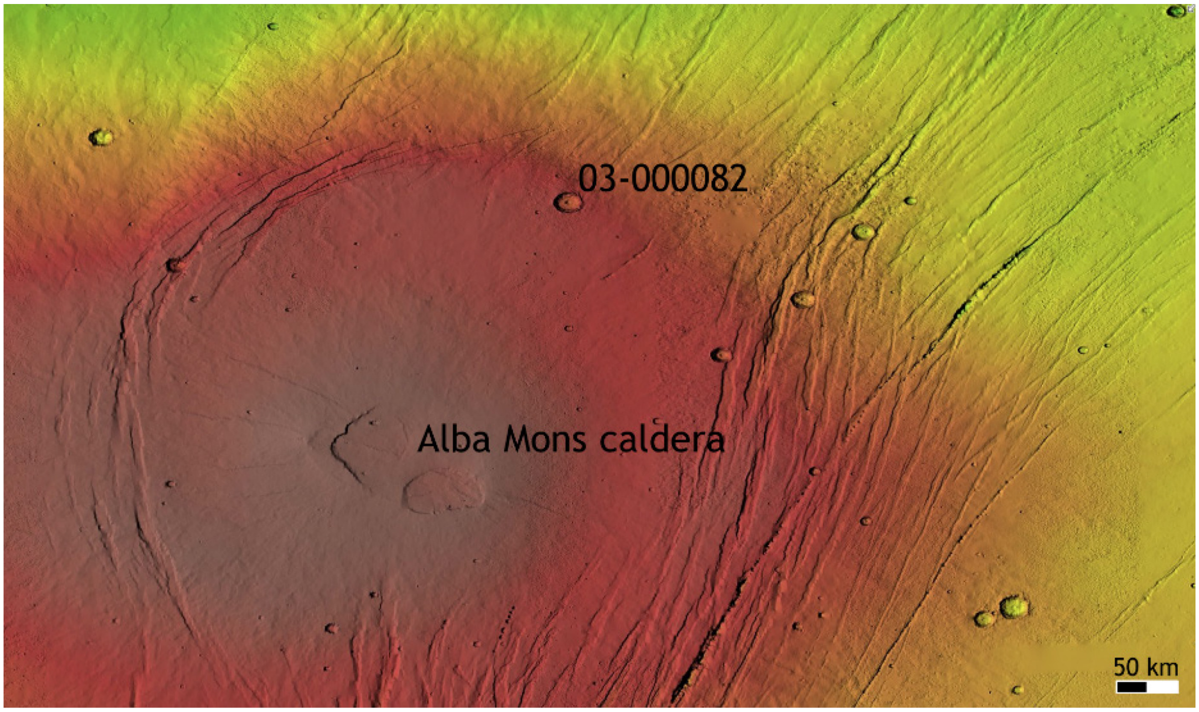

**Fig. 3.6.** MOLA-HRSC colourized shaded relief map showing crater 03-000082's location relative to Alba Mons.

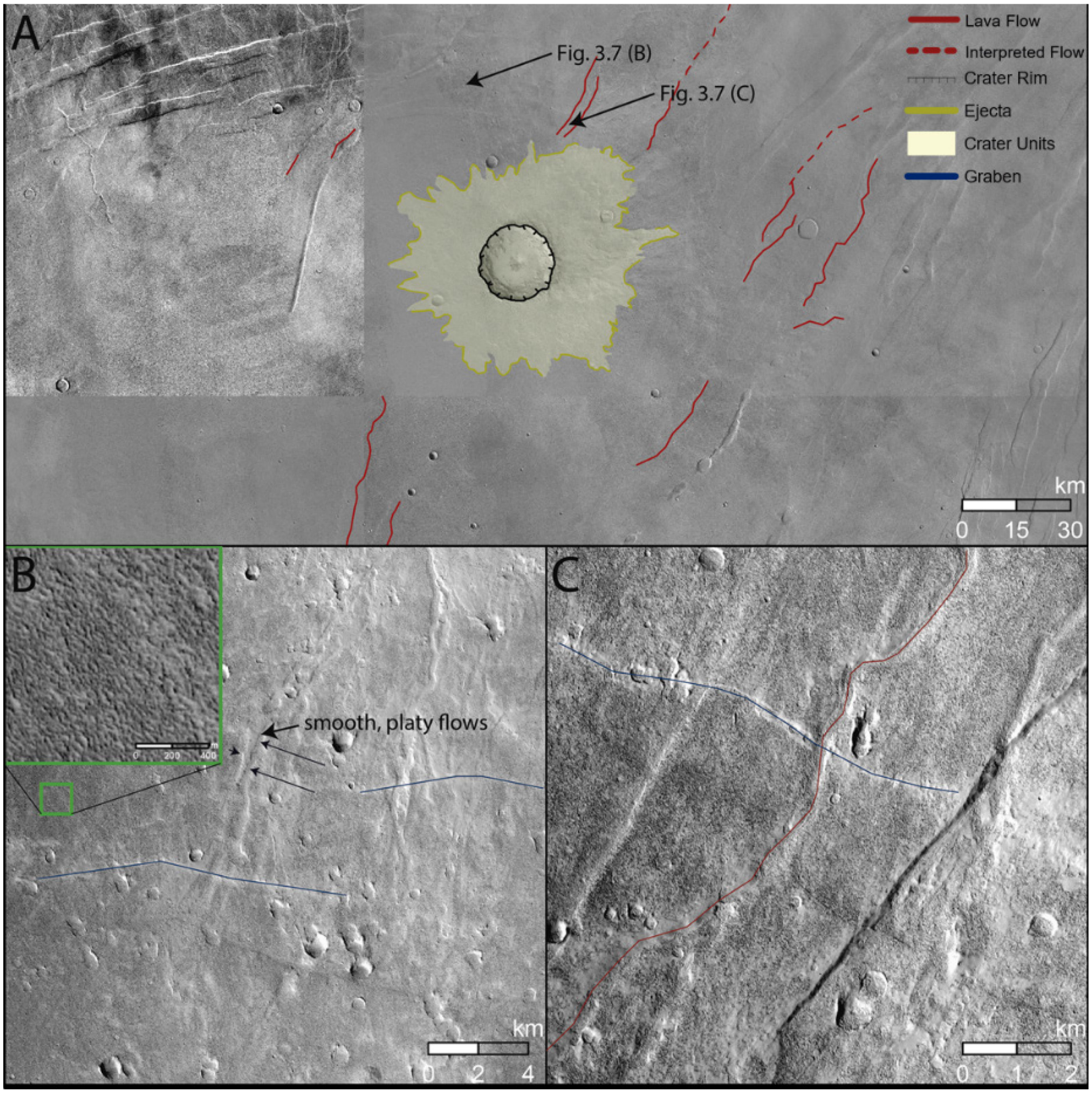

**Fig. 3.7.** (A) CTX mosaic showing an overview of crater 03-000082. Major extensional faults are present in two sets: radial to Alba Mons and approximately parallel to lava flows. Some tens of kilometers of mappable lava flows are observed on either side of the crater originating from Alba Mons. (B) CTX image (F18_042783_2270) showing smooth, platy flows near crater 03-000082 that overlay fields of wrinkled lava flows (see inset). The flows are crosscut by grabens that trend perpendicular to the smooth flows. (C) CTX image (B20_017610_2258) showing the central channel of a lava flow in red that is overlain by ejecta material from nearby craters.

## 3.3.5 09-000007

Crater 09-000007 is on the southern edge of Ceraunius Fossae within the Tharsis region of Mars (Fig. 3.8A; MC-9, Coles et al., 2019). This 22.2 km diameter crater has an asymmetrical ejecta blanket indicating that it formed by an oblique impact, likely from the northwest (Fig. 3.8A). Older bedrock material is observed on the northwestern side of the crater within the Hesperian-aged Ceraunius Fossae (McGovern et al., 2001). The crater directly superimposes these extensional faults and frequent crater pit chains and grabens surround the crater (Fig. 3.8A). A distinctive lobate flow that is nearly 50 km at its widest runs approximately parallel to the impact angle on the northeastern side of the ejecta (Fig. 3.8B), and is likely sourced from Ascreaus Mons. Additional nearby terrain is characterized by series of chaotic flow ridges with no overall trend observed (Fig. 3.8C).

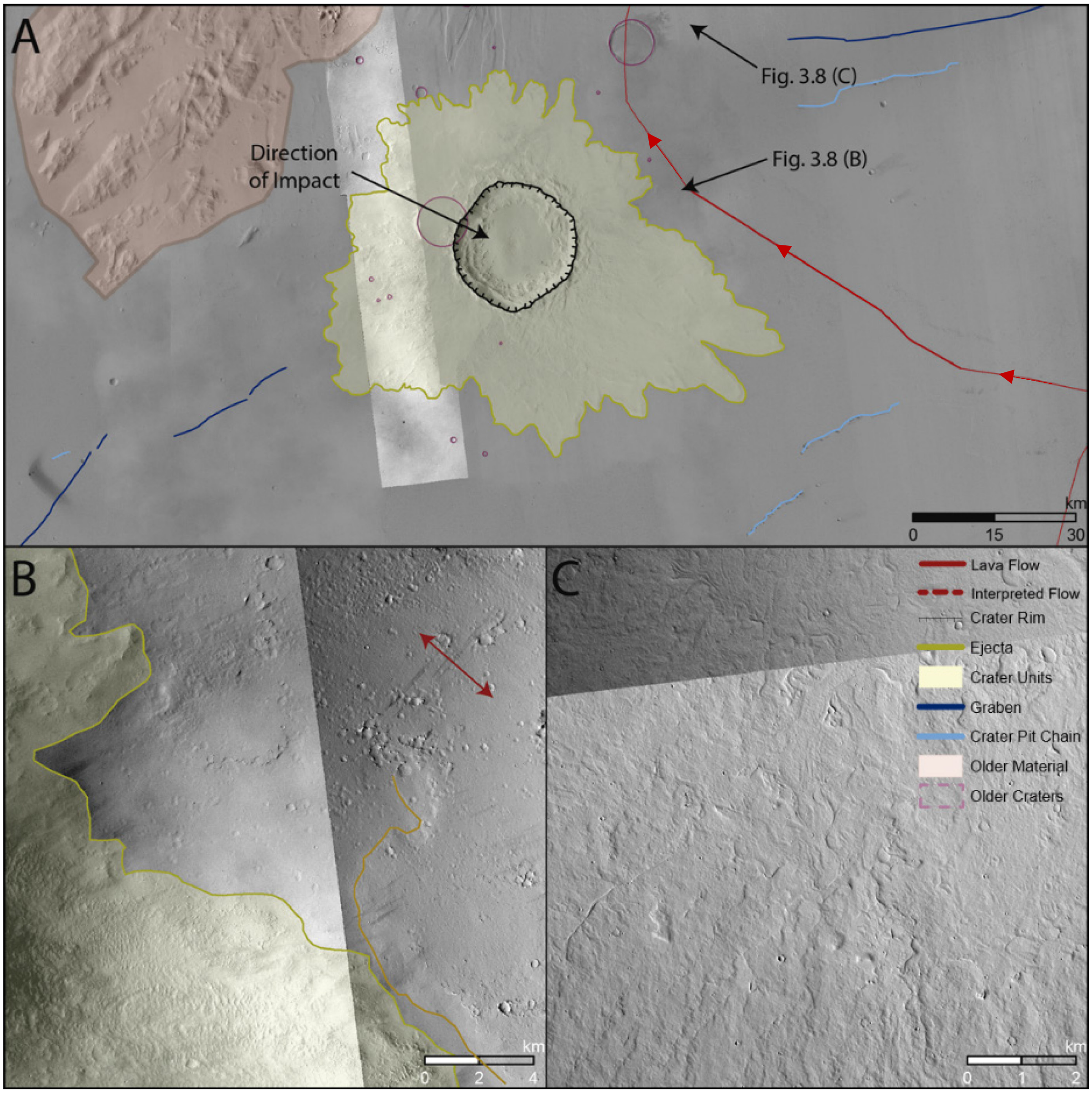

**Fig. 3.8.** (A) CTX mosaic showing an overview of crater 09-000007. This crater lies on the southern edge of fossae with frequent nearby grabens and crater pit chains, and only one major, mappable lava flow. The asymmetrical ejecta indicates that this crater formed by an oblique impact. (B) CTX images (P22_009659_1980, J05_046647_1964) showing the margins of a lava flow running parallel to the edge of the ejecta. The flow is significantly less discernable towards the northern edge of the figure as it becomes more diffuse and

is overlain by ejecta. (C) CTX images (P12_005730_1970, J05_046647_1964) near crater 09-000007 showing a series of chaotic flow ridges typical of the area.

### 3.3.6 03-000205

Approximately 400 km south of Alba Mons, contained well within Ceraunius Fossae, is crater 03-000205 (Fig. 3.9A; MC-3, Coles et al., 2019). This crater is ~12 km in diameter and superimposes a significant number of catenae, fractures, and collapse features (Fig. 3.9A). Accurate mapping of the ejecta is hindered by fossae; however, the ejecta blanket appears to have a roughly symmetrical morphology (Fig. 3.9A). Pre-dating impacts are overprinted by 03-000205 and range in size from 0.1-1.6 km diameter (Fig. 3.9A). The fossae prevent crosscutting flows from being mapped for more than a few tens of kilometers in any given area due to their having significantly less relief than the fossae (Fig. 3.9A). A kilometer-scale collapse feature is observed southeast of the ejecta with a singular channel draining down into the depression (Fig. 3.9B). Pits and associated channels post-date fractures to the west of 03-000205 as they lie within the fractures and have braided channels that are parallel to and constrained by the fractures (Fig. 3.9C).

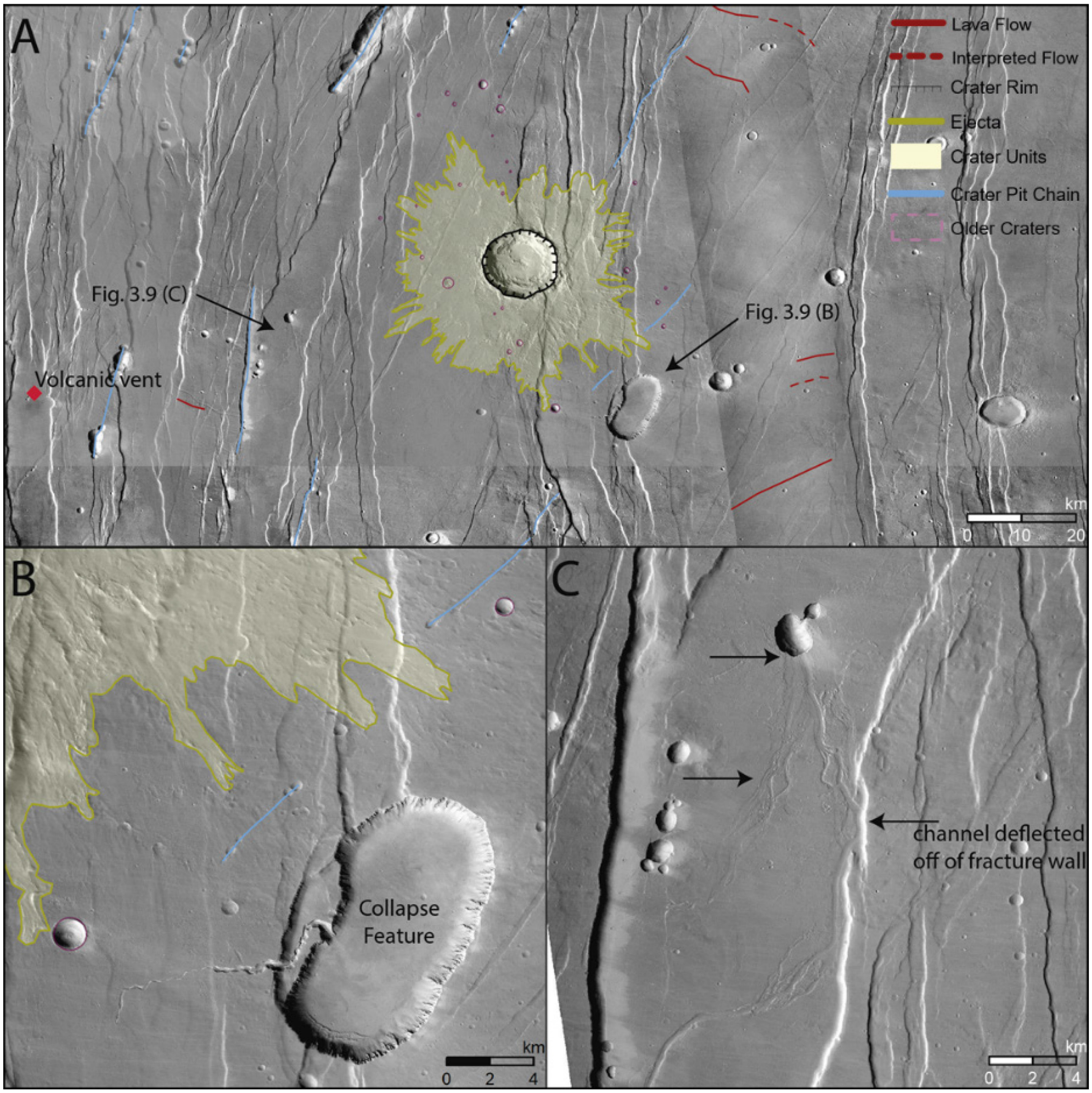

**Fig. 3.9.** A) CTX mosaic showing an overview of crater 03-000205. This crater occurs on fossae in the Tharsis region, hampering accurate mapping of ejecta and tracing of flows more than a few tens of kilometers. (B) CTX image (P14_006600_2133) showing a kilometer-scale volcanic collapse pit on the southeastern edge of crater 03-000205's ejecta. Note the channel that cuts into the eastern wall of the fossae, which appears to postdate it. (C) CTX image (P17_007813_2132) showing additional nearby collapse features. The channels emanating from these features (black arrows) are braided rather than meandering in contrast to the channel shown in (B).

### 3.3.7 09-000015

Crater 09-000015, with a diameter of 19.6 km, is located on the Tharsis plateau (Fig. 3.10A; MC-9, Coles et al., 2019), ~500 km northeast of Ascraeus Mons' caldera. A graben infilled by ejecta material crosscuts a lava flow on the northwest edge of the ejecta indicating that the graben formed sometime before the crater, but after the lava flow (Fig.

3.10C). Other lava flows trend radially away from Ascraeus Mons, one of which is observed to continue underneath the ejecta of 09-000015 (Fig. 3.10B). One pre-dating impact rests on the ejecta and is ~0.5 km in diameter; however, the surrounding terrain is otherwise unremarkable in terms of notable impact craters (Fig. 3.10A).09-000015 contains abundant, dense clusters of secondary craters near the margins of the ejecta (Fig. 3.10B/C).

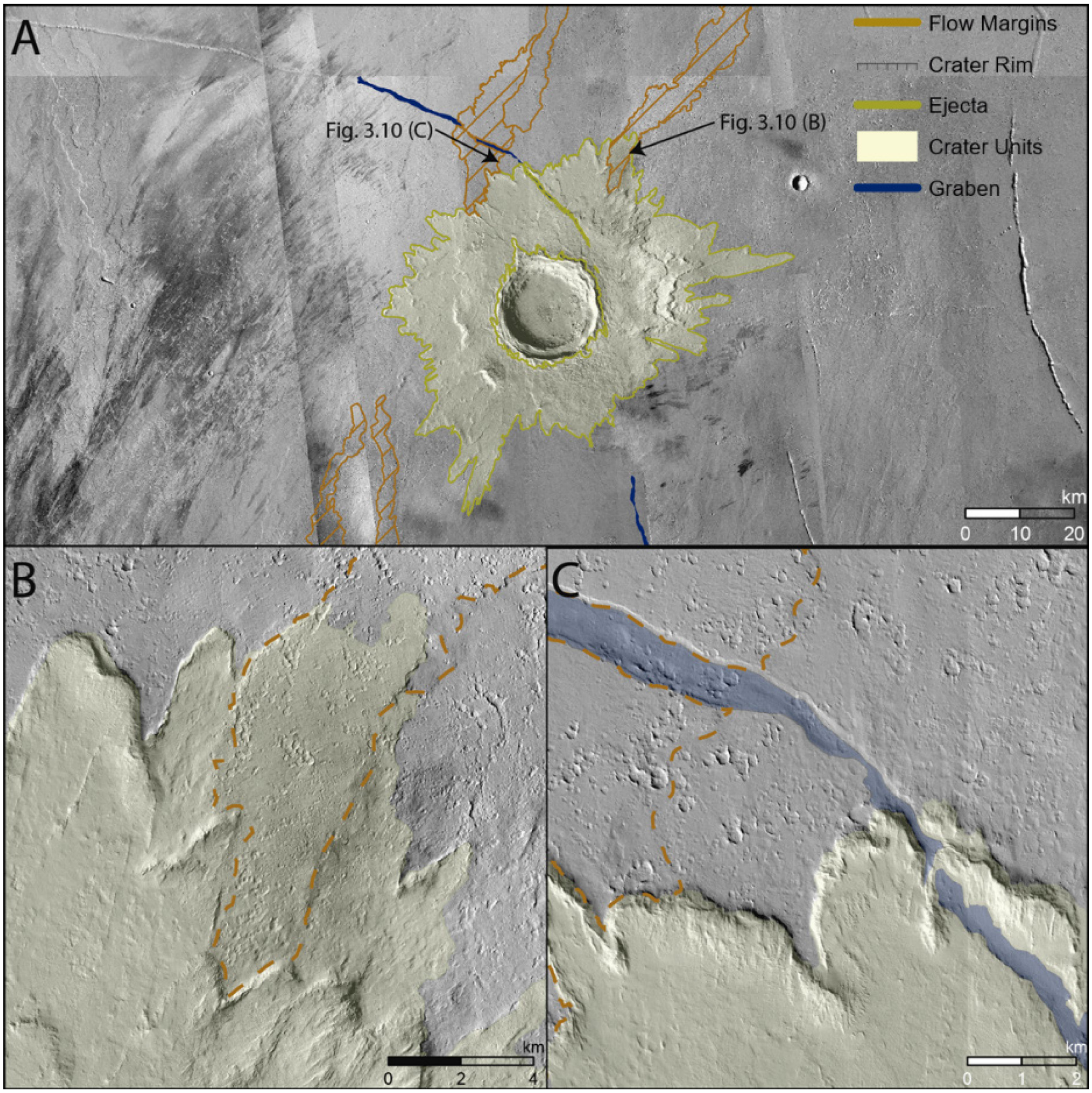

**Fig. 3.10.** (A) CTX mosaic showing an overview of crater 09-000015. (B) CTX mosaic showing a notable lava flow extending beneath the ejecta of crater 09-000015. (C) CTX mosaic showing an additional lava flow that extends beneath the ejecta of crater 09-000015. The flow is crosscut by a graben, which has been filled in by ejecta material from the impact.

Crater 09-000015 was mapped in detail (Fig. 3.11) to further assess its role as a candidate source crater. The interior is dominated by crater-related pitted deposits, and the walls are comprised of two units: exposed bedrock and talus material (Fig. 3.11). Talus material is more present on the eastern and southern edges of the crater where the walls are steeper and have not experienced major slope failure. Slumping has resulted in small, kilometer-scale terraces throughout the crater, which captured some of the melt deposits as impact melt flowed back into the crater interior during crater formation, particularly during the modification stage (Fig. 3.11). The ejecta is notably asymmetrical (Fig. 3.10A) and is inferred to have variable thickness based on the multiple overlapping ejecta layers (Fig. 3.10B).

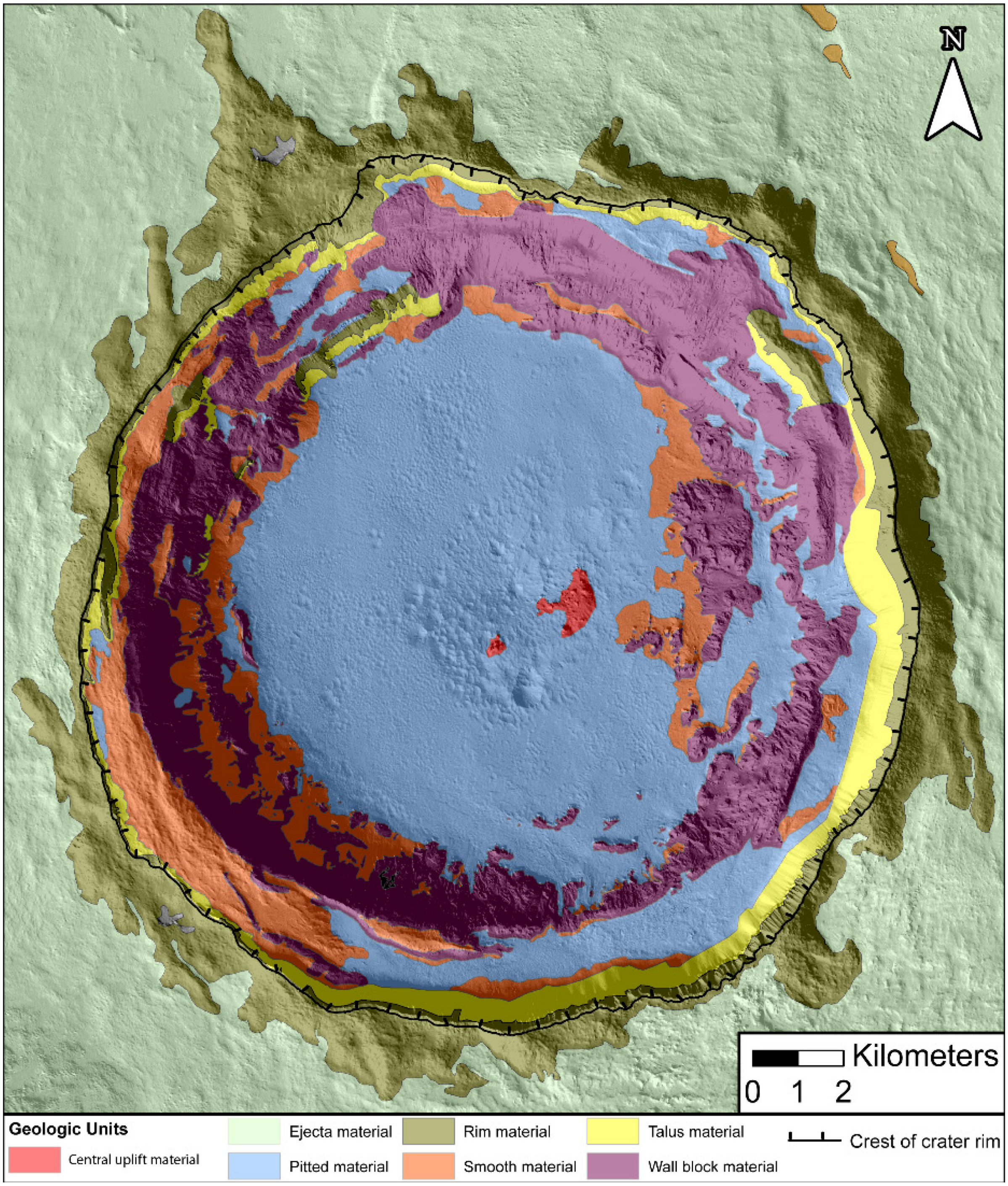

**Fig. 3.11.** Detailed mapping of the interior of crater 09-000015. A significant portion of the crater is composed of pitted material, representing melt-bearing deposits (Tornabene et al., 2012). Smooth material is the relatively bland portions of the crater floor and terrace blocks that are composed of emplaced sediments generated during impact. The orange-brown unit in the northeast portion of the map is the graben outlined in Fig. 3.10A/C.

### 3.3.8 Corinto

Corinto (D = 13.5 km) is located in Elysium Planitia (Fig. 3.12A; MC-15, Coles et al., 2019), ~500 km SW of Elysium Mons and Albor Tholus (Fig. 3.3). Lobate lava flows are found around Corinto, trending radially from Elysium Mons; however, an Albor Tholus source cannot be ruled out based on proximity. The lobate flows are superposed by Corinto's ejecta (Fig. 3.12A) and are noticeably thicker and more distinguishable than flows that are adjacent to Zunil (Section 3.3.9). This difference in flow morphology is due to Corinto's relative proximity to Elysium Mons compared to Zunil. Despite ejecta from another crater to the northeast obscuring the nearby terrain, lava flows are traceable on all sides of Corinto (Fig. 3.12A). Lava flows trend towards and away from Corinto, becoming more diffuse as they approach its ejecta (Fig. 3.12B). Surfaces to the east of Corinto show cratered flows with impacts up to a few kilometers in size that are crosscut by a fault (Fig. 3.12C). Some of the craters may be embayed by young, thin lava flows – but more analysis with high-resolution imagery is needed to confirm. Post-dating impacts from meter- to kilometer-scale are found frequently on the adjacent terrain (Fig. 3.12A).

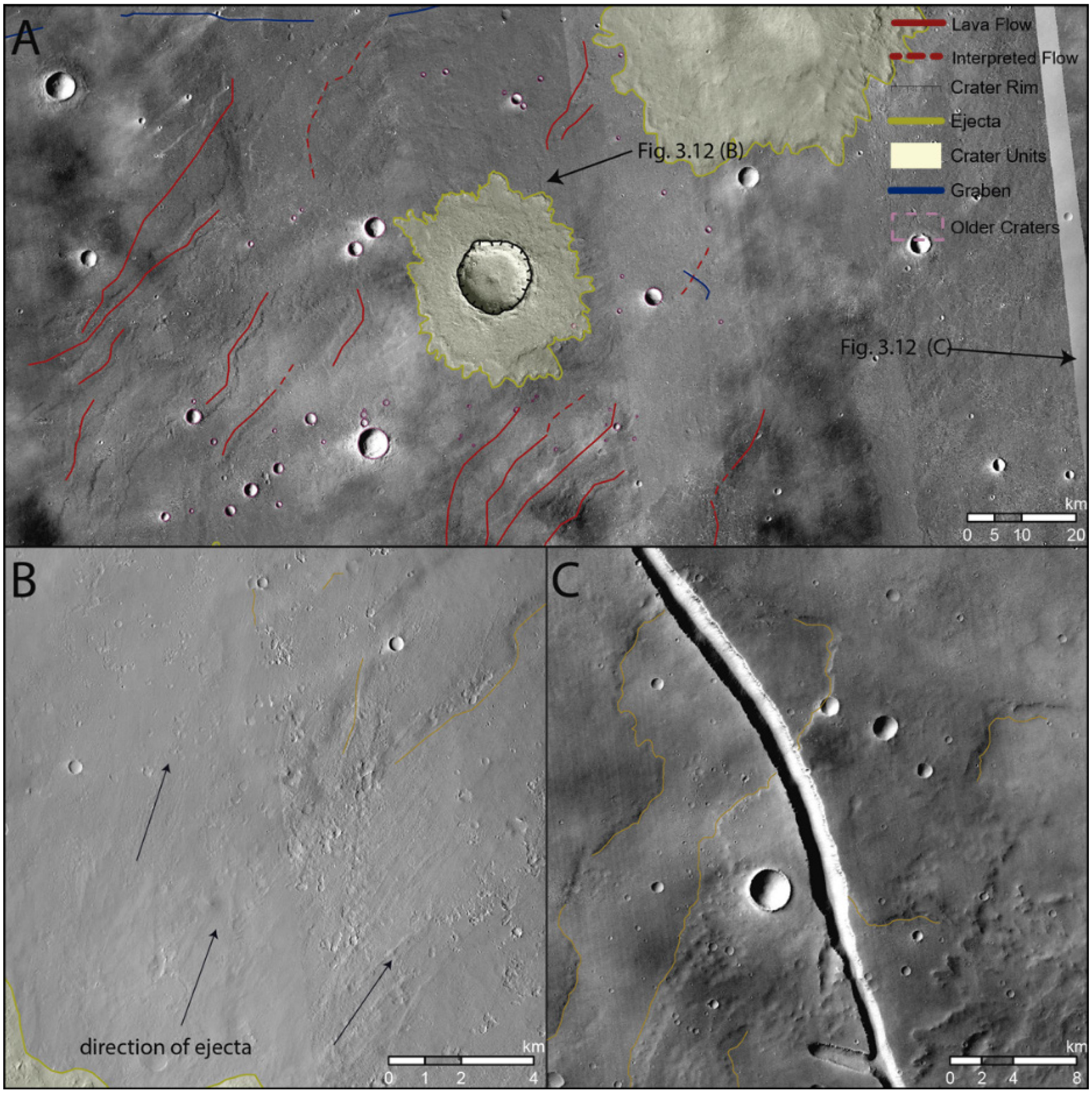

**Fig. 3.12.** (A) CTX mosaic showing an overview of Corinto. While a second, larger crater to the northeast largely obscures the terrain, many flows can be traced in a northeast-southwest direction near Corinto. (B) CTX images (J04_046229_1988, P18_007949_1971) showing the margins of two lava flows becoming diffuse outside the ejecta material originating from Corinto. (C) CTX mosaic east of Corinto showing a fault that crosscuts significant surficial lava flows that are heavily cratered by impacts up to a few kilometers in size.

### 3.3.9 Zunil

Zunil (D = 10.2 km) is one of the previously studied candidate source craters, located on the southeast corner of Elysium Planitia within Cerberus Fossae (Fig. 3.13A; MC-15, Coles et al., 2019). The location, well-preserved nature, modeled age, and thermophysical rays spanning 100's of kilometers have all led to Zunil being a favoured candidate in multiple previous studies (Tornabene et al., 2012; McEwen et al., 2005; Tornabene et al., 2006).

The surrounding Cerberus Fossae contain surface lava flows that are as young as 8 Ma (Voigt and Hamilton, 2018) overlaying an older volcanic unit that is 125-500 Ma and ≥20 m below the surface (Hamilton et al., 2010; Vaucher et al., 2009). Zunil’s ejecta is symmetrical and shows multiple layers that infill impacts that pre-date the Zunil forming event (Fig. 3.13A). Multiple lava flows are observed in the surrounding area but show no common direction and are only traceable for a few kilometers (Fig. 3.13A). The remainder of visible volcanic flows are chaotic flow ridges similar to those observed near 09-000007 (Fig. 3.13C) and larger, smooth flows such as those observed near 03-000082. A degraded crater pit chain crosscuts a series of smooth, platy flows southwest of Zunil (Fig. 3.13B). Post-dating impacts were observed by Hartmann et al. (2010) on the crater floor and ejecta; these impacts date Zunil to 0.1-1 Ma (Hartmann et al., 2010; Hundal et al., 2017).

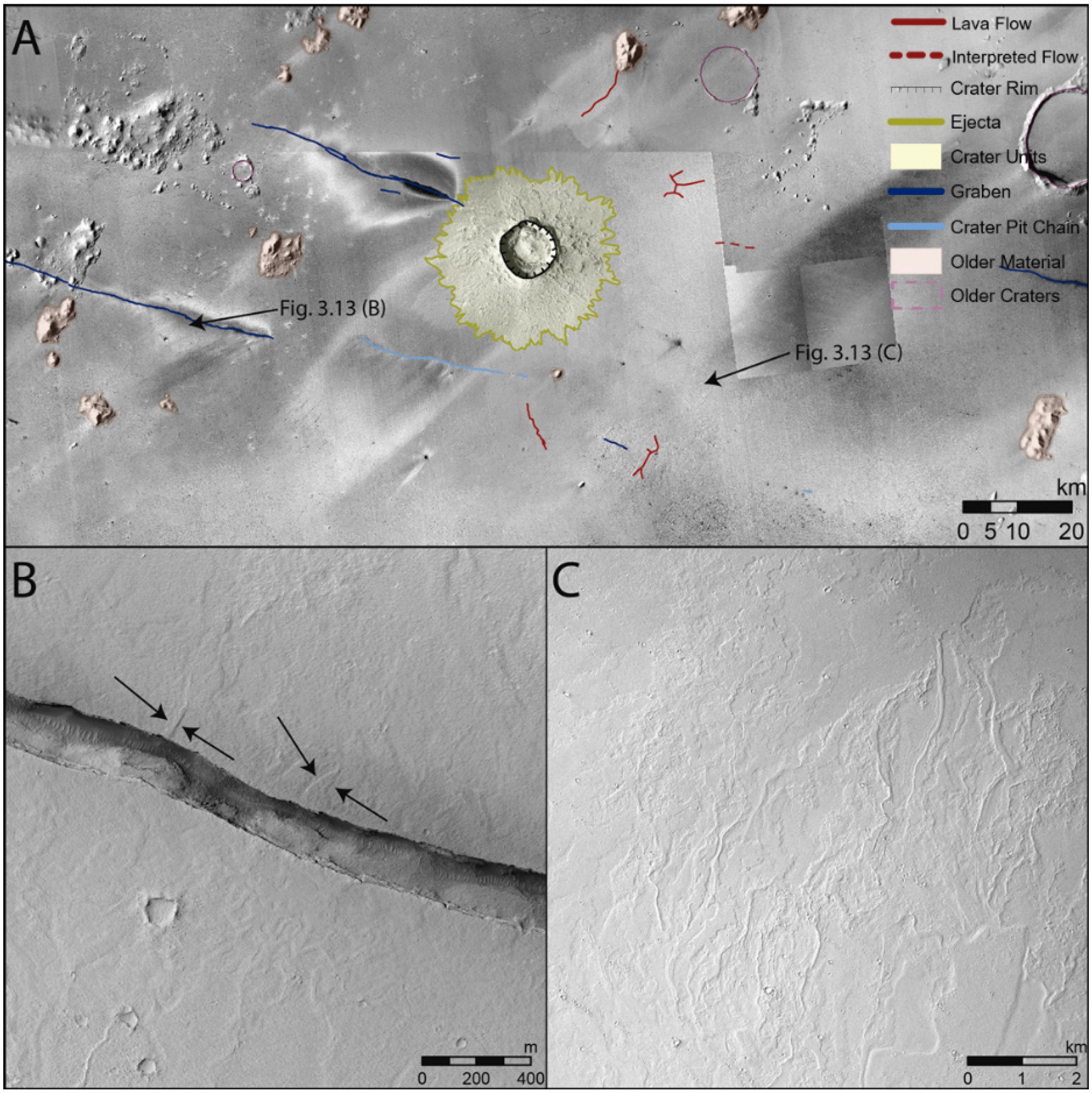

**Fig. 3.1.** (A) CTX mosaic showing an overview of Zunil and sporadic, mappable lava flows in the vicinity. (B) HiRISE image (ESP_035006_1875) showing a degraded crater pit chain, formed by the collapse of roof sections of an ancient lava tube, that crosscuts a series of decameter scale flows indicated by black arrows. (C) CTX image (B01_009939_1876) showing the different lava flow morphologies of the area including chaotic ridges similar to Fig. 3.8 (C) and larger, smoother flows. These morphologies cease to appear closer to Zunil as the terrain flattens out.

## 3.4 Discussion

The identification of the most likely source crater for a given martian meteorite is not straightforward. The approach presented here involves the combination of mapping results with literature data, with the primary goal of ranking the mapped craters from most to least likely to be the source of any of the four meteorites, Zagami, Tissint, Chassigny, and NWA 8159 (and their ejection pairs). In addition to the criteria that formed the short-list of candidate source craters in Section 3.2.1, a crater is considered a high-ranking candidate source crater if the crater:

- has a model age within the range of a specific meteorite's ejection age, and the target surface modeled ages are similar to the meteorite's crystallization age
- size is within impact modeling results based on shock analysis

Because I am identifying the best potential candidate source craters for the general characteristics of martian meteorites, I rank the youngest, most well-preserved craters the highest in terms of matching model and ejection ages. As mentioned previously (Section 3.2.1), the size range encompasses the permissible diameters for any of the four meteorites in this study. I discuss how the regional geology of the craters affects the general mechanisms of the ejection process. This includes evidence of persistent or cyclical ice and elevation as described by other studies. The highest ranking craters will have the best evidence of suitable launch conditions for any of the martian meteorites. I discuss how specific meteorites affect the generalized ranking in Section 3.4.6.

### CRATER AND TARGET SURFACE MODELED AGES

The crater must provide a young modeled age that, given uncertainties in modeled ages from the model's origin of lunar cratering rates, must be relatively consistent with the measured ejection ages of the martian meteorites (<20 Ma; Nyquist et al., 2001; 0.7-11 Ma for the meteorites in this study - Table 3.1). Additionally, the target material of the candidate crater should be consistent with Amazonian-aged lava flows consistent with the crystallization ages of the meteorites as discussed in Chapter 1.

### CRATER SIZE CONSTRAINTS

Bowling et al. (2020) provide a model of impacts into a basaltic target to provide quantitative constraints on the effective crater diameter ranges for the four meteorites considered in this study. Less coherent surface material can inhibit energy transfer and thus the overall ejection process (Bowling et al., 2020; Head et al., 2002; Fritz et al., 2005; Fritz et al., 2007). A regolith layer of at least 1 m thickness in the mid-latitude volcanic regions (Hartmann, 1999) and intermittent surficial ice in the past 20 Ma (Fritz et al., 2007) suggests that the minimum required diameter of a crater for certain launch events may be greater than indicated by modeling. However, limitations in 2-D iSALE code prohibit modeling of three-dimensional impacts (Bowling et al., 2020; Kurosawa et al., 2018). Oblique impacts, most commonly in nature at an angle of 45° (e.g. Shoemaker, 1959) are more representative of the events that are likely responsible for the ejection of martian meteorites and would increase the effective crater diameter range compared to the modeled 90° impact (Bowling et al., 2020; Kurosawa et al., 2018). A number of other, minor considerations including sub-surface information as it is related to the excavation depth modeling of the martian meteorite, climatic controls, and petrologic characteristics of the meteorites must also be evaluated. A summary of the relevant modeled crater and target surface ages can be found in Table 3.3. Here, I first rank the craters in terms of modeled formation age, and subsequently consider observed geological features associated with each crater. Modeled and relative crater ages represent the ejection age for material that may have been expelled from that particular impact and must therefore be consistent with the ejection ages of the martian meteorites themselves as determined by CRE dating. Furthermore, the modeled ages of the target surface, specifically the sampled material of the impact event, should be similar to the crystallization age of the meteorites to confirm their pairing.

**Table 3.3.** Summary of known crater and target material ages.

| Crater | Modeled Crater Age (Ma) | Target Material Age (Ma) |
|---|---|---|
| Tooting | 2.9 ± 0.3[a] | 240 – 375[a] |
| Domoni | 19.2 ± 5.3[b] | 70+[b] |
| 03-000082 | n.d. | 2000 – 2200[c,d] |
| 09-000007 | n.d. | n.d. |
| 03-000205 | n.d. | n.d. |
| 09-000015 | n.d. | n.d. |
| Corinto | 1 – 2.5[e,f] | 2 – 177[g] |
| Zunil | 0.1 – 1[h] | 2 – 177[g] |

Notes: [a]Mouginis-Mark and Boyce, 2012; [b]Viola et al., 2015; [c]Crown et al., 2020 – ages are of the western flank material of Alba Mons; [d]Crown et al., 2017; [e]Hundal et al., 2017; [f]Hartmann et al, 2010; [g]Vaucher et al., 2009; [h]McEwen et al., 2005. n.d. (no data) indicates where there is currently no published information available.

### 3.4.1 Modeled "Absolute" and Relative Crater Ages

Because geologists are unable to sample the various terrains and geologies of Mars, absolute ages of craters and geological features cannot be determined. Instead, a variety of techniques are used to approximate modeled and relative ages. The most widely cited means of providing a modeled age of a given surface, or in this case an individual martian crater, involves a determination of the areal size-frequency distribution of overprinting craters and fitting that distribution to a cratering isochron (e.g., Hartmann, 2005). Limitations to applying this method to individual craters have been outlined by McEwen et al. (2005) and Lagain et al. (2020) and are briefly discussed here. McEwen et al. (2005) argued that the crater-count chronometry systems when evaluating a young, well-preserved martian rayed crater are inconsistent. However, the inconsistencies in the system suggested by McEwen et al. (2005) were found to be the result of a lack of high-resolution imagery and a misunderstanding of the chronometry plots (Hartmann et al., 2010). Lagain et al. (2020) suggest that a constant impact rate, an assumption used in the Hartmann (2005) model, is not appropriate on martian crater-count chronometry systems. Nevertheless, these modeled crater ages are useful in comparing the relative ages of craters. There are model ages for only four of the eight craters examined in this study (Table 3.3). These ages serve as a base from which to discuss the remaining craters. Each of the crater ages in Table 3.3 use some version of the Hartmann (2005) cratering isochron to determine their ages. This is important to note because this methodology involves counting craters that superimpose the primary crater's interior or ejecta. Crater-related pitted material preservation provides better discrimination and higher fidelity for identifying the best-preserved craters on Mars rather than relying on other crater morphologic properties alone (e.g., rim sharpness, relief, ejecta preservation, floor infilling, and relative depth/diameter ratio); this is due to the fact that they are consistent with representing primary deposits formed during crater formation and the pits are amongst the first features to be degraded or obscured due to burial and/or erosion (Tornabene et al. 2012). I use the combination of these metrics to establish an initial relative age ranking (Table 3.4).

**Table 3.4.** Relative ages of candidate source craters for the meteorites in this study based on modeled crater ages and preservation (see Tables 3.1 and 3.2 for data sources). The differences between preservation and degradation are discussed later in this section.

| Relative Age | Crater | Modeled Crater Age | Preservation | Degradation |
|---|---|---|---|---|
| 1 | Zunil | 0.1 - 1 | 5 | 4 |
| 2 | Corinto | 1 – 2.5 | 5 | 4 |
| 3 | Tooting | 2.9 ± 0.3 | 5 | 4 |
| 4/5/6 | 09-000015 | n.d. | 5 | 3 |
| 4/5/6 | 03-000082 | n.d. | 4 | 4 |
| 4/5/6 | 09-000007 | n.d. | 4 | 4 |
| 7 | Domoni | 19.2 ± 5.3 | 5 | 3 |
| 8 | 03-0000205 | n.d. | 4 | 3 |

**Notes:** n.d. (no data) indicates where there is currently no published information related to the crater's age.

The first three placements are straightforward; these craters all rate at the top of both the preservation and degradation ranking and have recent crater-count ages (Table 3.4). Hartmann et al. (2010) originally suggested ages of 5-8 Ma and 2-10 Ma for Corinto and Tooting, respectively. The modeled ages suggest that Zunil is a better candidate; however, uncertainties from modeled ages necessitate the need to find other evaluation tools to more effectively rank craters. Corinto's modeled age exemplifies the uncertainties involved in crater-count chronometry, as its current estimated age range (Table 3.3) is significantly below the minimum suggested by Hartmann (2010). These uncertainties may simply be discrepancies created by different methodologies, isochron used, or inaccurate crater counting. The upper age bound of 2.5 Ma for Corinto is based on the crater superimposing young lava flows originating from the nearby Cerberus Fossae that have been dated to 2.5 ± 0.5 Ma (Vaucher et al. 2009). The minimum bound for Corinto's age in more recent work (Table 3.3) is based on the observation that Corinto is older than Zunil (Hundal et al., 2017; Golombek et al., 2014), supporting its placement below Zunil in Table 3.4. Tooting has been dated at 2-10 Ma via crater-count chronometry on the ejecta blanket and a terrace block (Hartmann et al., 2010). A more thorough investigation of the entire crater and ejecta with higher resolution imagery yielded a modeled age of 2.9 ± 0.3 Ma (Mouginis-Mark and Boyce, 2012), placing Tooting just behind the modeled formation ages of Zunil and Corinto.

Three of the four unnamed craters are presently undated and therefore share positions in the relative age component (Table 3.4). Crater 09-000015, 03-000082, and 09-000007 all superpose the volcanic terrain that they are found on and show no major subsequent impact craters in their interior or superimposed on their ejecta blanket. The preservation rank of 09-000015 is in minor conflict with its degradation rank when compared to 03-000082 and 09-000007 (Table 3.4). However, the preservation rating is chosen as a more suitable indication of its relative age as discussed in Section 3.2.1.

Domoni's model age of 19.2 Ma places it as one of the youngest craters in Arcadia Planitia (Viola et al., 2015). However, this age (19.2 Ma) is notably older than the first three placements (Zunil, Corinto, Tooting), as well as three of the unnamed candidate source craters, based on its relative degree of degradation. Crater 03-0000205 shows relatively low preservation compared to the other seven craters in this list.

### 3.4.2 Surface Ages and Geology

Target materials into which the candidate martian meteorite source craters occur represent the materials from which the meteorites were sampled. The most promising areas are those composed of mappable Amazonian-age lava flows, especially those whose craters walls, or other nearby exposures, show multiple sequences of lava flows. Such multiple stacked lava flows provide additional supporting evidence that a single impact event ejects rocks that have a range of crystallization ages. Additionally, alternating layers of coherent lava flows and slope-forming ash such as described near Tooting crater are conducive to spalling fragments at high velocity (Fig. 3.4C). This is particularly important for some martian meteorites that are grouped by CRE age yet have vastly different crystallization ages. For example, NWA 8159 has a crystallization age of ~2370 ± 250 Ma and an ejection age of 1.2 ± 0.1 Ma. A small suite of other basaltic martian meteorites have crystallization ages ranging from 327 – 2403 Ma with ejection ages of ~1 Ma (Lapen et al., 2017). Stacked lava flows may represent a single impact event responsible for some, or most, of these meteorites with a shared ejection age representing a singular impact event (Lapen et al., 2017; Cohen et al., 2017). The suite of meteorites in this study cover a range of crystallization ages (Table 3.1) representative of all martian meteorites. This criterion is discussed to evaluate the probability of a given crater being a source for a specific type of martian meteorite or group of meteorites. Martian meteorites fall into several distinct age ranges spanning all geologic areas on Mars: <716 Ma, ~1.3 Ga, 2.4 Ga, 4.1 Ga, and a breccia of ~1.5 Ga containing clasts up to 4.5 Ga (Udry et al., 2020). Comparing the target surface characteristics for the eight candidate source craters provides insight into the diversity of geologic units, morphologic differences and similarities between craters located in a variety of volcanic regions, and effects on impact modeling.

Tooting crater has been mapped at a scale of 1:200,000 as its unique location on unremarkable terrain provides a clear picture of a well-preserved crater with minimal degradation (Mouginis-Mark and Boyce, 2012). Thirteen craters superimpose Tooting's ejecta blanket, totaling an area of ~8120 km$^2$. These craters have been used to provide an approximate model age of Tooting of 2.9 ± 0.3 Ma (Mouginis-Mark and Boyce, 2012). A series of stacked lava flows are observed in the lower of three distinct units in the crater wall (Mouginis-Mark and Boyce, 2012). The exposed section of at least 4 and as many as 5 coherent layers in both the crater wall and that of a nearby pit suggest that the presence of thinly stacked flows is continuous in the area and not a phenomenon unique to the crater. Caudill et al. (2012) find that continuous layered lava flows are found in the walls and uplift material of craters throughout the major volcanic regions. The lava flows are alternated by less coherent layers, analogous to terrestrial layered sequences of flood lavas and pyroclastic layers – similar to what I note in Tooting crater (Caudill et al., 2012).

Zunil samples material from Elysium Planitia, within an area that contains thin, decameter-scale Amazonian lava flows (Hartmann and Berman, 2000). These lava flows are characteristically similar to those present nearby Tooting despite having a different source. The sequence of nearly horizontal layers at the bottom of the crater wall in Tooting crater are interpreted to be uplifted lava flows and are part of the sampled material (Mouginis-Mark and Boyce, 2012). Lava flows in the Zunil region have a similar morphology and decameter thickness but are interpreted to be upwards of a magnitude more recent in age (Mouginis-Mark and Boyce, 2012; Hartmann and Berman, 2000). It is likely that the stacked flows in this region continue through Zunil itself, but none are discernable in the crater walls or nearby geological material. This could be due to several factors including the small size and depth of this impact, and talus coverage of its steep crater walls. Corinto samples material from areas with similar volcanic sources, although less that is directly attributable to Cerberus Fossae. Vaucher et al. (2009) highlight active volcanic periods from between 2 – 250 Ma in Elysium Planitia. The target materials of either Zunil- or Corinto-forming impact events may be from any of the active volcanic periods within this range depending on the depth from which the material was sampled and the thickness of the volcanic units. The emplacement chronology has been studied in more detail to provide an extensive history of the volcanic history of the region (Voigt and Hamilton, 2018). In an area ~300 km east of Zunil, Voigt and Hamilton (2018) emphasize two primary volcanic units superimposing the bedrock. An initial volcanic unit with a thickness of ≥20 m and an age of 125 – 500 Ma is overlain by flood lava flow ≥20 m with a modeled surface age of 20 Ma. While the study area does not directly encompass Corinto or Zunil, the relative thicknesses and ages of volcanic material at this distance from its origin in the Cerberus Fossae brings to light an important point. Even when considering an uncertainty factor of 3-4X, no martian meteorites show crystallization ages as young as 20 Ma (or 80 Ma with the uncertainty factor), thus would be unlikely to be sampled from the surface units of this region (Tornabene et al., 2006). Materials in the 125 – 500 Ma range, relevant to many of the shergottites (Udry et al., 2020), could have been excavated from the near-surface units of Elysium Planitia, provided a decameter scale excavation depth. The older meteorites - NWA 7635, NWA 8159, Chassignites, and Nahklites - would only be sourced from Elysium Planitia given an excavation depth of at least 40 m. As an alternative, I propose that these older meteorites were sourced from elsewhere on Mars, most likely from somewhere within the Tharsis region.

The target materials for crater 09-000015 and crater 09-000007 are dominated by volcanic flows sourced from Ascraeus Mons. Crater 09-000007 has some volcanic material that originates from sources to the west as well, but the major flow adjacent to this crater (Fig. 3.8A) sources from Ascraeus Mons and is also the youngest of the major volcanic features in the area. The evident asymmetry of the ejecta blanket (Fig. 3.8A) provides insight into the impact direction and suggests that the impact itself was oblique. This asymmetric ejecta blanket is the most apparent of all the candidate source craters examined in this study. Lava flows that are hundreds of kilometers long dominate the terrain north of Ascraeus Mons and are observed to layer atop one another (Fig. 3.10A). The flow that is overlain by the ejecta from crater 09-000015 indicates that this crater is at least as old as the volcanic activity responsible for this flow. Evidence of extended glacial activity in Tharsis in the range of 25 - 600 Ma, and specifically on the Ascraeus Mons fan-shaped deposit at ~220 Ma, overprinted by volcanic material suggests that volcanic episodes have occurred up until recently (Kadish et al., 2008; Kadish et al., 2014).

Crater 03-000205's occurrence among the Hesperian-aged fossae creates unique challenges when making interpretations (Coles et al., 2019). Collapse features associated and related to the fossae, as well as individual fluvial pits and channels from within the fossae, suggest that this region has been active more recently. A small volcanic vent within one of the fossae southwest of 03-0000205 also indicates surface activity more recently than the formation of these major stress faults. However, of the notable volcanic flows in the area, all are crosscut by the fossae. The lack of major flows superimposing the fossae suggests there has been little to no major volcanic activity in the area in recent times. Ejecta material on the eastern half of the crater infills and superposes the fossae.

Crater 03-000082 is the only candidate source crater found on the flank of a volcano, within lava flows emanating from Alba Mons. It is unclear if the flows associated with 03-000082 originate from the caldera itself, or from vents or fissures on the lower flank that have since covered themselves (Cattermole, 1987; Schneeberger and Pieri, 1991; Crown et al., 2020). Model ages from crater-count chronometry on the western flank of Alba Mons indicate that these geologic units are 1.8 ± 0.4 – 2.2 ± 0.3 Ga (Crown et al., 2020). Alba Mons shows evidence of fluvial valleys and features from ice-rich bodies (e.g. polygonal cracks, ring-mold craters) that suggest extensive reworking from glacial episodes, including those as recent as ~10 – 100 Ma (Crown et al., 2020; Sinha and Vijayan, 2017). Only martian meteorites NWA 7635 and NWA 8159 are of similar age to the igneous terrain of Alba Mons superimposed by crater 03-000082.

Domoni is the highest latitude candidate source crater discussed in this study (Table 3.2). There is widespread evidence of northern mid-latitude ice and glaciation on Mars (Madeleine et al., 2009), and it can be assumed that there is greater and more recent glacial activity in the northern latitudes (>60°). This assumption is exhibited by the contrast between the smooth lava flows near craters such as Tooting (Fig. 3.1B) and 09-000015 (Fig.

3.10B) compared with the worn, degraded surface adjacent to Domoni (Fig. 3.5B). The primary features of this worn surface are abundant periglacial landforms and circular pits that are similar in morphology to small impact craters with one notable exception; the pits lack the raised rims of a well-preserved impact crater (Fig. 3.5B). This observation complicates crater-count chronometry because older primary impacts may no longer have a raised rim as they become degraded over time. The pits, interpreted to primarily result from thermal cracking of permafrost and subsequent sublimation within the cracks, vary in age and distribution (Kostama et al., 2006). Some pits cut into the icy mantle material, while others are overlain by it, some show signs of a collapse origin while others do not, and while the regional distribution contains dense clusters, there are also randomly distributed pits (Kostama et al., 2006). The Viola et al. (2015) estimate of 19.2 ± 5.3 Ma for Domoni may have far greater uncertainty than stated because of the pitted terrain. Domoni's interior was not included in the crater-count chronometry, and recent processes may erase or degrade small craters beyond recognition (Viola et al., 2015). Indeed, Viola et al. (2015) suggest that the provided model age may be better suited as a minimum age of Domoni. The observations of the local geology and volcanic history of the region in this study are consistent with the minimum age interpretation.

### 3.4.3 Other Considerations

Launch conditions of martian meteorites are primarily constrained by the geology and age of candidate source craters, as discussed in previous sections. Here, I consider several other factors that impact the likelihood of ejection from a given crater. These factors include climate, elevation, and burial depth. Burial depth is related to individual meteorites and will be discussed in a later section (3.4.6) relating specific meteorites to specific craters.

A clustering of martian meteorite ejection ages that are <5 Ma raises questions about the climatic controls on impact ejection, as discussed by Fritz et al. (2007). An increase in the mean obliquity of Mars of over 10° occurred between 5-20 Myr, leading to tropical glaciers in the Tharsis, Olympus, and Elysium regions with thicknesses of several hundred meters and localized snow and ice deposits in the decameter range (Fastook and Head, 2014). While thick ice coverage would hinder martian meteorite ejection, the subsequent retreat could expose fresh, rigid lithologies characteristic of martian meteorites. These newly exposed surfaces are especially frequent at higher elevations, from where the ice would initially retreat.

At higher elevations, such as the Tharsis bulge, atmospheric pressure is 2.3 times lower than that at Mars datum (Fritz et al., 2007). This higher elevation would increase the likelihood of small impacts producing martian meteorites (Fritz et al., 2007). Global atmospheric pressure can vary by upwards of 80 mbar. The variation of atmospheric pressure is dependent on volatile availability in the regolith, polar cap, and atmospheric reservoirs (Fritz et al., 2007). During times of greater atmospheric pressure, such as during a climate shift that has been inferred to have occurred 5 Myr ago, small impact events are only able to eject a small portion of total material compared to times of lower atmospheric pressure (Fritz et al., 2007).

### 3.4.4 Prioritization of Candidate Source Craters

The eight candidate source craters are ranked according to their probability of being a source of any of the four martian meteorites. Criteria for the ranking include both relative results, in the form of crater-count chronometry, and qualitative observations of the igneous context and general geology of the crater and nearby area, as discussed in previous sections. Our discussion of crater ranking starts from the least probable (Domoni) to the most probable (Zunil).

Domoni is located in Arcadia Planitia, which shows the persistence of ice over large time scales (Viola et al., 2015), contrary to the periodic cycles at mid-latitudes caused by obliquity (Fritz et al., 2007). The presence of an ice layer inhibits launch events (Fritz et al., 2007) and therefore reduces the likelihood of Domoni as a candidate crater. Crater-count chronometry provides a model age of the nearby surface that is >70 Ma (Viola et al., 2015), while the volcanic material source from Alba Mons is likely to be more than an order of magnitude older at 1.8 ± 0.4 – 2.2 ± 0.3 Ga (Crown et al., 2020). Domoni shows the advantage of incorporating a variety of factors in evaluating candidate source craters; its preservation level of 5 (Tornabene et al., 2012) suggests that it is much younger and more of a probable candidate than is presented here. Pits created by recent glacial activity in the region as observed on surfaces near Domoni may have affected the preservation of pitted material within the crater itself (Kostama et al., 2006). This post-impact reworking of pitted material would hinder the use of pitted material to determine Domoni's relative age.

Crater 03-000205 is relatively more degraded than other craters in this study (Table 3.3) and the major volcanic flows are crosscut by Hesperian aged fossae (Coles et al., 2019). The lack of recent major volcanic activity in the region, noting that smaller, more recent episodes are not ruled out, contributes to its lower ranking. The crater itself appears more degraded than Domoni, but as already mentioned, this is not a deciding factor on its own. With a lower latitude and the presence of ice being more episodic (e.g. Fritz et al., 2007) than persistent in this region, 03-000205 is more likely to represent suitable meteorite ejection conditions than Domoni.

The position of 03-000082 in our ranking is primarily due to the inactivity of Alba Mons in recent history (Crown et al., 2017; Crown et al., 2020). While the crater itself appears to be very well-preserved – like some of the candidate craters with modeled ages (e.g., Zunil and Corinto), it is therefore likely to be comparably young and would fit with the timing of martian meteorite ejection; however, volcanic flows (1.8 ± 0.4 – 2.2 ± 0.3 Ga; Crown et al., 2020) on the surface are significantly older than many of the crystallization ages of martian meteorites. Additionally, sampling of martian meteorites occurs just below the free surface (Melosh, 1984; Melosh, 1985; Vickery and Melosh, 1987; Head et al., 2002; Artemieva and Ivanov, 2004), therefore, the material sampled by an ejection at this site is likely older than those of the surface flows. Some meteorites, notably NWA 7635 and NWA 8159 at ~2.4 Ga (Lapen et al., 2017; Herd et al., 2017) fit within these crystallization constraints. However, as a source for any martian meteorite and the bulk of martian meteorites being <716 Ma (Udry et al., 2020), 03-000082 is not the ideal candidate in this list.

Craters 09-000015 and 09-000007 are both placed at the 4th ranking on the list because these craters share common attributes that did not allow us to delineate between their likelihood as source craters based on the criteria considered. They both derive volcanic material from Ascraeus Mons, have significant lava flows nearby, and are well preserved. 09-000015 has significantly more mappable flows adjacent to the crater (Fig. 3.10A) than 09-000007, including some which are mapped to continue beneath the ejecta. However, the high number of mappable flows near 09-000015 is most likely due to its nearer proximity to Ascraeus Mons compared to 09-000007. These two craters are suitable for recent ejection as they are located at a higher elevation on the Tharsis bulge (Fig. 3.3 and their high degree of preservation suggests they formed by relatively recent impacts. A moderate crater diameter (Table 3.2) may increase the amount of unique materials sampled, due to the relatively larger volume of material within the spall zone, as discussed in Chapter 1. This observation makes craters 09-000015 and 09-000007 contenders for releasing many meteorites from a single event, as suggested by Lapen et al. (2017). However, with little to no relative or modeled age constraints available on the nearby terrain, Ascraeus Mons, or the craters themselves, it cannot be confidently stated that these craters are more likely sources for any of the martian meteorites.

Tooting, Corinto, and Zunil all share many of their martian meteorite source features. These three craters occur on recent lava plains at higher-than-datum elevations, are well-preserved, and their nearby terrain is consistent with the age of the bulk of martian meteorites. While matching crater-count chronometry (i.e., modeled ages) for candidate craters with ejection ages is not recommended without considering all the uncertainties, it can help pin down their approximate ages when they show similar levels of preservation. In this case, crater-count chronometry is applied to rank these three craters with Zunil being the youngest and most probable crater, and Tooting being the oldest and least probable crater of the three. It is important to note that for specific meteorites these three rankings may change, but on the premise of the most ideal candidate for any martian meteorite, the ideal candidate, all else being equal, is the youngest crater. The finalized rankings are presented below in Table 3.5.

**Table 3.5.** Ranking of candidate source craters being the source of any martian meteorite.

| Rank | Crater |
|---|---|
| 1 | Zunil |
| 2 | Corinto |
| 3 | Tooting |
| 4/5 | 09-000015 |
| 4/5 | 09-000007 |
| 6 | 03-000082 |
| 7 | 03-0000205 |
| 8 | Domoni |

### 3.4.6 Launch Events for Specific Meteorites

Determining the most probable candidate source craters for specific martian meteorites requires evaluating more factors including burial depth (e.g. Warren, 1994; Artemieva and Ivanov, 2004; Fritz and Greshake, 2009; Bowling et al., 2020) and emplacement and petrologic constraints (e.g. Treiman, 2005; Daly et al., 2019; Cohen et al., 2017). Cosmic ray exposure studies, surface regolith layers, and near-surface ice suggest that martian meteorites are ejected from depths that vary from immediately below the regolith to upwards of 250 m (Artemieva and Ivanov, 2004; Fritz et al., 2007; Fritz and Greshake, 2009). Modeling results from the four meteorites in this study suggest a maximum burial depth of 50 m (Table 3.6).

**Table 3.6.** Pre-impact burial depths of the four meteorites in this study as per modeling results from Bowling et al. (2020) and Herd et al. (2018).

| Meteorite | Burial Depth (m) |
|---|---|
| Zagami | < 6 |
| Tissint | < 50 |
| Chassigny | < 25 |
| NWA 8159 | < 25 |

When accounting for traits specific to a given meteorite, the candidate source crater ranking changes, compared to the ranking presented in the previous section. Zagami's relatively young crystallization age (177 ± 3 Ma; Table 3.1) and near-surface origin based on petrology and impact modeling (Table 3.6), suggest that the recently active flows in Elysium Planitia near Zunil and Corinto are more probable sources. Craters such as Domoni, with a significant regolith layer and subsurface ice, or crater 03-000082 and its significantly older volcanic flows, are less likely sources for Zagami. However, crater 03-000082 becomes more of a probable source when evaluating this crater as a source for older meteorites such as NWA 8159 (~2.4 Ga; Herd et al., 2017) or the nakhlites and chassignites (~1.3 Ga; Udry et al., 2020). Small changes to the initial queries bring additional craters not evaluated in this study to the discussion. The low end of effective crater diameter ranges of Chassigny and NWA 8159 (Table 3.1) are only restricted by general launch mechanisms (Head et al., 2002). These small impacts generally occur more frequently and recently than large impacts (Hartmann, 2005) suggesting other craters including Gratteri (Quantin et al., 2016) and Zumba (Chuang et al., 2016) as potential, and probable, sources. Indeed, characteristics from a specific martian meteorite or group of meteorites can dramatically alter the list and ranking of candidate source craters. Nevertheless, this study offers the most probable candidate source craters for any of the current shergottites in the world's collection.

## 3.5 Conclusions

Mapping of candidate source craters for martian meteorites has provided insight into the probability of a given crater being the source for either any or a specific martian meteorite. A general approach to the source crater problem was developed to deliver more targeted studies. By using the query-based methodology in this study to initially limit candidate craters of interest for a given meteorite, results for a specific meteorite or group of meteorites can be refined. Mapping of the crater and surrounding terrain in conjunction with the relative ages of craters, and understanding factors such as burial depth (Artemieva and Ivanov, 2004; Bowling et al., 2020), and petrologic and geochemical constraints (e.g.

Treiman, 2005; Daly et al., 2019; Cohen et al., 2017) alleviates the limitations and uncertainties of other approaches (e.g. Werner et al., 2014; Ody et al., 2015; Kereszturi and Chatzitheodoridis, 2016).

Results from the mapping of the most well-preserved candidate source craters reveal that the previously studied craters Zagami, Corinto, and Tooting (McEwen et al., 2005; Tornabene et al., 2006; Tornabene et al., 2012; Mouginis-Mark and Boyce, 2012; Golombek et al., 2014) are the most probable sources of at least some of the martian meteorites. Two craters in the Ascraeus region, 09-000015 and 09-000007, present promising characteristics as possible sources for martian meteorites, but further work to constrain surface ages is required to identify the meteorite(s) that most likely sourced from this region. Not all craters in the ranking scheme are probable candidates for all martian meteorites, and, conversely, some craters missing in the ranking are probable candidate sources for specific martian meteorites. Other factors unique to individual and groups of martian meteorites can further constrain the list of candidate source craters for those meteorites. Previously studied candidate source craters and potentially useful variables for future studies will be discussed in the next chapter.

# Chapter 4. Future Work for Martian Source Craters and Conclusions

As discussed in Chapter 1, linking martian meteorites to their source craters will greatly increase their scientific value. While the constraints placed in Chapter 3 and subsequent mapping and prioritization of candidate source craters provided significant progress in pursuit of this goal, there is still much work to be done. In this chapter, I will address previously studied candidate source craters that did not receive consideration as part of this study. Additionally, I will outline key components for the continuation of this research and provide a summary of the findings in this study.

## 4.1 Other candidate source craters and future work

In the previous chapter, I noted that craters that did not appear as candidate source craters for martian meteorites based on our methodology were not necessarily ruled out as a potential candidate. As stated in Section 3.4.6, making minor changes to the query to account for individual meteorite characteristics can have noticeable changes to the resulting list of craters. Two craters, Gratteri and Zumba, did not make the finalized list but are excellent candidate source craters for those meteorites which have impact modeling results that include craters that are <8 km diameter.

Gratteri is a 7 km diameter crater in southern Tharsis that is noted for the strong contrast of its thermophysical rays (Quantin et al., 2016). This crater is estimated to have formed ~0.8 Myr ago, making it younger than all the craters in this study other than possibly Zunil (Quantin et al., 2016; Hundal et al., 2017; Vaucher et al., 2009; McEwen et al., 2005). Quantin et al. (2016) focused on how the secondary crater field affects the size-frequency distribution on crater-count chronometry systems. The observations of this study find that vast quantities of secondary craters found in tandem with small, fresh impact craters do not negatively impact the effectiveness of crater-count chronometry systems (Quantin et al., 2016). In fact, the presence of secondary craters is suggested to provide useful evidence to distinguish young geological formations from significantly older geological features (Tornabene et al., 2006; Quantin et al., 2016). More work on the age of lava flows near Gratteri is needed to evaluate its potential as a candidate source crater; however, its recent impact age (~0.8 Ma) is encouraging as this age aligns with CRE ages for many recently ejected shergottites, including Tissint and potentially Northwest Africa (NWA) 8159 (Table 3.1; Udry et al., 2020).

Another compelling candidate source crater that was not discussed in detail in Chapter 3 is Zumba. Zumba is a ~2.9 km diameter crater in southern Tharsis that was excluded from this study because its small diameter is not consistent with the impact modeling of Zagami and Tissint (Table 3.1). Zumba – like Gratteri and Zunil – is noteworthy because of the prominent thermophysical rays that it exhibits. Chuang et al. (2016) mapped 13,064 secondary fields yielding ~352,000 secondary craters and several interesting conclusions. Detailed mapping and counting of primary craters resulted in a model age of 2.3 ± 1 Ma for Zumba crater and ~580 ± 100 Ma for the lava flows sampled by this impact (Chuang et al., 2016). The crystallization age, impact age, and composition of Zumba crater are consistent with the characteristics of many shergottites (Chuang et al., 2016; Udry et al., 2020; Nyquist et al., 2001). However, none of the four meteorites from this study have characteristics that make them potential matches for Zumba crater. Zagami's ejection age is similar to the impact age of Zumba, but its younger crystallization age and near-surface burial depth hinder arguments that Zumba is a good fit for this meteorite (Table 3.1; Table 3.5; Chuang et al., 2016). Additionally, as previously mentioned in this section, both Zagami and Tissint have impact modeling that is incompatible with the diameter of Zumba crater. Even without consideration for impact modeling, Tissint's crystallization age is consistent with the lava flows sampled by Zunil but its ejection age is less than half that of the modeled age for the Zumba impact (Table 3.1; Chuang et al., 2016). Both Chassigny (~1.3 Ga) and NWA 8159 (~2.4 Ga) are significantly older than material sampled by Zumba crater, and it is unlikely that deeper flows of at least 1 Ga were sampled in an impact resulting in a ~2.9 km diameter (Table 3.1; Chuang et al., 2016). This inference is based on the observation that the depth of an impact structure is less than half its diameter (e.g. Tornabene et al., 2018). While Zumba crater is not a good fit as a source for the martian meteorites considered in this study, its morphological features and geological context retain this crater as a strong candidate for other shergottites (Chuang et al., 2016; Udry et al., 2020).

The identification of thermophysical rays and evaluation of size-frequency distributions of secondary craters is outside the scope of this study, but are important factors when evaluating candidate source craters. I will now discuss several other notable variables related to the continuation of evaluating candidate source craters.

Mars has a significant layer of windblown dust that obscures orbital remote sensing instruments from obtaining accurate data (Christensen et al., 2001). However, fresh impact craters and faulting in crater walls disturb this dust layer providing windows to the geological material below (Viviano et al., 2019). These windows allow orbital instruments to determine spectral signatures, from which compositions of Amazonian-aged volcanic terrain on Mars can be derived. Viviano et al. (2019) positively identified 103 areas of exposed mafic rock throughout Tharsis and Elysium that contained predominately high-Ca pyroxene with olivine and/or glass. Within the 103 areas of exposed Amazonian volcanic materials, one location was identified that has a direct link to this study. A scarp associated with crater 03-000082 was classified in the high-Ca pyroxene group described by Viviano et al. (2019). This observation has implications for the source crater project because in addition to the 1.8 ± 0.4 – 2.2 ± 0.3 Ga volcanic terrain on the western flank of Alba Mons, meteorites dominated by high-Ca pyroxene are the best potential fit for crater 03-000082 (Crown et al., 2020). High-Ca pyroxene is a common mineral in shergottites, especially in NWA 8159 and NWA 7635 which both are enriched in augite, and which have crystallization ages more consistent with the estimates for the western flank of Alba Mons (Papike et al., 2009; Herd et al., 2017). The work done by Vivian et al. (2019) opens the possibility to find spectral matches for other candidate source craters either directly on scarps such as 03-000082, or near fresh impact craters on lava flows that can be positively linked to a candidate source crater.

A limiting factor in our ability to rank the priority of candidate source craters for martian meteorites is the lack of modeled ages for craters and nearby surfaces on Mars. Improvements in crater-count chronometry have provided model ages for some martian craters and surfaces (Hartmann, 1966; Hartmann, 2005; Hartmann et al., 2010). However, the process of manually counting craters to determine the crater size distribution is cumbersome when dating multiple surfaces. The spatial resolution of orbital instruments has vastly increased from Mariner 4 at ~3 km/pixel in the 1960s to High Resolution Imaging Science Experiment (HiRISE) at ~30 cm/pixel beginning in 2006. Higher spatial resolutions allow for the identification of smaller craters and thus more tightly refined crater size distribution. This refinement comes at a trade-off of more time being required to identify small impact craters accurately and completely. The current most complete database of martian craters only contains those that are ≥1 km diameter, so those craters that are smaller must still be hand-counted when applying crater-count chronometry (Robbins and Hynek, 2012). Benedix et al. (2020) simplify the process by developing an automated Crater Detection Algorithm to increase the efficiency of the crater-count chronometry process. Supervised machine learning was used to train and subsequently validate the Crater Detection Algorithm on previously created martian crater databases (Benedix et al., 2020).

Preliminary results indicate accurate and consistent reproduction of manual databases and suggest that the Crater Detection Algorithm is equal to or better than manual detection of craters in both Context Camera (CTX) and (THEMIS Day IR) imagery. Once this new technology has been expanded to include higher resolution imagery such as HiRISE, it will be an effective tool to quickly and accurately model the ages of craters and surfaces on Mars. This tool is especially useful in studies such as this one where dating multiple craters and surfaces is outside the scope of the study. Indeed, the Crater Detection Algorithm could potentially be applied to the 52 candidate source craters and their adjacent surfaces identified by the initial queries discussed in Chapter 3.

Other variables not discussed in this study may also come into play for the evaluation of candidate source craters for martian meteorites at a future time. An example of this are the low-temperature alteration materials found in the shock-melt pockets of Tissint (Kuchka et al., 2017). The altered material formed as the martian atmosphere penetrated cracks in Tissint as it resided on Mars in low enough abundances to affect $H_2O$ and Cl concentrations, and isotopic compositions while not affecting the concentrations of major, minor, and trace elements (Kuchka et al., 2017). This low-temperature alteration may have implications for the accurate identification of source regions of martian meteorites. Indeed, as more variables for constraining candidate source craters are revealed and their implications understood, constraints for specific meteorites will become tighter and the number of potential source craters will continue to be refined.

## 4.2 Summary and concluding remarks

In this study, I have laid the foundation to link martian meteorites to their source craters. Chapter 1 outlined the necessary background for this study including current scientific goals for Mars exploration. I also discussed the limitations that we face when investigating these goals due to restricted access to Mars and our reliance on *in situ* analysis of the surface by martian landers and rovers, and by orbital instruments that must contend with atmospheric and wind-blown dust interference. Until martian meteorites are linked to a specific region on Mars, their scientific value is limited. By linking martian meteorites to their source craters, we can greatly increase their scientific value in many endeavours such as the refinement of chronology boundaries. In Chapter 2, I investigated the shock effects recorded in 13 previously understudied shergottites to better understand the conditions of their shock history and timing. This work provides crucial information for modeling the impacts of these meteorites and expanding the suite of martian meteorites from which we can constrain their source craters. Chapter 3 proposed an updated methodology to constrain candidate source craters based on work by Tornabene et al. (2006) and Mouginis-Mark et al. (1992). Using the more comprehensive understanding of the impact process, higher resolution datasets, and an emphasis on characteristics for identifying well-preserved impact craters on Amazonian-aged lava flows I was able to identify 17 candidate source craters for Zagami, Tissint, Chassigny, and NWA 8159. I selected the 8 most well-preserved craters from this set for further evaluation and then conducted detailed mapping with the use of Geographic Information Systems (GIS) to make observations on the crater morphologies and surrounding geological features. This mapping resulted in further prioritization of the 8 candidate source craters. I then discussed variables that relate to constraining source craters for individual meteorites and the implications of our prioritization. In this chapter, I briefly outlined previously identified candidate source craters that did not make the list of 8 craters evaluated in this study. Their exclusion from this study does not exclude them as potential sources for martian meteorites. Additionally, I discussed some recent research that could be applied to the candidate crater identification methodology in the future to further constrain candidate source craters and bring us closer to finding an exact link between a specific martian crater and its matching martian meteorite(s). The work accomplished in this Master's thesis is an invaluable addition to creating these links between martian meteorites and their sources, and to the understanding of Mars once this has been achieved.

# References

Agee, C. B., Wilson, N. V., McCubbin, F. M., Ziegler, K., Polyak, V. J., Sharp, Z. D., Asmerom, Y., Nunn, M. H., Shaheen, R., Thiemens, M. H., Steele, A., Fogel, M. L., Bowden, R., Glamoclija, M., Zhang, Z., & Elardo, S. M. (2013). Unique Meteorite from Early Amazonian Mars: Water-Rich Basaltic Breccia Northwest Africa 7034. *Science*, *339*(6121), 780–785. https://doi.org/10.1126/science.1228858

Amsden, A. A., Ruppel, H. M., & Hirt, C. W. (1980). SALE: a simplified ALE computer program for fluid flow at all speeds. United States. https://doi.org/10.2172/5176006

Aoudjehane, H. C., Avice, G., Barrat, J.-A., Boudouma, O., Chen, G., Duke, M. J. M., Franchi, I. A., Gattacceca, J., Grady, M. M., Greenwood, R. C., Herd, C. D. K., Hewins, R., Jambon, A., Marty, B., Rochette, P., Smith, C. L., Sautter, V., Verchovsky, A., Weber, P., & Zanda, B. (2012). Tissint Martian Meteorite: A Fresh Look at the Interior, Surface, and Atmosphere of Mars. *Science*, *338*(6108), 785–788. https://doi.org/10.1126/science.1224514

Artemieva, N., & Ivanov, B. (2004). Launch of martian meteorites in oblique impacts. *Icarus*, *171*(1), 84–101. https://doi.org/10.1016/j.icarus.2004.05.003

Banerdt, W. B., Smrekar, S. E., Banfield, D., Giardini, D., Golombek, M., Johnson, C. L., Lognonné, P., Spiga, A., Spohn, T., Perrin, C., Stähler, S. C., Antonangeli, D., Asmar, S., Beghein, C., Bowles, N., Bozdag, E., Chi, P., Christensen, U., Clinton, J., … Wieczorek, M. (2020). Initial results from the InSight mission on Mars. *Nature Geoscience*, *13*(3), 183–189. https://doi.org/10.1038/s41561-020-0544-y

Beaty, D. W., Grady, M. M., McSween, H. Y., Sefton-Nash, E., Carrier, B. L., Altieri, F., Amelin, Y., Ammannito, E., Anand, M., Benning, L. G., Bishop, J. L., Borg, L. E., Boucher, D., Brucato, J. R., Busemann, H., Campbell, K. A., Czaja, A. D., Debaille, V., Des Marais, D. J., … Zorzano, M. P. (2019). The potential science and engineering value of samples delivered to Earth by Mars sample return: International MSR Objectives and Samples Team (iMOST). *Meteoritics & Planetary Science*, *54*, S3–S152. https://doi.org/10.1111/maps.13242

Beck, P., Gillet, Ph., El Goresy, A., & Mostefaoui, S. (2005). Timescales of shock processes in chondritic and martian meteorites. *Nature*, *435*(7045), 1071–1074. https://doi.org/10.1038/nature03616

Bellucci, J. J., Nemchin, A. A., Whitehouse, M. J., Snape, J. F., Kielman, R. B., Bland, P. A., & Benedix, G. K. (2016). A Pb isotopic resolution to the Martian meteorite age paradox. *Earth and Planetary Science Letters*, *433*, 241–248. https://doi.org/10.1016/j.epsl.2015.11.004

Bellucci, J. J., Nemchin, A. A., Whitehouse, M. J., Snape, J. F., Bland, P., Benedix, G. K., & Roszjar, J. (2018). Pb evolution in the Martian mantle. *Earth and Planetary Science Letters*, *485*, 79–87. https://doi.org/10.1016/j.epsl.2017.12.039

Benedix, G. K., Lagain, A., Chai, K., Meka, S., Anderson, S., Norman, C., Bland, P. A., Paxman, J., Towner, M. C., & Tan, T. (2020). Deriving Surface Ages on Mars Using Automated Crater Counting. *Earth and Space Science*, *7*(3). https://doi.org/10.1029/2019EA001005

Bjork, R., Kreyenhagen, K., & Wagner, M. (1967). Analytical study of impact effects as applied to the meteoroid hazard. National Aeronautics and Space Administration, Issue 757.

Bläß, U. W. (2013). Shock-induced formation mechanism of seifertite in shergottites. *Physics and Chemistry of Minerals*, *40*(5), 425–437. https://doi.org/10.1007/s00269-013-0580-x

Bläß, U. W., Langenhorst, F., & McCammon, C. (2010). Microstructural investigations on strongly stained olivines of the chassignite NWA 2737 and implications for its shock history. *Earth and Planetary Science Letters*, *300*(3-4), 255–263. https://doi.org/10.1016/j.epsl.2010.09.047

Borg, L. E., Edmunson, J. E., & Asmerom, Y. (2005). Constraints on the U-Pb isotopic systematics of Mars inferred from a combined U-Pb, Rb-Sr, and Sm-Nd isotopic study of the Martian meteorite Zagami. *Geochimica et Cosmochimica Acta*, *69*(24), 5819–5830. https://doi.org/10.1016/j.gca.2005.08.007

Bouley, S., Baratoux, D., Matsuyama, I., Forget, F., Séjourné, A., Turbet, M., & Costard, F. (2016). Late Tharsis formation and implications for early Mars. *Nature*, *531*(7594), 344–347. https://doi.org/10.1038/nature17171

Bowling, T. J., Johnson, B. C., Wiggins, S. E., Walton, E. L., Melosh, H. J., & Sharp, T. G. (2020). Dwell time at high pressure of meteorites during impact ejection from Mars. *Icarus*, *343*, 113689. https://doi.org/10.1016/j.icarus.2020.113689

Brennecka, G. A., Borg, L. E., & Wadhwa, M. (2014). Insights into the Martian mantle: The age and isotopics of the meteorite fall Tissint. *Meteoritics & Planetary Science*, *49*(3), 412–418. https://doi.org/10.1111/maps.12258

Brezina, A. (1904). The arrangement of collections of meteorites. *Proceedings of the American Philosophical Society*, *43*(176), 211–247.

Carr, M. H. (2008). *The Surface of Mars*. Cambridge University Press.

Carr, M. H., & Head, J. W. (2010). Geologic history of Mars. *Earth and Planetary Science Letters*, *294*(3–4), 185–203. https://doi.org/10.1016/j.epsl.2009.06.042

Cattermole, P. (1987). Sequence, rheological properties, and effusion rates of volcanic flows at Alba Patera, Mars. *Journal of Geophysical Research: Solid Earth*, *92*(B4), E553–E560. https://doi.org/10.1029/JB092iB04p0E553

Caudill, C., Tornabene, L., McEwen, A. S., Byrne, S., Ojha, L., & Mattson, S. (2012). Layered MegaBlocks in the central uplifts of impact craters. *Icarus*, *221*(2), 710–720.

Chen, M., Sharp, T. G., El Goresy, A., Wopenka, B., & Xie, X. (1996). The Majorite-Pyrope + Magnesiowustite Assemblage: Constraints on the History of Shock Veins in Chondrites. *Science*, *271*(5255), 1570–1573. https://doi.org/10.1126/science.271.5255.1570

Chen, Ming, & El Goresy, A. (2000). The nature of maskelynite in shocked meteorites: Not diaplectic glass but a glass quenched from shock-induced dense melt at high pressures. *Earth and Planetary Science Letters*, *179*(3–4), 489–502. https://doi.org/10.1016/S0012-821X(00)00130-8

Christen, F., Eugster, O., & Busemann, H. (2005). Mars ejection times and neutron capture effects of the nakhlites Y000593 and Y000749, the olivine-phyric shergottite Y980459, and the lherzolite NWA1950. *Antarctic Meteorite Research*, *18*, 117.

Christensen, P. R., Bandfield, J. L., Hamilton, V. E., Ruff, S. W., Kieffer, H. H., Titus, T. N., Malin, M. C., Morris, R. V., Lane, M. D., Clark, R. L., Jakosky, B. M., Mellon, M. T., Pearl, J. C., Conrath, B. J., Smith, M. D., Clancy, R. T., Kuzmin, R. O., Roush, T., Mehall, G. L., … Greenfield, M. (2001). Mars Global Surveyor Thermal Emission Spectrometer experiment: Investigation description and surface science results. *Journal of Geophysical Research: Planets*, *106*(E10), 23823–23871. https://doi.org/10.1029/2000JE001370

Christensen, P. R., Engle, E., Anwar, S., Dickenshied, S., Noss, D., Gorelick, N., & Weiss-Malik, M. (2009, December). JMARS-a planetary GIS. In *AGU Fall Meeting Abstracts* (Vol. 2009, pp. IN22A-06).

Chuang, F. C., Crown, D. A., & Tornabene, L. L. (2016). Zumba crater, Daedalia Planum, Mars: Geologic investigation of a young, rayed impact crater and its secondary field. *Icarus*, *269*, 75–90. https://doi.org/10.1016/j.icarus.2016.01.005

Cohen, B. E., Mark, D. F., Cassata, W. S., Lee, M. R., Tomkinson, T., & Smith, C. L. (2017). Taking the pulse of Mars via dating of a plume-fed volcano. *Nature Communications*, *8*(1), 640. https://doi.org/10.1038/s41467-017-00513-8

Coles, K. S., Tanaka, K. L., & Christensen, P. R. (2019). *The Atlas of Mars: Mapping its Geography and Geology* (1st ed.). Cambridge University Press. https://doi.org/10.1017/9781139567428

Crown, D. A., Berman, D. C., Platz, T., & Scheidt, S. P. (2017). Geologic Mapping of Alba Mons, Mars: Constraints on Summit Evolution and Eruptive History. *48th Lunar and Planetary Science Conference*, Abstract #2301. http://www.lpi.usra.edu/meetings/lpsc2017/pdf/2301.pdf

Crown, D. A., Berman, D. C., Scheidt, S. P., & Hauber, E. (2019A). Geology of Alba Mons, Mars: Results from 1:1M-Scale Geologic Mapping. *50th Lunar and Planetary Science Conference*, Abstract #2160. https://www.hou.usra.edu/meetings/lpsc2019/pdf/2160.pdf

Crown, D. A., Berman, D. C., Scheidt, S. P., & Hauber, E. (2020). Alba Mons, Mars: Geologic Mapping of the Summit Region and Western Flank. *51st Lunar and Planetary Science Conference*, Abstract #1626. https://www.hou.usra.edu/meetings/lpsc2020/pdf/1626.pdf

Crown, D. A., Scheidt, S. P., & Berman, D. C. (2019B). Distribution and Morphology of Lava Tube Systems on the Western Flank of Alba Mons, Mars. *50th Lunar and Planetary Science Conference*, Abstract #1417. https://www.hou.usra.edu/meetings/lpsc2019/pdf/1417.pdf

Daly, L., Piazolo, S., Lee, M. R., Griffin, S., Chung, P., Campanale, F., Cohen, B. E., Hallis, L. J., Trimby, P. W., Baumgartner, R., Forman, L. V., & Benedix, G. K. (2019). Understanding the emplacement of Martian volcanic rocks using petrofabrics of the nakhlite meteorites. *Earth and Planetary Science Letters*, *520*, 220–230. https://doi.org/10.1016/j.epsl.2019.05.050

Dera, P., Prewitt, C. T., Boctor, N. Z., & Hemley, R. J. (2002). Characterization of a high-pressure phase of silica from the Martian meteorite Shergotty. *American Mineralogist*, *87*(7), 1018–1023. https://doi.org/10.2138/am-2002-0728

Dymshits, A., Sharygin, I., Litasov, K., Shatskiy, A., Gavryushkin, P., Ohtani, E., Suzuki, A., & Funakoshi, K. (2015). In situ observation of the pyroxene-majorite transition in Na2MgSi5O12 using synchrotron radiation and Raman spectroscopy of Na-majorite. *American Mineralogist*, *100*(2–3), 378–384. https://doi.org/10.2138/am-2015-4801

Edwards, C. S., & Piqueux, S. (2016). The water content of recurring slope lineae on Mars. *Geophysical Research Letters*, *43*(17), 8912–8919. https://doi.org/10.1002/2016GL070179

El Goresy, A. D., Sharp, T. G., Prewitt, C. T., Chen, M., Dubrovinsky, L., Wopenka, B., Boctor, N. Z., & Hemley, R. J. (2008). Seifertite, a dense orthorhombic polymorph of silica from the Martian meteorites Shergotty and Zagami. *European Journal of Mineralogy*, *20*(4), 523–528. https://doi.org/10.1127/0935-1221/2008/0020-1812

El Goresy, A., Dubrovinsky, L., Sharp, T. G., & Chen, M. (2004). Stishovite and post-stishovite polymorphs of silica in the shergotty meteorite: Their nature, petrographic settings versus theoretical predictions and relevance to Earth's mantle. *Journal of Physics and Chemistry of Solids*, *65*(8–9), 1597–1608. https://doi.org/10.1016/j.jpcs.2004.02.001

El Goresy, A., Gillet, Ph., Miyahara, M., Ohtani, E., Ozawa, S., Beck, P., & Montagnac, G. (2013). Shock-induced deformation of Shergottites: Shock-pressures and perturbations of magmatic ages on Mars. *Geochimica et Cosmochimica Acta*, *101*, 233–262. https://doi.org/10.1016/j.gca.2012.10.002

Eugster, O., Busemann, H., Lorenzetti, S., & Terribilini, D. (2002). Ejection ages from krypton-81-krypton-83 dating and pre-atmospheric sizes of martian meteorites. *Meteoritics & Planetary Science*, *37*(10), 1345–1360. https://doi.org/10.1111/j.1945-5100.2002.tb01033.x

Fastook, J. L., & Head, J. W. (2014). Amazonian mid- to high-latitude glaciation on Mars: Supply-limited ice sources, ice accumulation patterns, and concentric crater fill glacial flow and ice sequestration. *Planetary and Space Science*, *91*, 60–76. https://doi.org/10.1016/j.pss.2013.12.002

Filiberto, J. (2008). Experimental constraints on the parental liquid of the Chassigny meteorite: A possible link between the Chassigny meteorite and a Martian Gusev basalt. *Geochimica et Cosmochimica Acta*, *72*(2), 690–701. https://doi.org/10.1016/j.gca.2007.11.007

Floran, R. J., Prinz, M., Hlava, P. F., Keil, K., Nehru, C. E., & Hinthorne, J. R. (1978). The Chassigny meteorite: A cumulate dunite with hydrous amphibole-bearing melt inclusions. *Geochimica et Cosmochimica Acta*, *42*(8), 1213–1229. https://doi.org/10.1016/0016-7037(78)90115-1

Forget, F., Haberle, R., Montmessin, F., Levrard, B., & Head, J. (2006). Formation of glaciers on Mars by atmospheric precipitation at high obliquity. *Science*, *311*(5759), 368-371.

Freeman, J. J., Wang, A., Kuebler, K. E., Jolliff, B. L., & Haskin, L. A. (2008). Characterization of natural feldspars by raman spectroscopy for future planetary exploration. *The Canadian Mineralogist*, *46*(6), 1477-1500. https://doi.org/10.3749/canmin.46.6.1477

Frey, H. V. (2006). Impact constraints on, and a chronology for, major events in early Mars history. *Journal of Geophysical Research*, *111*(E8), E08S91. https://doi.org/10.1029/2005JE002449

Fritz, J, Greshake, A., & Stoffler, D. (2007). The Martian meteorite paradox: Climatic influence on impact ejection from Mars? *Earth and Planetary Science Letters*, *256*(1–2), 55-60. https://doi.org/10.1016/j.epsl.2007.01.009

Fritz, J., Assis Fernandes, V., Greshake, A., Holzwarth, A., & Böttger, U. (2019). On the formation of diaplectic glass: Shock and thermal experiments with plagioclase of different chemical compositions. *Meteoritics & Planetary Science*, *54*(7), 1533–1547. https://doi.org/10.1111/maps.13289

Fritz, J., Greshake, A., & Fernandes, V. A. (2017). Revising the shock classification of meteorites. *Meteoritics & Planetary Science*, *52*(6), 1216–1232. https://doi.org/10.1111/maps.12845

Fritz, Jörg, & Greshake, A. (2009). High-pressure phases in an ultramafic rock from Mars. *Earth and Planetary Science Letters*, *288*(3–4), 619–623. https://doi.org/10.1016/j.epsl.2009.10.030

Fritz, Jörg, Artemieva, N., & Greshake, A. (2005). Ejection of Martian meteorites. *Meteoritics & Planetary Science*, *40*(9–10), 1393–1411. https://doi.org/10.1111/j.1945-5100.2005.tb00409.x

Gillet, P., El Goresy, A., Beck, P., & Chen, M. (2007). High-pressure mineral assemblages in shocked meteorites and shocked terrestrial rocks: Mechanisms of phase transformations and constraints to pressure and temperature histories. *Special Papers-Geological Society of America*, *421*, 57.

Glotch, T. D., Edwards, C. S., Yesiltas, M., Shirley, K. A., McDougall, D. S., Kling, A. M., Bandfield, J. L., & Herd, C. D. K. (2018). MGS-TES Spectra Suggest a Basaltic Component in the Regolith of Phobos. *Journal of Geophysical Research: Planets*, *123*(10), 2467–2484. https://doi.org/10.1029/2018JE005647

Golombek, M., Bloom, C., Wigton, N., & Warner, N. (2014). Constraints on the Age of Corinto Crater from Mapping Secondaries in Elysium Planitia on Mars. *45th Lunar and Planetary Science Conference*, Abstract #1470. http://www.lpi.usra.edu/meetings/lpsc2014/pdf/1470.pdf

Gorelick, N. S., Weiss-Malik, M., Steinberg, B., & Anwar, S. (2003). JMARS: A Multimission Data Fusion Application. *34th Lunar and Planetary Science Conference*, Abstract #2057. http://www.lpi.usra.edu/meetings/lpsc2003/pdf/2057.pdf

Greshake, A., Fritz, J., Böttger, U., & Goran, D. (2013). Shear-induced ringwoodite formation in the Martian shergottite Dar al Gani 670. *Earth and Planetary Science Letters*, *375*, 383–394. https://doi.org/10.1016/j.epsl.2013.06.002

Greshake, A., Stephan, T., & Rost, D. (1998). Symplectic Exsolutions in Olivine from the Martian Meteorite Chassigny: Evidence for Slow Cooling Under Highly Oxidizing Conditions. *29th Lunar and Planetary Science Conference*, Abstract #1069. http://www.lpi.usra.edu/meetings/LPSC98/pdf/1069.pdf

Hahn, B., & McLennan, S. (2007). *Evolution and geochemistry of the Martian crust: Integrating mission datasets*. Seventh International Conference on Mars, *1353*, 3179. https://ui.adsabs.harvard.edu/abs/2007LPICo1353.3179H

Hartmann, W. K. (1966). Martian cratering. *Icarus*, *5*(1–6), 565–576.

Hartmann, W. K. (1999). Martian cratering VI: Crater count isochrons and evidence for recent volcanism from Mars Global Surveyor. *Meteoritics & Planetary Science*, *34*(2), 167–177. https://doi.org/10.1111/j.1945-5100.1999.tb01743.x

Hartmann, W. K. (2005). Martian cratering 8: Isochron refinement and the chronology of Mars. *Icarus*, *174*(2), 294–320. https://doi.org/10.1016/j.icarus.2004.11.023

Hartmann, W. K., & Berman, D. C. (2000). Elysium Planitia lava flows: Crater count chronology and geological implications. *Journal of Geophysical Research: Planets*, *105*(E6), 15011–15025. https://doi.org/10.1029/1999JE001189

Hartmann, W. K., Quantin, C., Werner, S. C., & Popova, O. (2010). Do young martian ray craters have ages consistent with the crater count system? *Icarus*, *208*(2), 621–635. https://doi.org/10.1016/j.icarus.2010.03.030

Head, J. N., Melosh, H. J., & Ivanov, B. A. (2002). Martian meteorite launch: High-speed ejecta from small craters. *Science*, *298*(5599), 1752–1756.

Head, J. W., & Marchant, D. R. (2003). Cold-based mountain glaciers on Mars: Western Arsia Mons. *Geology*, *31*(7), 641–644.

Herd, C. D. K., Tornabene, L. L., Bowling, T. J., Walton, E. L., Sharp, T. G., Melosh, H. J., Hamilton, J. S., Viviano, C. E., & Ehlmann, B. L. (2018). Linking Martian Meteorites to their Source Craters: New Insights. *49th Lunar and Planetary Science Conference*, Abstract #2266. http://www.lpi.usra.edu/meetings/lpsc2018/pdf/2266.pdf

Herd, Christopher D.K., Walton, E. L., Agee, C. B., Muttik, N., Ziegler, K., Shearer, C. K., Bell, A. S., Santos, A. R., Burger, P. V., Simon, J. I., Tappa, M. J., McCubbin, F. M., Gattacceca, J., Lagroix, F., Sanborn, M. E., Yin, Q.-Z., Cassata, W. S., Borg, L. E., Lindvall, R. E., … Caffee, M. W. (2017). The Northwest Africa 8159 martian meteorite: Expanding the martian sample suite to the early Amazonian. *Geochimica et Cosmochimica Acta*, *218*, 1–26. https://doi.org/10.1016/j.gca.2017.08.037

Herzberg, C., & Zhang, J. (1996). Melting experiments on anhydrous peridotite KLB-1: Compositions of magmas in the upper mantle and transition zone. *Journal of Geophysical Research: Solid Earth*, *101*(B4), 8271–8295.

Herzog, G. F., & Caffee, M. W. (2014). Cosmic-Ray Exposure Ages of Meteorites. In *Treatise on Geochemistry* (pp. 419–454). Elsevier. https://doi.org/10.1016/B978-0-08-095975-7.00110-8

Hörz, F., & Quaide, W. L. (1973). Debye-Scherrer investigations of experimentally shocked silicates. *The Moon*, *6*(1–2), 45–82.

Hundal, C. B., Golombek, M. P., & Daubar, I. J. (2017). Chronology of Fresh Rayed Craters in Elysium Planitia, Mars. *48th Lunar and Planetary Science Conference*, Abstract #1726. http://www.lpi.usra.edu/meetings/lpsc2017/pdf/1726.pdf

Irving, A. J., Kuehner, S. M., Herd, C. D. K., Gellissen, M., Korotev, R. L., Puchtel, I., Walker, R. J., Lapen, T., & Rumble, D. I. (2010). *Petrologic, Elemental and Multi-Isotopic Characterization of Permafic Olivine-Phyric Shergottite Northwest Africa 5789: A Primitive Magma Derived from Depleted Martian Mantle. 41st Lunar and Planetary Science Conference*, Abstract #1547. http://www.lpi.usra.edu/meetings/lpsc2010/pdf/1547.pdf

Irving, T. (2020). An up-to-date List of Martian Meteorites. Retrieved December 15, 2020, from https://imca.cc/mars/martian-meteorites-list.htm

Jaret, S. J., Woerner, W. R., Phillips, B. L., Ehm, L., Nekvasil, H., Wright, S. P., & Glotch, T. D. (2015). Maskelynite formation via solid-state transformation: Evidence of infrared and X-ray anisotropy. *Journal of Geophysical Research: Planets*, *120*(3), 570–587. https://doi.org/10.1002/2014JE004764

Johnson, M. C., Rutherford, M. J., & Hess, P. C. (1991). Chassigny petrogenesis: Melt compositions, intensive parameters and water contents of Martian (?) magmas. *Geochimica et Cosmochimica Acta*, *55*(1), 349–366. https://doi.org/10.1016/0016-7037(91)90423-3

Kadish, S. J., Head, J. W., Fastook, J. L., & Marchant, D. R. (2014). Middle to Late Amazonian tropical mountain glaciers on Mars: The ages of the Tharsis Montes fan-shaped deposits. *Planetary and Space Science*, *91*, 52–59. https://doi.org/10.1016/j.pss.2013.12.005

Kadish, S., Head, J., Parsons, R., & Marchant, D. (2008). The Ascraeus Mons fan-shaped deposit: Volcano–ice interactions and the climatic implications of cold-based tropical mountain glaciation. *Icarus*, *197*(1), 84–109. https://doi.org/10.1016/j.icarus.2008.03.019

Kereszturi, A., & Chatzitheodoridis, E. (2016). Searching for the Source Crater of Nakhlite Meteorites. *Origins of Life and Evolution of Biospheres*, *46*(4), 455–471. https://doi.org/10.1007/s11084-016-9498-x

Kimura, M., Chen, M., Yoshida, Y., El Goresy, A., & Ohtani, E. (2004). Back-transformation of high-pressure phases in a shock melt vein of an H-chondrite during atmospheric passage: Implications for the survival of high-pressure phases after decompression. *Earth and Planetary Science Letters*, *217*(1–2), 141–150. https://doi.org/10.1016/S0012-821X(03)00585-5

Kollé, J. J., & Blacic, J. D. (1982). Deformation of single-crystal clinopyroxenes: 1. Mechanical twinning in diopside and hedenbergite. *Journal of Geophysical Research*, *87*(B5), 4019. https://doi.org/10.1029/JB087iB05p04019

Korochantseva, E. V., Schwenzer, S. P., Buikin, A. I., Hopp, J., Ott, U., & Trieloff, M. (2011). 40Ar-39Ar and cosmic-ray exposure ages of nakhlites-Nakhla, Lafayette, Governador Valadares-and Chassigny: 40Ar-39Ar and exposure ages of nakhlites and Chassigny. *Meteoritics & Planetary Science*, *46*(9), 1397–1417. https://doi.org/10.1111/j.1945-5100.2011.01240.x

Kostama, V.-P., Kreslavsky, M. A., & Head, J. W. (2006). Recent high-latitude icy mantle in the northern plains of Mars: Characteristics and ages of emplacement. *Geophysical Research Letters*, *33*(11), L11201. https://doi.org/10.1029/2006GL025946

Krot, A. N., Keil, K., Scott, E. R. D., Goodrich, C. A., & Weisberg, M. K. (2014). Classification of Meteorites and Their Genetic Relationships. In *Treatise on Geochemistry* (pp. 1–63). Elsevier. https://doi.org/10.1016/B978-0-08-095975-7.00102-9

Kubo, T., Kato, T., Higo, Y., & Funakoshi, K. (2015). Curious kinetic behavior in silica polymorphs solves seifertite puzzle in shocked meteorite. *Science Advances*, *1*(4), e1500075. https://doi.org/10.1126/sciadv.1500075

Kurosawa, K., Okamoto, T., & Genda, H. (2018). Hydrocode modeling of the spallation process during hypervelocity impacts: Implications for the ejection of Martian meteorites. *Icarus*, *301*, 219–234. https://doi.org/10.1016/j.icarus.2017.09.015

Lafuente B., Downs R. T., Yang H., Stone N. (2015). The power of databases: the RRUFF project. In: *Highlights in Mineralogical Crystallography*, T. Armbruster and R. M. Danisi, eds. Berlin, Germany, W. De Gruyter, pp 1-30

Lagain, A., Bouley, S., Baratoux, D., Costard, F., & Wieczorek, M. (2020). Impact cratering rate consistency test from ages of layered ejecta on Mars. *Planetary and Space Science*, *180*, 104755. https://doi.org/10.1016/j.pss.2019.104755

Lapen, T. J., Righter, M., Andreasen, R., Irving, A. J., Satkoski, A. M., Beard, B. L., Nishiizumi, K., Jull, A. J. T., & Caffee, M. W. (2017). Two billion years of magmatism recorded from a single Mars meteorite ejection site. *Science Advances*, *3*(2), e1600922. https://doi.org/10.1126/sciadv.1600922

Lapen, T. J., Righter, M., Brandon, A. D., Debaille, V., Beard, B. L., Shafer, J. T., & Peslier, A. H. (2010). A Younger Age for ALH84001 and Its Geochemical Link to Shergottite Sources in Mars. *Science*, *328*(5976), 347–351. https://doi.org/10.1126/science.1185395

Lauro, S. E., Pettinelli, E., Caprarelli, G., Guallini, L., Rossi, A. P., Mattei, E., Cosciotti, B., Cicchetti, A., Soldovieri, F., Cartacci, M., Di Paolo, F., Noschese, R., & Orosei, R. (2020). Multiple subglacial water bodies below the south pole of Mars unveiled by new MARSIS data. *Nature Astronomy*. https://doi.org/10.1038/s41550-020-1200-6

Leya, I., & Masarik, J. (2009). Cosmogenic nuclides in stony meteorites revisited. *Meteoritics & Planetary Science*, *44*(7), 1061–1086. https://doi.org/10.1111/j.1945-5100.2009.tb00788.x

Leya, I., Lange, H.-J., Neumann, S., Wieler, R., & Michel, R. (2000). The production of cosmogenic nuclides in stony meteoroids by galactic cosmic-ray particles. *Meteoritics & Planetary Science*, *35*(2), 259–286. https://doi.org/10.1111/j.1945-5100.2000.tb01775.x

Ma, C., Tschauner, O., Beckett, J. R., Liu, Y., Rossman, G. R., Sinogeikin, S. V., Smith, J. S., & Taylor, L. A. (2016). Ahrensite, γ-Fe2SiO4, a new shock-metamorphic mineral from the Tissint meteorite: Implications for the Tissint shock event on Mars. *Geochimica et Cosmochimica Acta*, *184*, 240–256. https://doi.org/10.1016/j.gca.2016.04.042

Ma, C., Tschauner, O., Beckett, J. R., Liu, Y., Rossman, G. R., Zhuravlev, K., Prakapenka, V., Dera, P., & Taylor, L. A. (2015). Tissintite, (Ca, Na, □)AlSi2O6, a highly-defective, shock-induced, high-pressure clinopyroxene in the Tissint martian meteorite. *Earth and Planetary Science Letters*, *422*, 194–205. https://doi.org/10.1016/j.epsl.2015.03.057

Madeleine, J.-B., Forget, F., Head, J. W., Levrard, B., Montmessin, F., & Millour, E. (2009). Amazonian northern mid-latitude glaciation on Mars: A proposed climate scenario. *Icarus*, *203*(2), 390–405. https://doi.org/10.1016/j.icarus.2009.04.037

Mars Exploration Program. (2018, May 29). *A New Impact Crater*. https://mars.nasa.gov/resources/21891/a-new-impact-crater/

Marty, B., Heber, V. S., Grimberg, A., Wieler, R., & Barrat, J.-A. (2006). Noble gases in the Martian meteorite Northwest Africa 2737: A new chassignite signature. *Meteoritics & Planetary Science*, *41*(5), 739–748. https://doi.org/10.1111/j.1945-5100.2006.tb00989.x

Mason, B., Nelon, J. A., Muir, P., & Taylor, S. R. (1976). The Composition of the Chassigny Meteorite. *Meteoritics*, *11*(1), 21–27. https://doi.org/10.1111/j.1945-5100.1976.tb00311.x

McCoy, T. J., Wadhwa, M., & Keil, K. (1999). New lithologies in the Zagami meteorite: Evidence for fractional crystallization of a single magma unit on Mars. *Geochimica et Cosmochimica Acta*, *63*(7–8), 1249–1262. https://doi.org/10.1016/S0016-7037(99)00015-0

McCubbin, F. M., Elardo, S. M., Shearer, C. K., Smirnov, A., Hauri, E. H., & Draper, D. S. (2013). A petrogenetic model for the comagmatic origin of chassignites and nakhlites: Inferences from chlorine-rich minerals, petrology, and geochemistry. *Meteoritics & Planetary Science*, *48*(5), 819–853. https://doi.org/10.1111/maps.12095

McEwen, A. S., Eliason, E. M., Bergstrom, J. W., Bridges, N. T., Hansen, C. J., Delamere, W. A., Grant, J. A., Gulick, V. C., Herkenhoff, K. E., & Keszthelyi, L. (2007). Mars reconnaissance orbiter's high resolution imaging science experiment (HiRISE). *Journal of Geophysical Research: Planets*, *112*(E5).

McEwen, A., Preblich, B., Turtle, E., Artemieva, N., Golombek, M., Hurst, M., Kirk, R., Burr, D., & Christensen, P. (2005). The rayed crater Zunil and interpretations of small impact craters on Mars. *Icarus*, *176*(2), 351–381. https://doi.org/10.1016/j.icarus.2005.02.009

McGovern, P. J., Solomon, S. C., Head, J. W., Smith, D. E., Zuber, M. T., & Neumann, G. A. (2001). Extension and uplift at Alba Patera, Mars: Insights from MOLA observations and loading models. *Journal of Geophysical Research: Planets*, *106*(E10), 23769–23809. https://doi.org/10.1029/2000JE001314

McSween, H. Y. (1994). What we have learned about Mars from SNC meteorites. *Meteoritics*, *29*(6), 757–779. https://doi.org/10.1111/j.1945-5100.1994.tb01092.x

McSween, H. Y. (2015). Petrology on Mars. *American Mineralogist*, *100*(11–12), 2380–2395. https://doi.org/10.2138/am-2015-5257

McSween, H. Y., & Stolper, E. M. (1980). Basaltic Meteorites. *Scientific American*, *242*(6), 54–63. https://doi.org/10.1038/scientificamerican0680-54

McSween, H.Y., & McLennan, S. M. (2014). Mars. In *Treatise on Geochemistry* (pp. 251–300). Elsevier. https://doi.org/10.1016/B978-0-08-095975-7.00125-X

McSween, H. Y., Taylor, G. J., & Wyatt, M. B. (2009). Elemental Composition of the Martian Crust. *Science*, *324*(5928), 736–739. JSTOR.

Melosh, H. J. (1984). Impact ejection, spallation, and the origin of meteorites. *Icarus*, *59*(2), 234–260. https://doi.org/10.1016/0019-1035(84)90026-5

Melosh, H. J. (1985). Ejection of rock fragments from planetary bodies. *Geology*, *13*(2), 144. https://doi.org/10.1130/0091-7613(1985)13<144:EORFFP>2.0.CO;2

MEPAG (2020), Mars Scientific Goals, Objectives, Investigations, and Priorities: 2020. D. Banfield, ed., 89 p. white paper posted March, 2020 by the Mars Exploration Program Analysis Group (MEPAG) at https://mepag.jpl.nasa.gov/reports.cfm.

Misawa, K., Shih, C., Reese, Y., Bogard, D., & Nyquist, L. (2006). Rb-Sr, Sm-Nd and Ar-Ar isotopic systematics of Martian dunite Chassigny. *Earth and Planetary Science Letters*, *246*(1–2), 90–101. https://doi.org/10.1016/j.epsl.2006.03.044

Mittlefehldt, D. W. (1994). ALH84001, a cumulate orthopyroxenite member of the Martian meteorite clan. *Meteoritics*, *29*(2), 214–221.

Miyahara, M., Kaneko, S., Ohtani, E., Sakai, T., Nagase, T., Kayama, M., Nishido, H., & Hirao, N. (2013). Discovery of seifertite in a shocked lunar meteorite. *Nature Communications*, *4*(1), 1737. https://doi.org/10.1038/ncomms2733

Mouginis-Mark, P. J., & Boyce, J. M. (2012). Tooting crater: Geology and geomorphology of the archetype large, fresh, impact crater on Mars. *Chemie Der Erde - Geochemistry*, *72*(1), 1–23. https://doi.org/10.1016/j.chemer.2011.12.001

Mouginis-Mark, P. J., McCoy, T. J., Taylor, G. J., & Keil, K. (1992). Martian parent craters for the SNC meteorites. *Journal of Geophysical Research*, *97*(E6), 10213. https://doi.org/10.1029/92JE00612

Nekvasil, H., McCubbin, F. M., Harrington, A., Elardo, S., & Lindsley, D. H. (2009). Linking the Chassigny meteorite and the Martian surface rock Backstay: Insights into igneous crustal differentiation processes on Mars. *Meteoritics & Planetary Science*, *44*(6), 853–869. https://doi.org/10.1111/j.1945-5100.2009.tb00773.x

Nyquist, L. E., Bogard, D. D., Shih, C.-Y., Greshake, A., Stöffler, D., & Eugster, O. (2001). Ages and Geologic Histories of Martian Meteorites. *Space Science Reviews*, *96*(1), 105–164. https://doi.org/10.1023/A:1011993105172

Ody, A., Poulet, F., Quantin, C., Bibring, J.-P., Bishop, J. L., & Dyar, M. D. (2015). Candidates source regions of martian meteorites as identified by OMEGA/MEx. *Icarus*, *258*, 366–383. https://doi.org/10.1016/j.icarus.2015.05.019

Ott, U. (1988). Noble gases in SNC meteorites: Shergotty, Nakhla, Chassigny. *Geochimica et Cosmochimica Acta*, *52*(7), 1937–1948.

Papike, J. J., Karner, J. M., Shearer, C. K., & Burger, P. V. (2009). Silicate mineralogy of martian meteorites. *Geochimica et Cosmochimica Acta*, *73*(24), 7443–7485. https://doi.org/10.1016/j.gca.2009.09.008

Park, J., Okazaki, R., & Nagao, K. (2003). Noble Gas Studies on Martian Meteorites: Dar Al Gani 476/489, Sayh Al Uhaymir 005/060, Dhofar 019, Los Angeles 001 and Zagami. *34th Lunar and Planetary Science Conference*, Abstract #1213. http://www.lpi.usra.edu/meetings/lpsc2003/pdf/1213.pdf

Peslier, A., Hnatyshin, D., Herd, C., Walton, E., Brandon, A., Lapen, T., & Shafer, J. (2010). Crystallization, melt inclusion, and redox history of a Martian meteorite: Olivine-phyric shergottite Larkman Nunatak 06319. *Geochimica et Cosmochimica Acta*, *74*(15), 4543-4576.

Pittarello, L., Daly, L., PickersgilL, A. E., Ferrière, L., & Lee, M. R. (2020A). Shock metamorphism in plagioclase and selective amorphization. *Meteoritics & Planetary Science*, *55*(5), 1103–1115. https://doi.org/10.1111/maps.13494

Pittarello, L., Fritz, J., Roszjar, J., Lenz, C., Chanmuang N., C., & Koeberl, C. (2020B). Partial amorphization of experimentally shocked plagioclase: A spectroscopic study. *Meteoritics & Planetary Science*, *55*(3), 669–678. https://doi.org/10.1111/maps.13445

Pozuelo, M., Lefebvre, J., Srivastava, P., & Gupta, V. (2019). Stishovite formation at very low pressures in soda-lime glass. *Scripta Materialia*, *171*, 6–9. https://doi.org/10.1016/j.scriptamat.2019.06.005

Prinz, M., Hlava, P., & Keil, K. (1974). The Chassigny meteorite: A relatively iron-rich cumulate dunite. *Metic*, *9*, 393.

Quantin, C., Popova, O., Hartmann, W. K., & Werner, S. C. (2016). Young Martian crater Gratteri and its secondary craters. *Journal of Geophysical Research: Planets*, *121*(7), 1118–1140.

Quintana, S. N., Schultz, P. H., & Horowitz, S. S. (2018). Experimental constraints on impact-induced winds. *Icarus*, *305*, 91–104.

Robbins, S. J., & Hynek, B. M. (2012). A new global database of Mars impact craters ≥1 km: 2. Global crater properties and regional variations of the simple-to-complex transition diameter. *Journal of Geophysical Research: Planets*, *117*(E6). https://doi.org/10.1029/2011JE003967

Rubin, A. E., & Grossman, J. N. (2010). Meteorite and meteoroid: New comprehensive definitions. *Meteoritics & Planetary Science*, *45*(1), 114–122.

Rucks, M. J., Whitaker, M. L., Glotch, T. D., Parise, J. B., Jaret, S. J., Catalano, T., & Dyar, M. D. (2018). Making tissintite: Mimicking meteorites in the multi-anvil. *American Mineralogist*, *103*(9), 1516–1519. https://doi.org/10.2138/am-2018-6539

Ruff, S. W., & Christensen, P. R. (2002). Bright and dark regions on Mars: Particle size and mineralogical characteristics based on Thermal Emission Spectrometer data. *Journal of Geophysical Research: Planets*, *107*(E12), 2-1-2–22. https://doi.org/10.1029/2001JE001580

Schnabel, C., Ma, P., Herzog, G. F., Faestermann, T., Knie, K., & Korschinek, G. (2001). 10Be, 26Al, and 53Mn in Martian Meteorites. *32nd Lunar and Planetary Science Conference*, Abstract #1353. http://www.lpi.usra.edu/meetings/lpsc2001/pdf/1353.pdf

Schneeberger, D. M., & Pieri, D. C. (1991). Geomorphology and stratigraphy of Alba Patera, Mars. *Journal of Geophysical Research*, *96*(B2), 1907. https://doi.org/10.1029/90JB01662

Schultz, P. H., & Gault, D. E. (1979). Atmospheric effects on Martian ejecta emplacement. *Journal of Geophysical Research: Solid Earth*, *84*(B13), 7669–7687.

Scott, D. H., & Tanaka, K. L. (1986). Geologic map of the western equatorial region of Mars. https://doi.org/10.3133/i1802A

Sharp, T. G., Walton, E. L., Hu, J., & Agee, C. (2019). Shock conditions recorded in NWA 8159 martian augite basalt with implications for the impact cratering history on Mars. *Geochimica et Cosmochimica Acta*, *246*, 197–212. https://doi.org/10.1016/j.gca.2018.11.014

Sharp, T., & deCarli, P. (2006). Shock Effects in Meteorites. *Meteorites and the Early Solar System II*, 653-677.

Shaw, C. S., & Walton, E. (2013). Thermal modeling of shock melts in Martian meteorites: Implications for preserving Martian atmospheric signatures and crystallization of high-pressure minerals from shock melts. *Meteoritics & Planetary Science*, *48*(5), 758–770.

Shoemaker, Eugene M. (1962). Interpretation of lunar craters. *Physics and Astronomy of the Moon*, 283–359.

Shoemaker, Eugene Merle. (1959). Impact mechanics at Meteor crater, Arizona (No. 2331–1258). US Geological Survey.

Sinha, R. K., & Vijayan, S. (2017). Geomorphic investigation of craters in Alba Mons, Mars: Implications for Late Amazonian glacial activity in the region. *Planetary and Space Science*, *144*, 32–48. https://doi.org/10.1016/j.pss.2017.05.014

Stephant, A., Garvie, L. A., Mane, P., Hervig, R., & Wadhwa, M. (2018). Terrestrial exposure of a fresh Martian meteorite causes rapid changes in hydrogen isotopes and water concentrations. *Scientific Reports*, *8*(1), 1-7.

Stillman, D. E., Bue, B. D., Wagstaff, K. L., Primm, K. M., Michaels, T. I., & Grimm, R. E. (2020). Evaluation of wet and dry recurring slope lineae (RSL) formation mechanisms based on quantitative mapping of RSL in Garni Crater, Valles Marineris, Mars. *Icarus*, *335*, 113420. https://doi.org/10.1016/j.icarus.2019.113420

Stöffler, D., Hamann, C., & Metzler, K. (2018). Shock metamorphism of planetary silicate rocks and sediments: Proposal for an updated classification system. *Meteoritics & Planetary Science*, *53*(1), 5–49. https://doi.org/10.1111/maps.12912

Stöffler, D., Keil, K., & Edward R.D, S. (1991). Shock metamorphism of ordinary chondrites. *Geochimica et Cosmochimica Acta*, *55*(12), 3845–3867. https://doi.org/10.1016/0016-7037(91)90078-J

Stolper, E., & McSween, H. Y. (1979). Petrology and origin of the shergottite meteorites. *Geochimica et Cosmochimica Acta*, *43*(9), 1475–1498. https://doi.org/10.1016/0016-7037(79)90142-X

Takenouchi, A., Mikouchi, T., & Kogure, T. (2017). Mineralogical study of brown olivine in Northwest Africa 1950 shergottite and implications for the formation mechanism of iron nanoparticles. *Meteoritics & Planetary Science*, *52*(12), 2491–2504. https://doi.org/10.1111/maps.12949

Takenouchi, A., Mikouchi, T., & Yamaguchi, A. (2018). Shock veins and brown olivine in Martian meteorites: Implications for their shock pressure-temperature histories. *Meteoritics & Planetary Science*, *53*(11), 2259-2284. https://doi.org/10.1111/maps.13120

Tanaka, K. L., Robbins, S. J., Fortezzo, C. M., Skinner, J. A., & Hare, T. M. (2014). The digital global geologic map of Mars: Chronostratigraphic ages, topographic and crater morphologic characteristics, and updated resurfacing history. *Planetary and Space Science*, *95*, 11–24. https://doi.org/10.1016/j.pss.2013.03.006

Taylor, G. J. (2013). The bulk composition of Mars. *Geochemistry*, *73*(4), 401–420. https://doi.org/10.1016/j.chemer.2013.09.006

Terribilini, D., Busemann, H., & Eugster, O. (2000). Krypton-81-krypton cosmic-ray exposure ages of Martian meteorites including the new shergottite Los Angeles. *Meteoritics & Planetary Science*, *35*(5, Suppl.), 155–156.

Terribilini, Dario, Eugster, O., Burger, M., Jakob, A., & Krähenbühl, U. (1998). Noble gases and chemical composition of Shergotty mineral fractions, Chassigny, and Yamato 793605: The trapped argon-40/argon-36 ratio and ejection times of Martian meteorites. *Meteoritics & Planetary Science*, *33*(4), 677–684.

Tornabene, L. L., Moersch, J. E., McSween, H. Y., McEwen, A. S., Piatek, J. L., Milam, K. A., & Christensen, P. R. (2006). Identification of large (2–10 km) rayed craters on Mars in THEMIS thermal infrared images: Implications for possible Martian meteorite source regions. *Journal of Geophysical Research*, *111*(E10). https://doi.org/10.1029/2005JE002600

Tornabene, L. L., Osinski, G. R., McEwen, A. S., Boyce, J. M., Bray, V. J., Caudill, C. M., Grant, J. A., Hamilton, C. W., Mattson, S., & Mouginis-Mark, P. J. (2012). Widespread crater-related pitted materials on Mars: Further evidence for the role of target volatiles during the impact process. *Icarus*, *220*(2), 348–368. https://doi.org/10.1016/j.icarus.2012.05.022

Tornabene, L. L., Watters, W. A., Osinski, G. R., Boyce, J. M., Harrison, T. N., Ling, V., & McEwen, A. S. (2018). A depth versus diameter scaling relationship for the best-preserved melt-bearing complex craters on Mars. *Icarus*, *299*, 68–83. https://doi.org/10.1016/j.icarus.2017.07.003

Treiman, A. H. (2005). The nakhlite meteorites: Augite-rich igneous rocks from Mars. *Geochemistry*, *65*(3), 203–270. https://doi.org/10.1016/j.chemer.2005.01.004

Treiman, A. H., Dyar, M. D., McCanta, M., Noble, S. K., & Pieters, C. M. (2007). Martian Dunite NWA 2737: Petrographic constraints on geological history, shock events, and olivine color. *Journal of Geophysical Research*, *112*(E4), E04002. https://doi.org/10.1029/2006JE002777

Treiman, A. H., Gleason, J. D., & Bogard, D. D. (2000). The SNC meteorites are from Mars. *Planetary and Space Science*, *48*(12–14), 1213–1230. https://doi.org/10.1016/S0032-0633(00)00105-7

Trepmann, C., & Stöckhert, B. (2001). Mechanical twinning of jadeite; an indication of synseismic loading beneath the brittle-plastic transition. *Geologische Rundschau = International Journal of Earth Sciences (1999)*, *90*(1), 4–13. GeoRef. https://doi.org/10.1007/s005310000165

Udry, A., Howarth, G. H., Herd, C. D. K., Day, J. M. D., Lapen, T. J., & Filiberto, J. (2020). What Martian meteorites reveal about the interior and surface of Mars. *Journal of Geophysical Research: Planets*, 125, e2020JE006523. https://doi-org.login.ezproxy.library.ualberta.ca/10.1029/2020JE006523

Van de Moortèle, B., Reynard, B., Rochette, P., Jackson, M., Beck, P., Gillet, P., Mcmillan, P., & Mccammon, C. (2007). Shock-induced metallic iron nanoparticles in olivine-rich Martian meteorites. *Earth and Planetary Science Letters*, *262*(1–2), 37–49. https://doi.org/10.1016/j.epsl.2007.07.002

Vaucher, J., Baratoux, D., Mangold, N., Pinet, P., Kurita, K., & Grégoire, M. (2009). The volcanic history of central Elysium Planitia: Implications for martian magmatism. *Icarus*, *204*(2), 418–442.

Vickery, A. M., & Melosh, H. J. (1987). The Large Crater Origin of SNC Meteorites. *Science*, *237*(4816), 738–743.

Vickery, Ann M, & Melosh, H. (1983). The origin of SNC meteorites: An alternative to Mars. *Icarus*, *56*(2), 299–318.

Villanueva, G. L., Mumma, M. J., Novak, R. E., Kaufl, H. U., Hartogh, P., Encrenaz, T., Tokunaga, A., Khayat, A., & Smith, M. D. (2015). Strong water isotopic anomalies in the martian atmosphere: Probing current and ancient reservoirs. *Science*, *348*(6231), 218–221. https://doi.org/10.1126/science.aaa3630

Viola, D., McEwen, A. S., Dundas, C. M., & Byrne, S. (2015). Expanded secondary craters in the Arcadia Planitia region, Mars: Evidence for tens of Myr-old shallow subsurface ice. *Icarus*, *248*, 190–204. https://doi.org/10.1016/j.icarus.2014.10.032

Viviano, C. E., Murchie, S. L., Daubar, I. J., Morgan, M. F., Seelos, F. P., & Plescia, J. B. (2019). Composition of Amazonian volcanic materials in Tharsis and Elysium, Mars, from MRO/CRISM reflectance spectra. *Icarus*, *328*, 274–286. https://doi.org/10.1016/j.icarus.2019.03.001

Voigt, J. R. C., & Hamilton, C. W. (2018). Investigating the volcanic versus aqueous origin of the surficial deposits in Eastern Elysium Planitia, Mars. *Icarus*, *309*, 389–410. https://doi.org/10.1016/j.icarus.2018.03.009

von Engelhardt, W., Arndt, J., Stöffler, D., Müller, W., Jeziorkowski, H., & Gubser, R. (1967). Diaplektische Gläser in den Breccien des Ries von Nördlingen als Anzeichen für Stoßwellenmetamorphose. *Contributions to Mineralogy and Petrology*, *15*(1), 93–102.

Wadhwa, M., & Crozaz, G. (1995). Trace and minor elements in minerals of nakhlites and Chassigny: Clues to their petrogenesis. *Geochimica et Cosmochimica Acta*, *59*(17), 3629–3645. https://doi.org/10.1016/0016-7037(95)00228-R

Walton, E. L., & Shaw, C. S. (2009). Understanding the textures and origin of shock melt pockets in Martian meteorites from petrographic studies, comparisons with terrestrial mantle xenoliths, and experimental studies. *Meteoritics & Planetary Science*, *44*(1), 55–76.

Walton, E. L., Irving, A. J., Bunch, T. E., & Herd, C. D. K. (2012). Northwest Africa 4797: A strongly shocked ultramafic poikilitic shergottite related to compositionally intermediate Martian meteorites: A strongly shocked ultramafic shergottite. *Meteoritics & Planetary Science*, *47*(9), 1449–1474. https://doi.org/10.1111/j.1945-5100.2012.01407.x

Walton, E. L., Tschauner, O., Herd, C. D. K., & Agee, C. B. (2016). Shock Effects in New Martian Olivine Basalt Northwest Africa 10416: Distinct from Shergottites but Akin to Northwest Africa 8159. *47th Lunar and Planetary Science Conference*, Abstract #1639. http://www.lpi.usra.edu/meetings/lpsc2016/pdf/1639.pdf

Walton, E.L., Sharp, T. G., Hu, J., & Filiberto, J. (2014). Heterogeneous mineral assemblages in martian meteorite Tissint as a result of a recent small impact event on Mars. *Geochimica et Cosmochimica Acta*, *140*, 334–348. https://doi.org/10.1016/j.gca.2014.05.023

Walton, Erin L, & Herd, C. D. (2007). Dynamic crystallization of shock melts in Allan Hills 77005: Implications for melt pocket formation in Martian meteorites. *Geochimica et Cosmochimica Acta*, *71*(21), 5267–5285.

Walton, Erin L., & Spray, J. G. (2003). Mineralogy, microtexture, and composition of shock-induced melt pockets in thi Los Angeles basaltic shergottite. *Meteoritics & Planetary Science*, *38*(12), 1865–1875. https://doi.org/10.1111/j.1945-5100.2003.tb00020.x

Warren, P. H. (1994). Lunar and Martian Meteorite Delivery Services. *Icarus*, *111*(2), 338–363. https://doi.org/10.1006/icar.1994.1149

Werner, S. C., Ody, A., and Poulet, F. (2014). The Source Crater of Martian Shergottite Meteorites. *Science* 343, 1343-1346.

Wieler, R., Huber, L., Busemann, H., Seiler, S., Leya, I., Maden, C., Masarik, J., Meier, M. M. M., Nagao, K., Trappitsch, R., & Irving, A. J. (2016). Noble gases in 18 Martian meteorites and angrite Northwest Africa 7812—Exposure ages, trapped gases, and a re-evaluation of the evidence for solar cosmic ray-produced neon in shergottites and other achondrites. *Meteoritics & Planetary Science*, *51*(2), 407–428. https://doi.org/10.1111/maps.12600

Wright, I., Grady, M., & Pillinger, C. (1989). Organic materials in a Martian meteorite. *Nature*, *340*(6230), 220–222.

Yoshizaki, T., & McDonough, W. F. (2020). The composition of Mars. *Geochimica et Cosmochimica Acta*, *273*, 137–162. https://doi.org/10.1016/j.gca.2020.01.011

# Appendix A

Plane polarized light (PPL) and cross polarized light (XPL) thin section scans available for the 14 thin sections described in Chapter 2.

**<u>Jiddat al Harasis 479</u>**

*TEP 1*

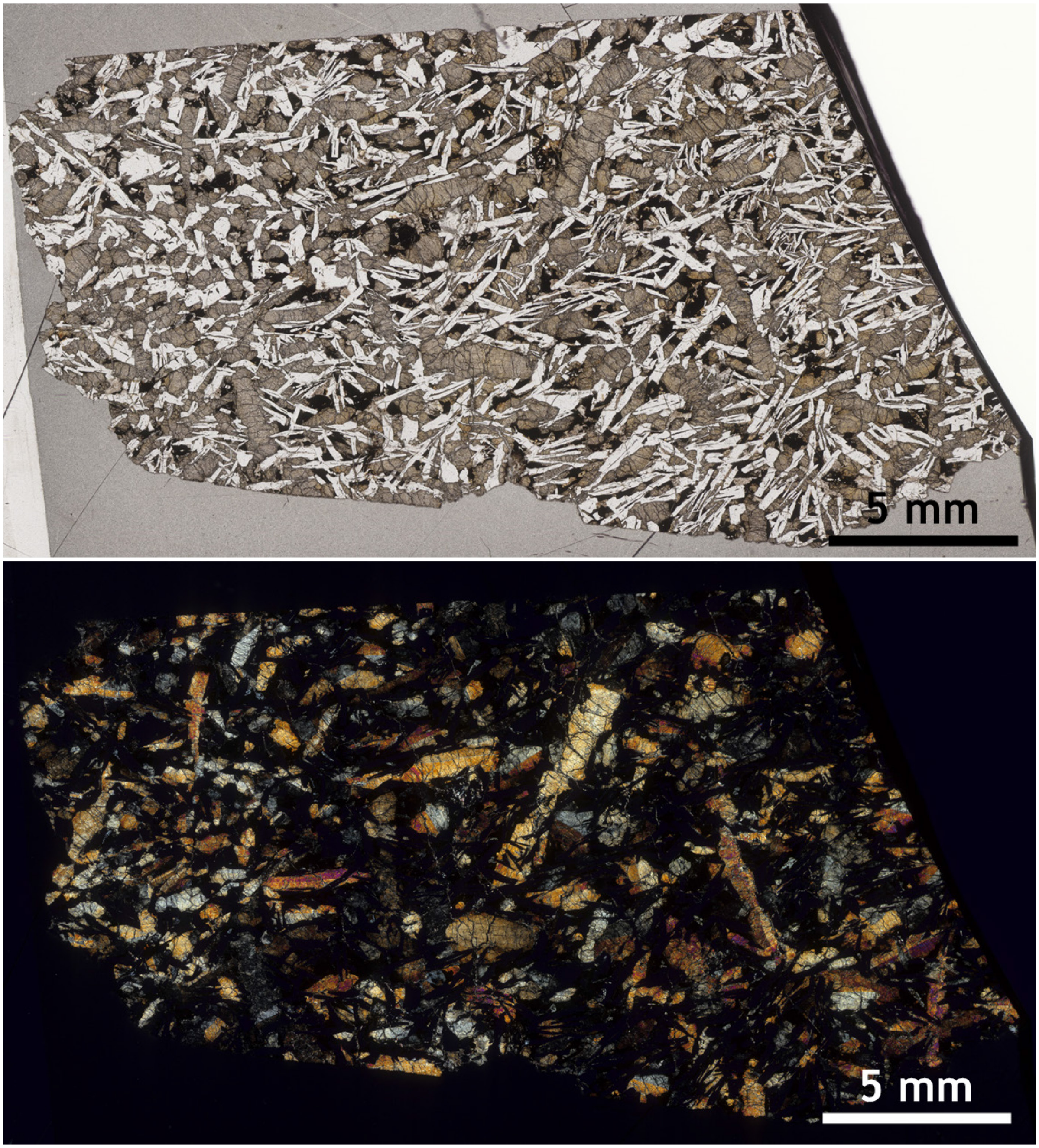

*TEP 2*

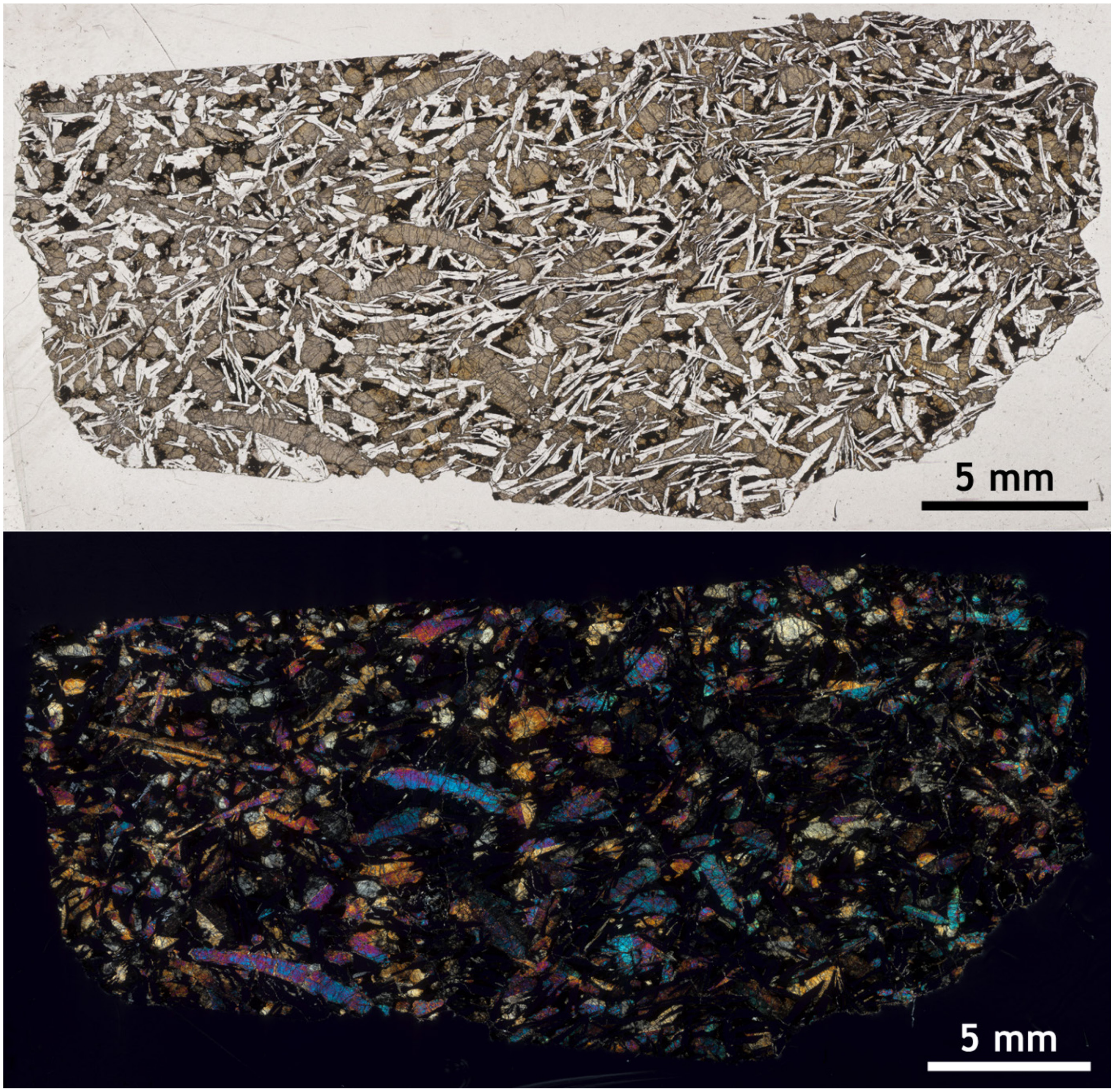

**Ksar Ghilane 002**

## Northwest Africa 2046

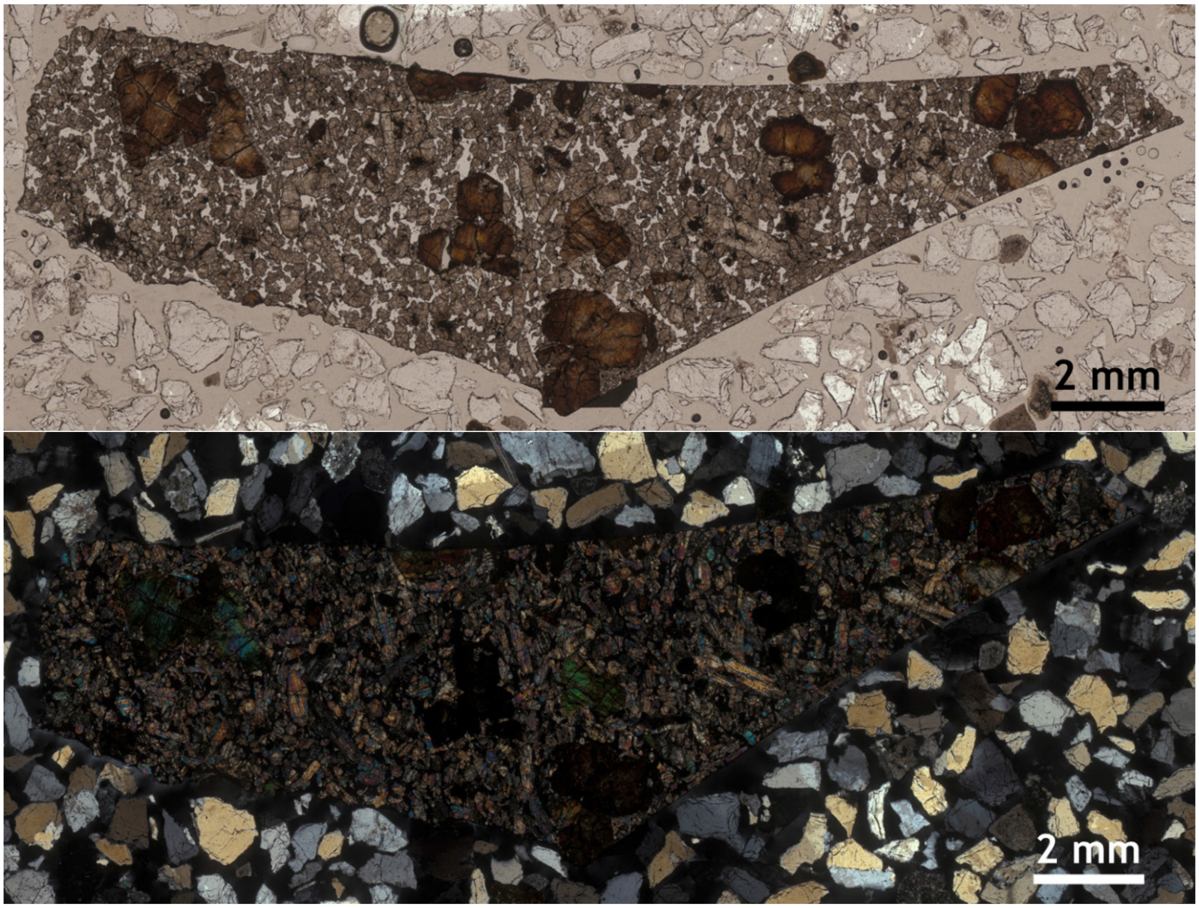

## Northwest Africa 2626

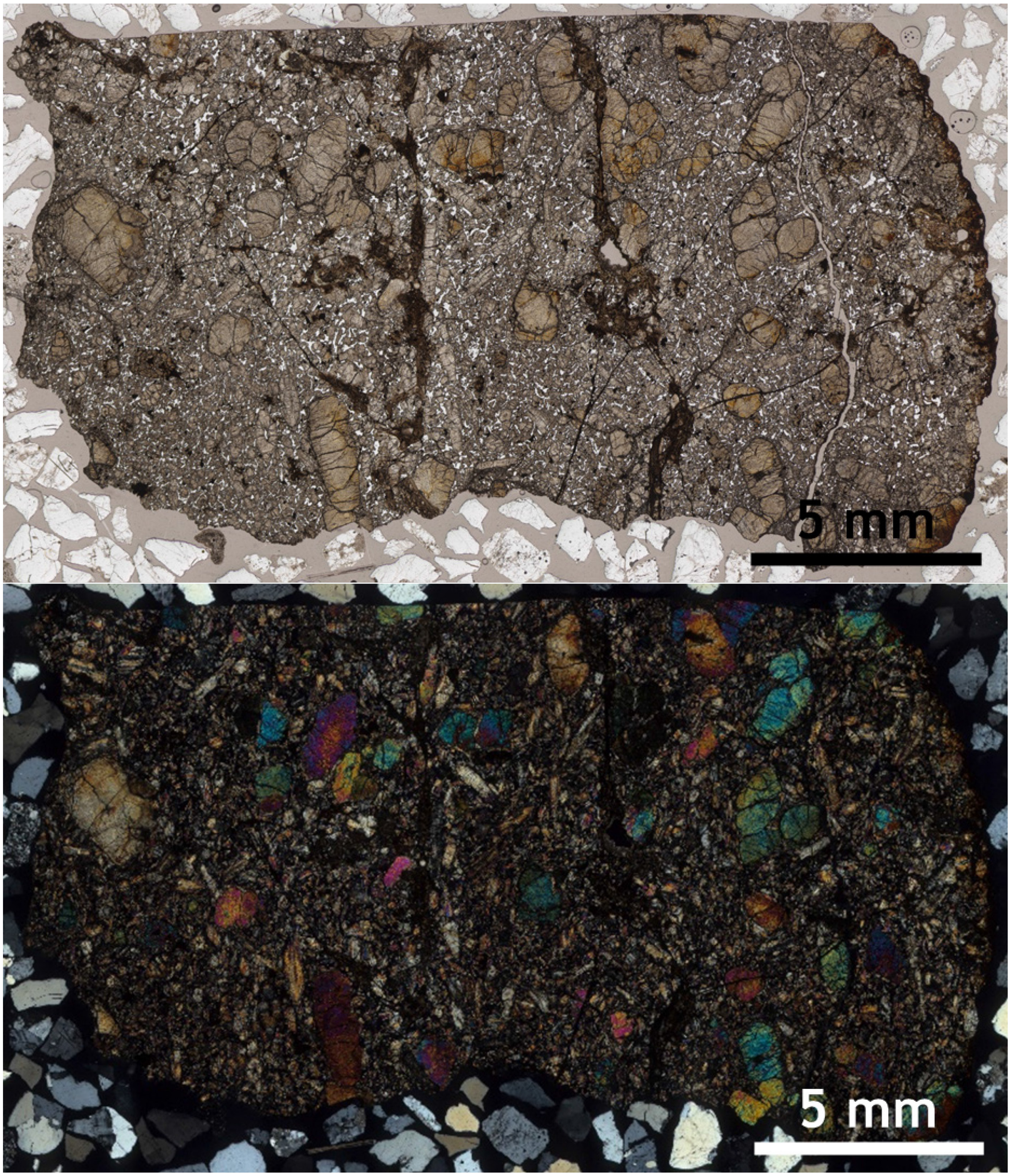

## **Northwest Africa 6162**

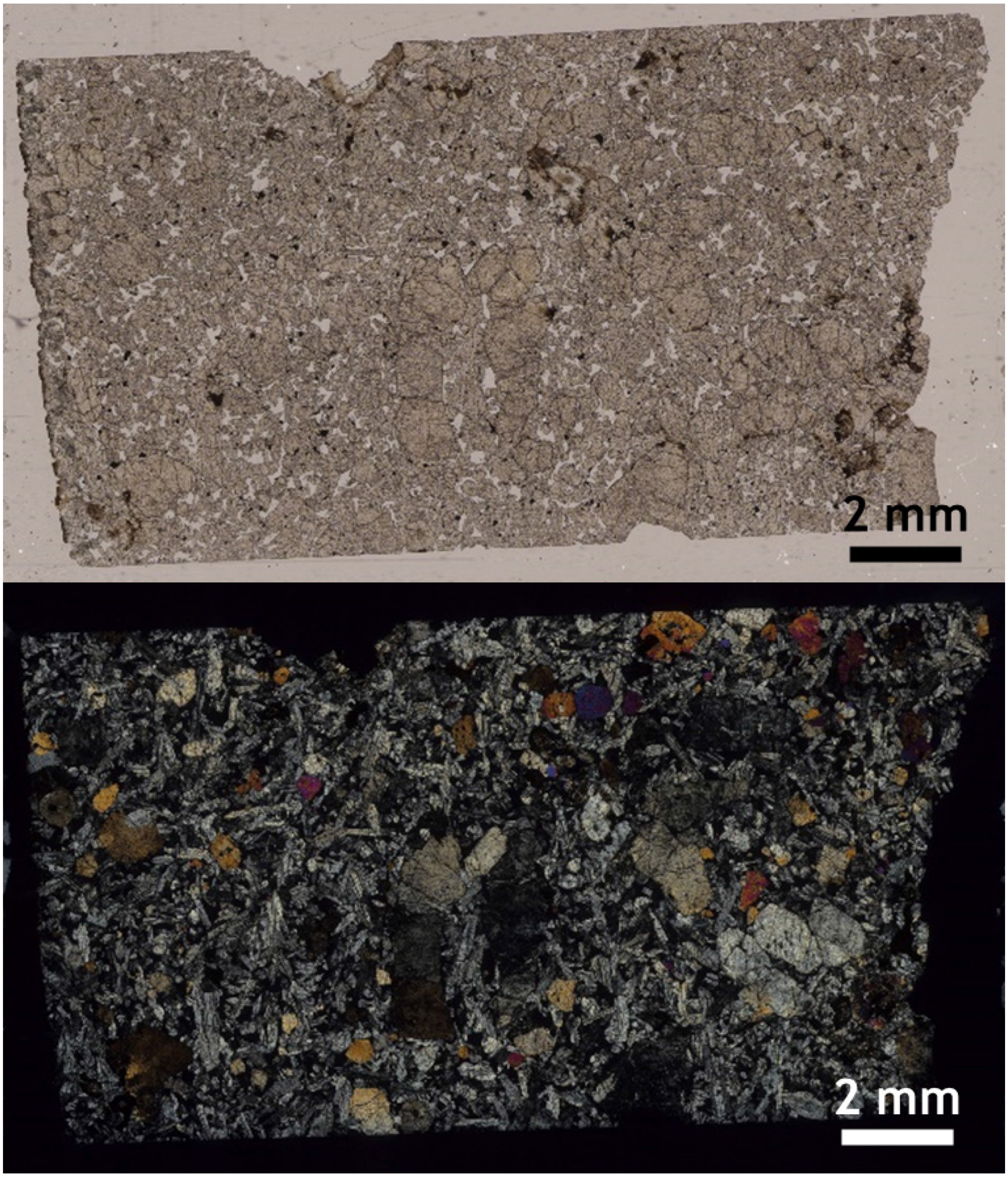

## Northwest Africa 7635

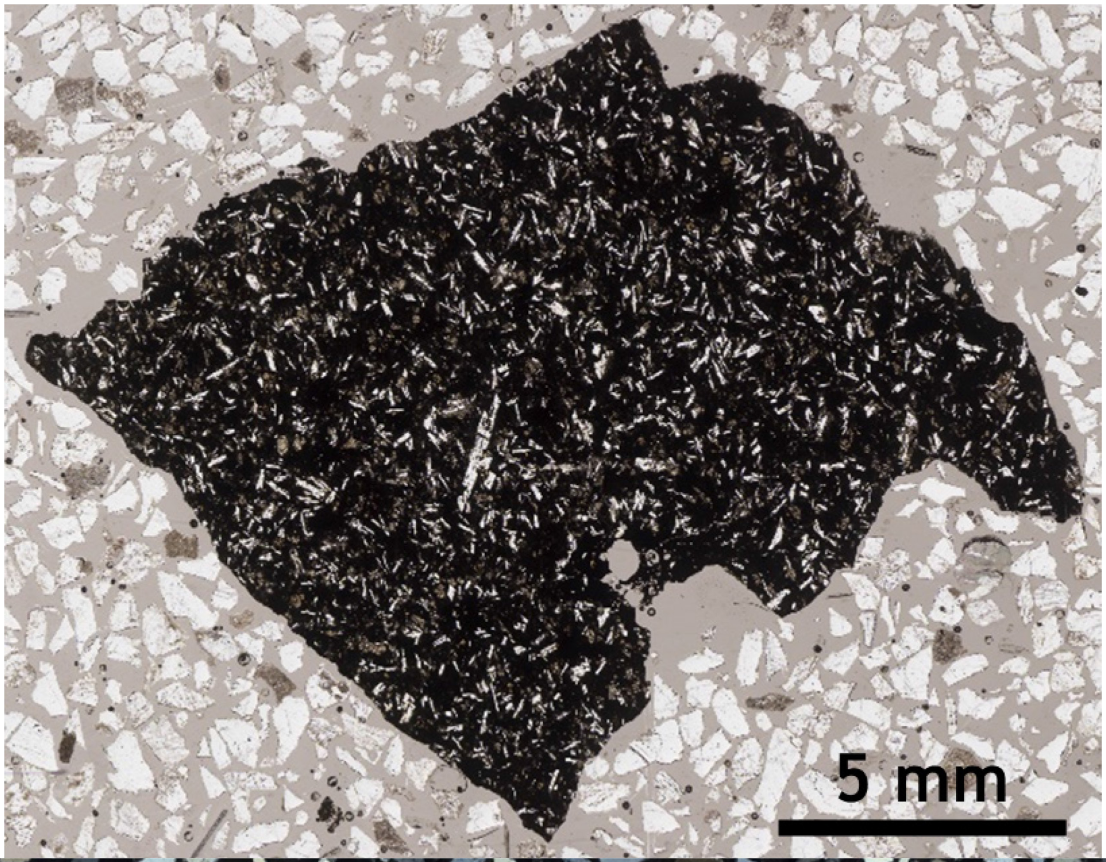

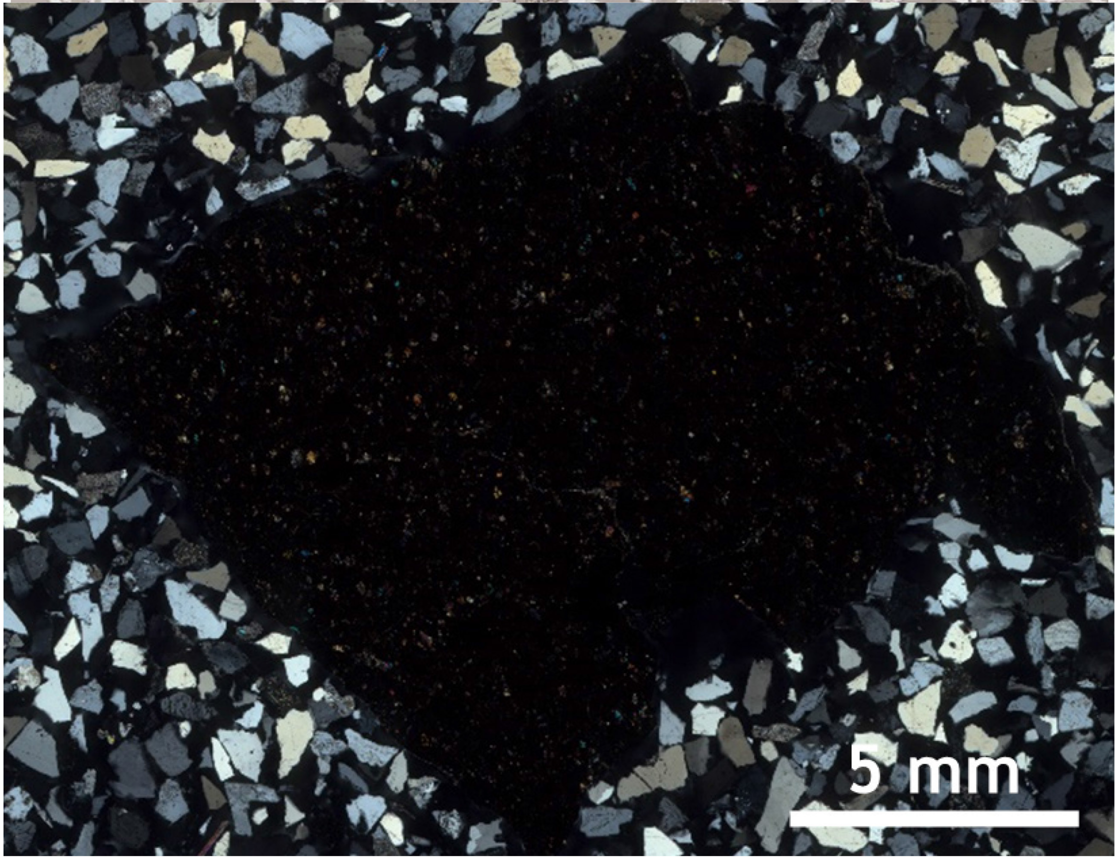

## Northwest Africa 10299

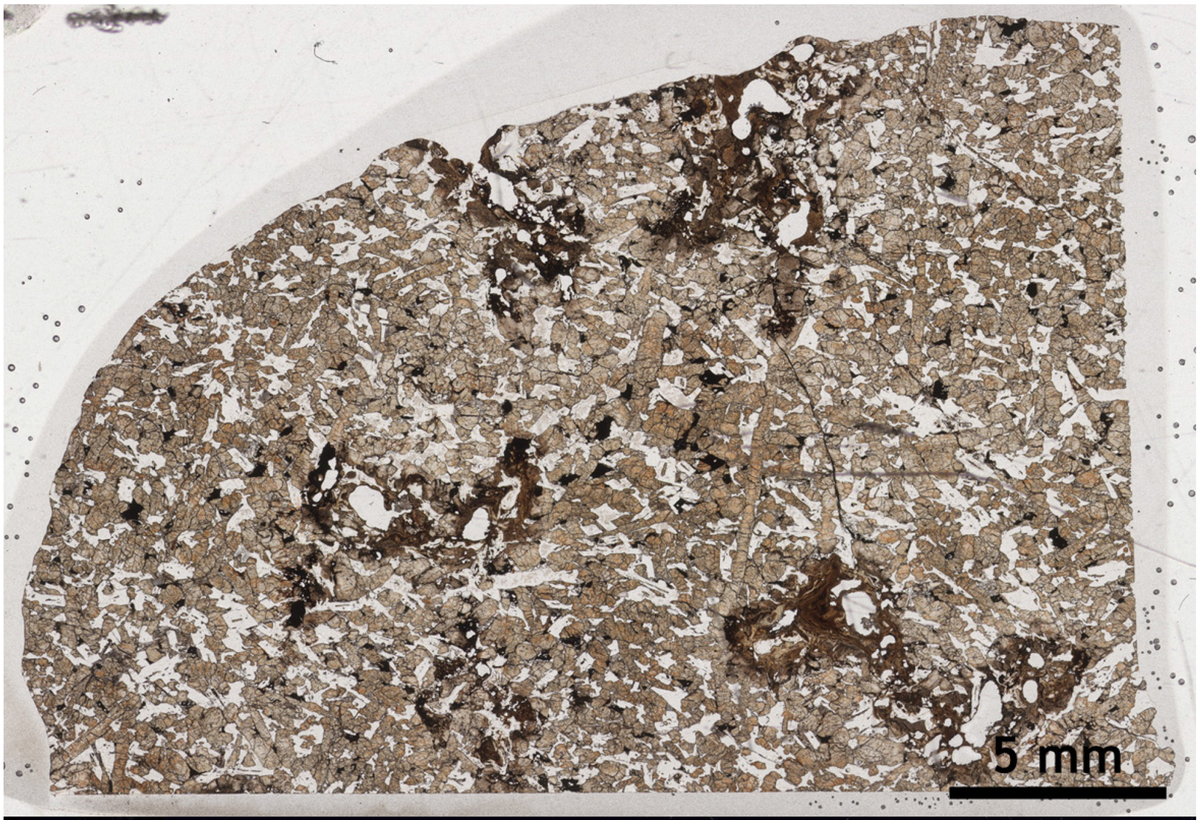

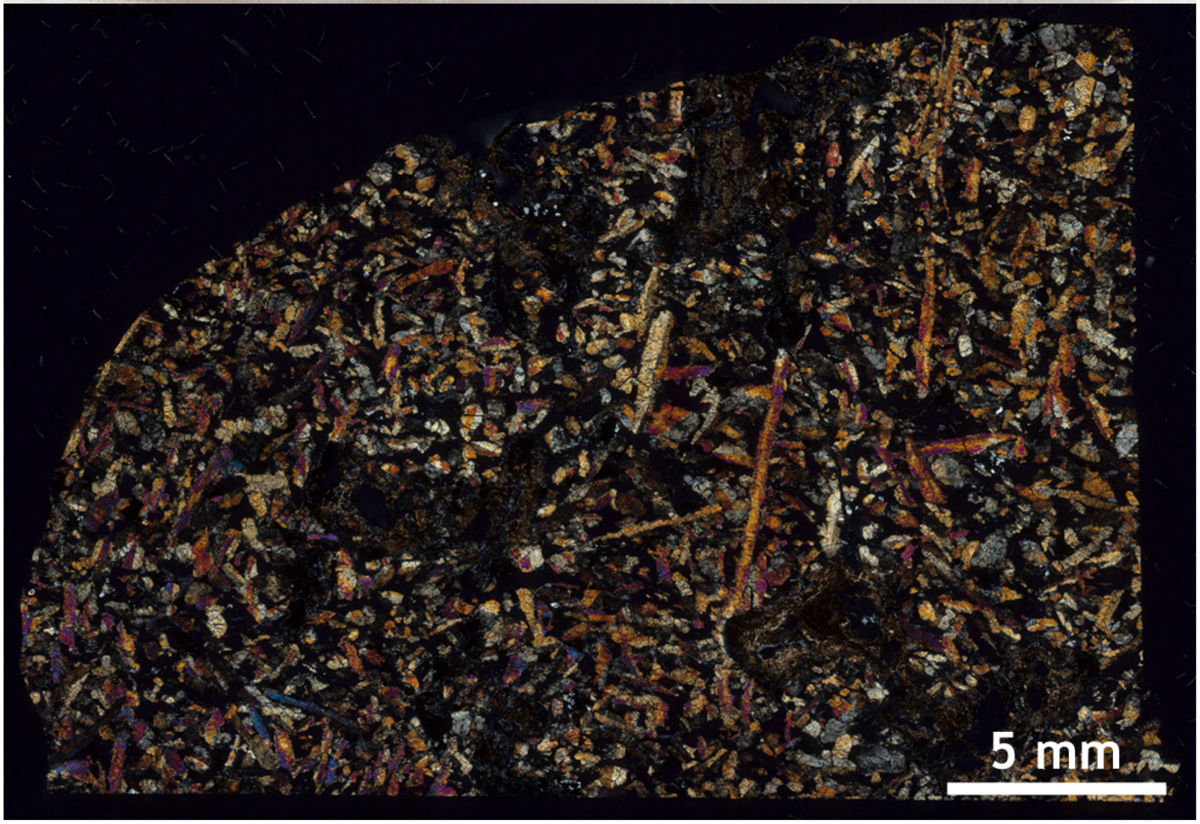

## Northwest Africa 11057

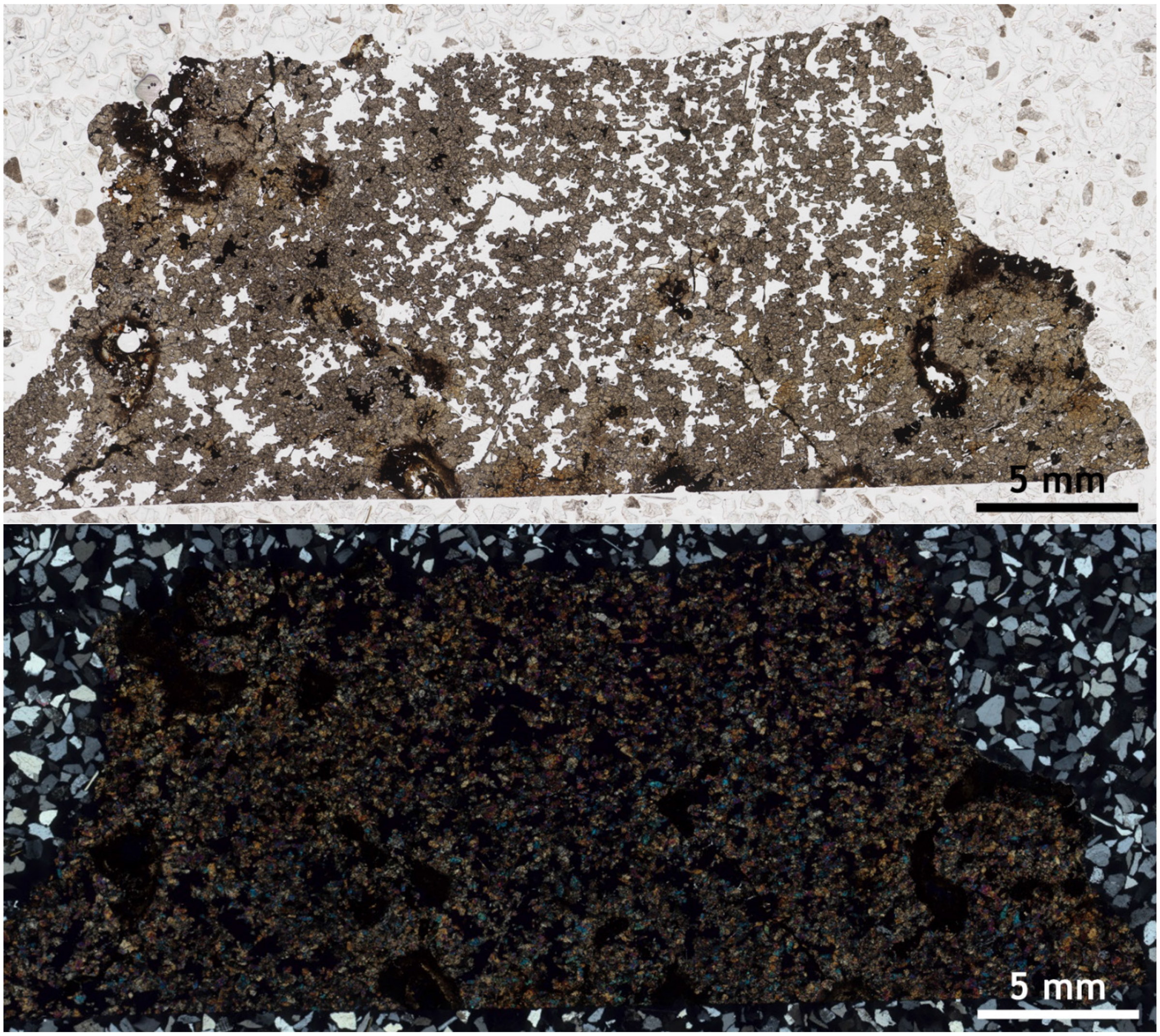

## Northwest Africa 11073

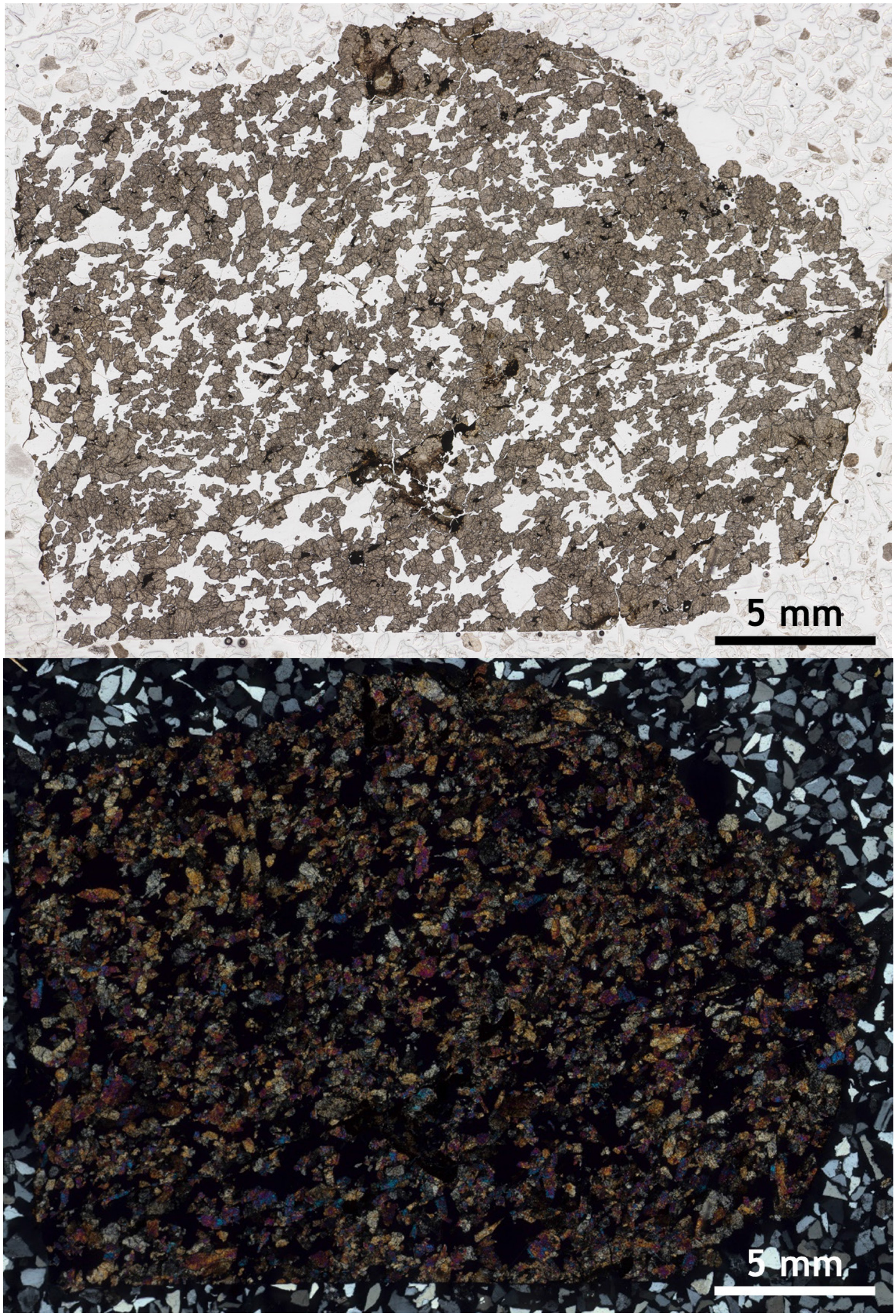

## Northwest Africa 11255

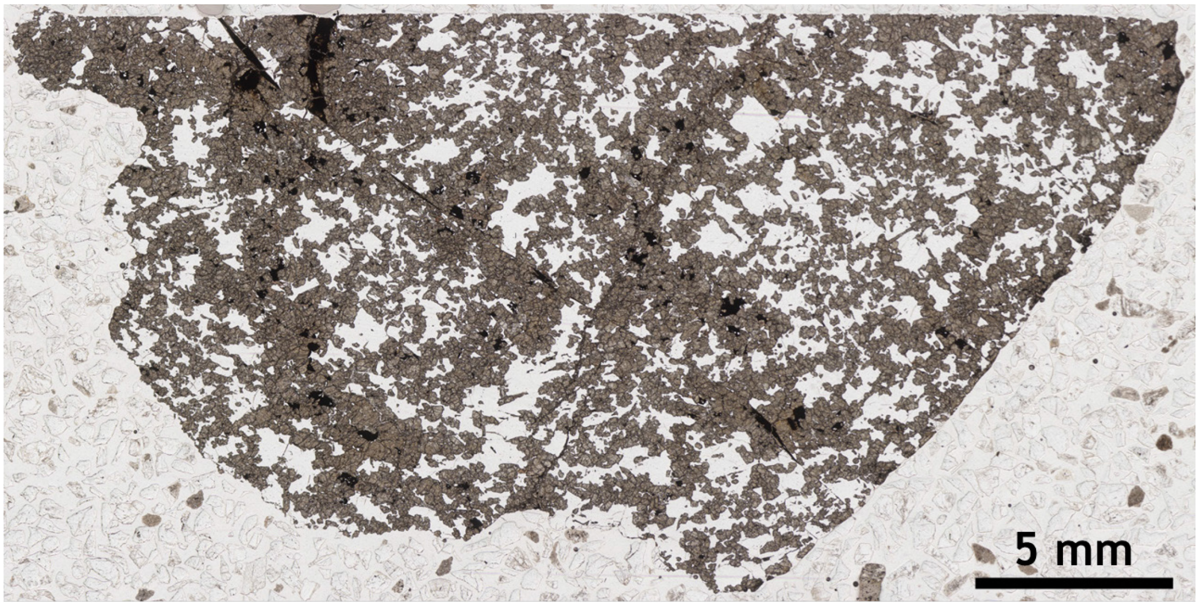

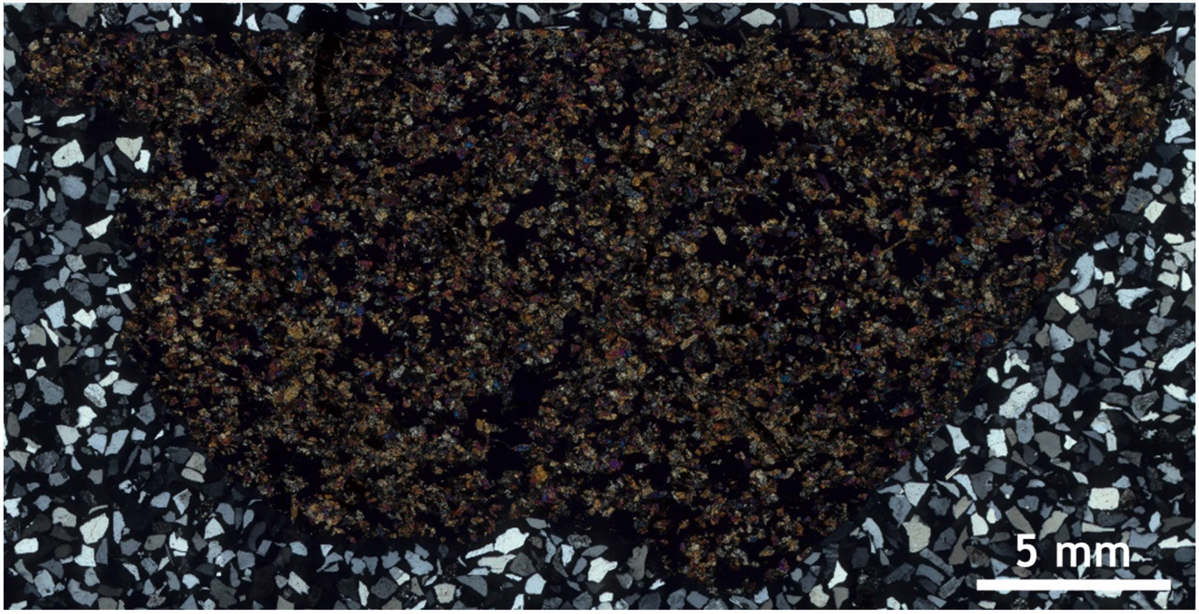

## Northwest Africa 11955

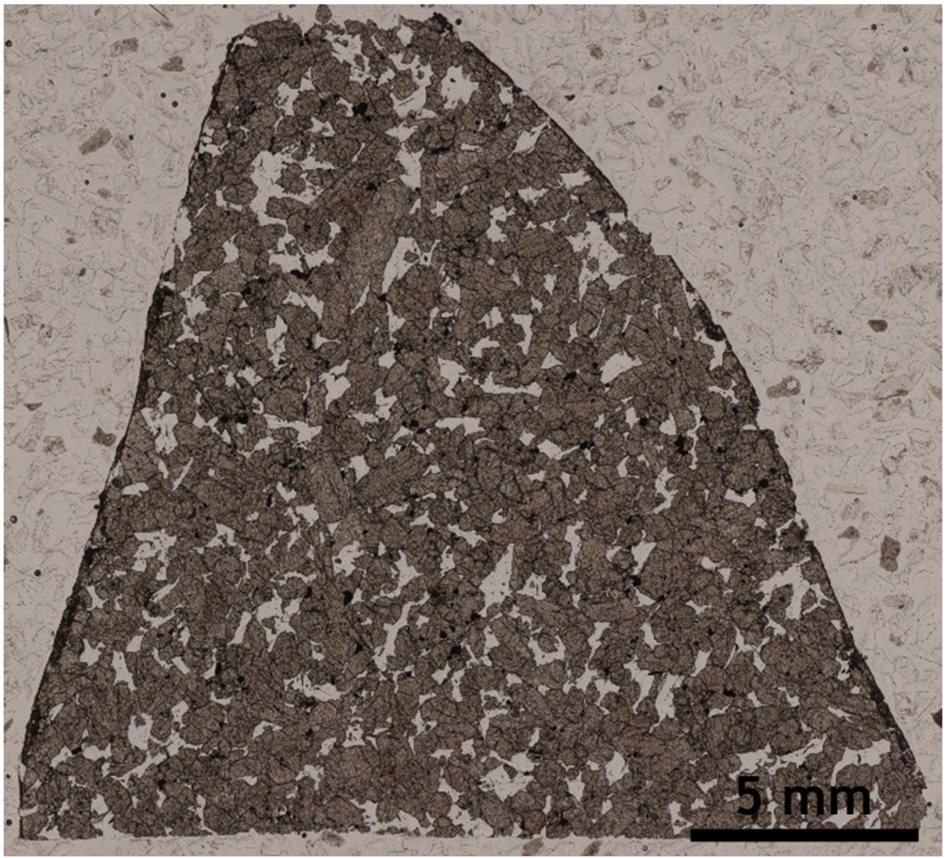

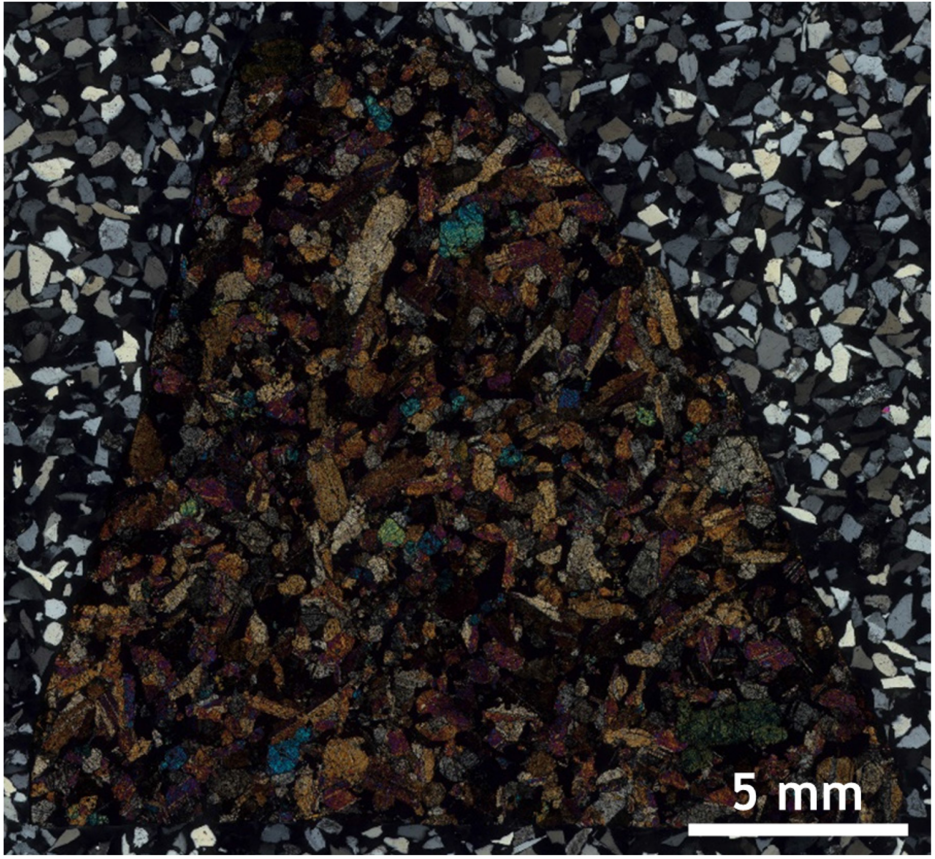

## Northwest Africa 12262

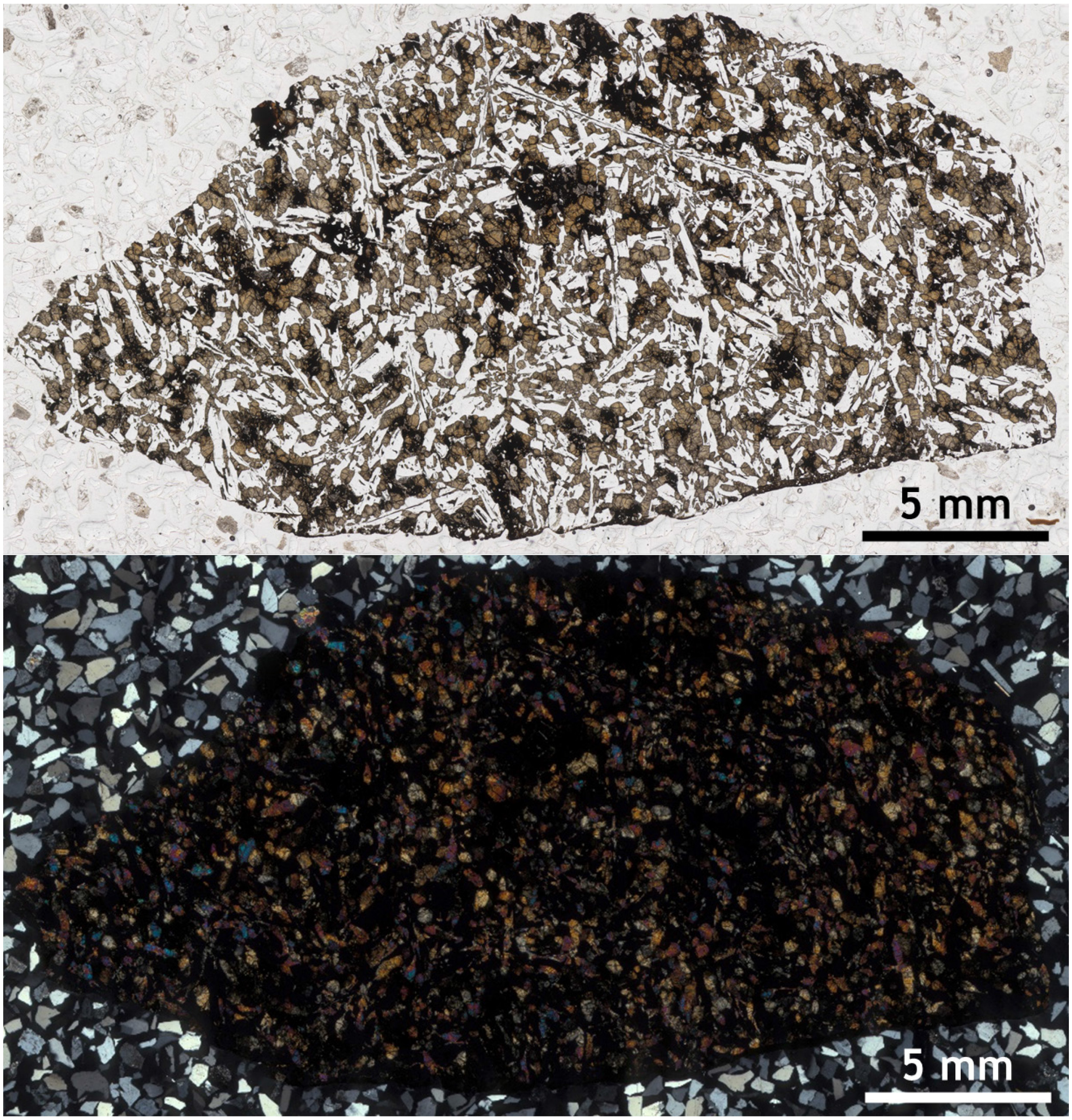

## Northwest Africa 12919

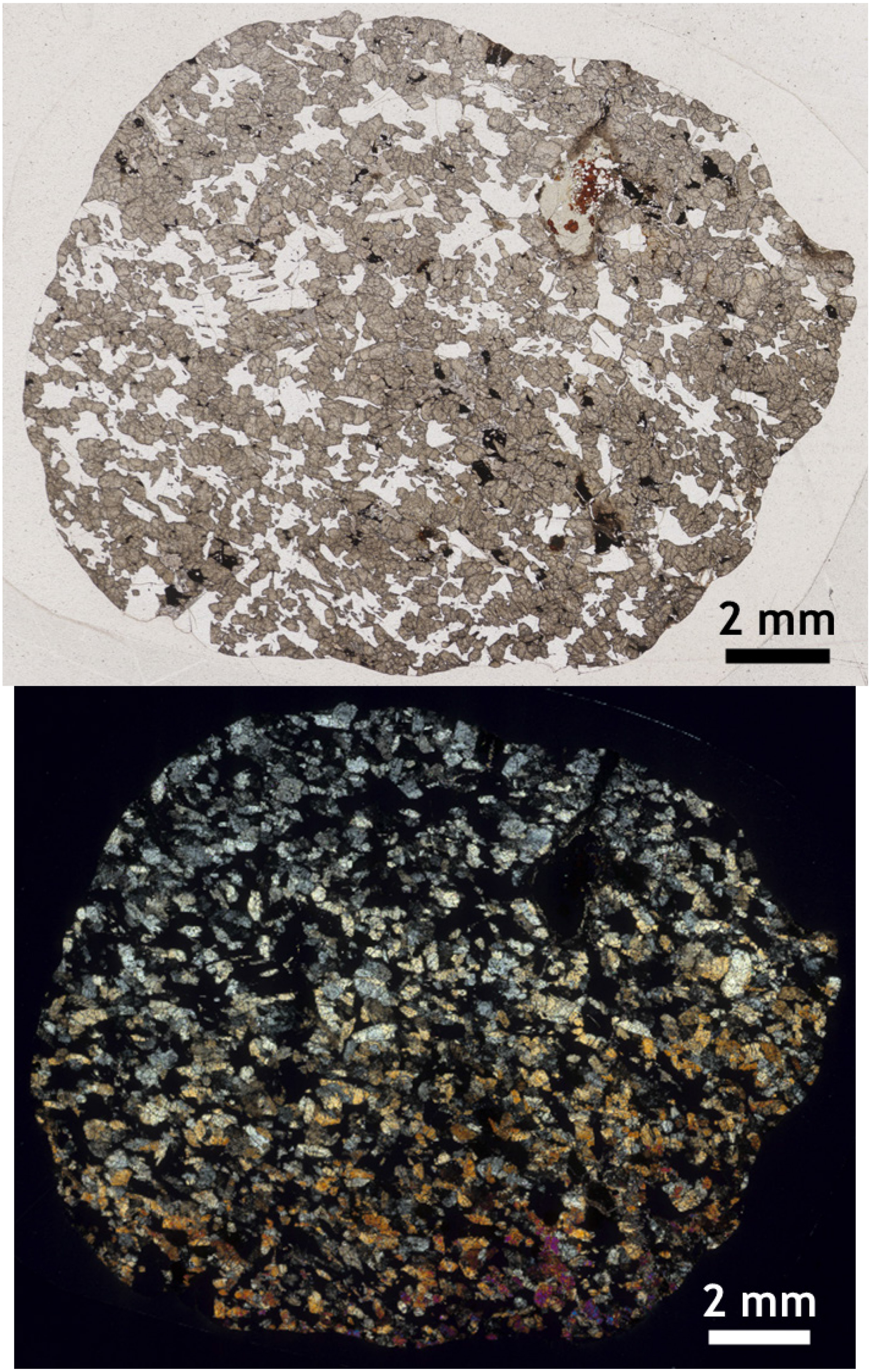

# Appendix B

All 52 craters that were candidates for at least one of the meteorites investigated in Chapter 3.

| Crater Name | Robbins and Hynek (2012) ID[a] | Latitude | Longitude | Diameter (km) | Preservation[c] | Degradation[d] |
|---|---|---|---|---|---|---|
| Unnamed | 15-001441 | 22.5 | 151.4 | 2.5 | 5 | n.d. |
| Zumba | 17-000913 | -28.7 | 226.9 | 2.8 | 5 | n.d. |
| Unnamed | 21-004283 | -22.2 | 67.3 | 2.85 | 3 | n.d. |
| Unnamed | 15-001066 | 17.2 | 160.0 | 3.2 | 4 | 4 |
| Unnamed | 15-001031 | 20.2 | 158.9 | 3.2 | 4 | 4 |
| Unnamed | 18-000821 | -17.1 | 297.0 | 6.1 | 3 | 3 |
| Unnamed | 02-000325 | 43.3 | 225.8 | 6.4 | 5 | 3 |
| Unnamed | 15-000464 | 8.2 | 142.0 | 6.5 | 3 | 4 |
| Unnamed | 09-000103 | 15.8 | 267.8 | 8 | 3 | 4 |
| Unnamed | 02-000244 | 31.1 | 212.4 | 8.1 | 3 | 4 |
| Echus | 10-000512 | 11.4 | 283.1 | 8.8 | 3 | 4 |
| Unnamed | 02-000223 | 46.6 | 239.0 | 8.9 | 3 | 4 |
| Unnamed | 03-000308 | 39.9 | 257.4 | 9.2 | 3 | 3 |
| Unnamed | 16-001260 | -15.7 | 203.6 | 9.7 | 4 | 1 |
| Zunil | 15-000240 | 7.7 | 166.2 | 10.2 | 5 | 4 |
| Unnamed | 21-001301 | -22.3 | 64.9 | 10.6 | 3 | 3 |
| Unnamed | 02-000166 | 40.5 | 231.7 | 10.8 | 4 | 4 |
| Canala | 10-000384 | 24.3 | 279.9 | 11.2 | 5 | 2 |
| Unnamed | 03-000226 | 55.4 | 253.6 | 12 | 3 | n.d. |
| Unnamed | 03-000205 | 32.6 | 254.1 | 12.2 | 4 | 3 |
| Unnamed | 10-000307 | 18.0 | 272.3 | 13.2 | 3 | 4 |
| Corinto | 15-000165 | 17.0 | 141.7 | 13.5 | 5 | 4 |
| Domoni | 02-000116 | 51.4 | 234.4 | 14 | 5 | 3 |
| Unnamed | 03-000153 | 31.8 | 296.4 | 15.3 | 3 | 3 |
| Unnamed | 02-000095 | 39.1 | 238.7 | 15.4 | 3 | 4 |
| Unnamed | 17-000058 | -18.4 | 228.6 | 19 | 3 | 4 |
| Unnamed | 03-000099 | 30.8 | 297.6 | 19 | 3 | 4 |
| Unnamed | 09-000015 | 19.3 | 260.1 | 19.6 | 5 | 3 |
| Unnamed | 09-000010 | 14.0 | 264.0 | 20.7 | 3 | 3 |
| Unnamed | 03-000082 | 44.6 | 253.0 | 21.2 | 4 | 4 |
| Unnamed | 09-000007 | 18.0 | 249.1 | 22.2 | 4 | 4 |

| | | | | | | |
|---|---|---|---|---|---|---|
| Tooting | 08-000060 | 23.2 | 207.8 | 28.9 | 5 | 4 |
| Acidalia | 04-000080 | 35.8 | 319.2 | 33.6 | 3 | 4 |
| Kotka | 15-000029 | 19.3 | 169.9 | 38.9 | 3 | 3 |
| Unnamed | 20-000190 | -21.5 | 44.8 | 41.2 | 3 | 3 |
| Unnamed | 21-000135 | -22.6 | 65.4 | 43.1 | 3 | 3 |
| Isidis | 14-000035 | 10.2 | 94.3 | 47.5 | 3 | 4 |
| Unnamed | 24-000163 | -43.9 | 206.9 | 48.5 | 3 | 1 |
| Ottumwa | 10-000033 | 24.6 | 304.3 | 50.1 | 3 | 3 |
| Unnamed | 20-000126 | -26.1 | 20.9 | 50.4 | 3 | 3 |
| Unnamed | 21-000102 | -18.8 | 62.7 | 52.2 | 3 | 3 |
| Unnamed | 20-000103 | -19.3 | 32.2 | 53.5 | 3 | 3 |
| Bamberg | 04-000023 | 39.7 | 356.9 | 54.6 | 3 | 3 |
| Cimmeria | 29-000095 | -27.1 | 133.0 | 55 | 3 | 3 |
| Mojave | 11-000056 | 7.5 | 327.0 | 56.8 | 5 | 3 |
| Unnamed | 22-000059 | -13.7 | 113.5 | 58 | 4 | 4 |
| Horowitz | 29-000055 | -32.0 | 140.8 | 63.1 | 3 | 4 |
| Poynting | 09-000000 | 8.4 | 247.3 | 69 | 3 | 3 |
| Unnamed | 27-000055 | -43.5 | 12.7 | 69.5 | 3 | 3 |
| Lockyer | 15-000008 | 27.8 | 160.5 | 71.3 | 3 | 3 |
| Pál | 28-000021 | -31.3 | 108.7 | 73.3 | 4 | 3 |
| Sabaea | 20-000045 | -19.2 | 36.0 | 76.5 | 3 | 3 |

Notes: [a]Data source from Robbins and Hynek (2012). [c,d]Relative preservation of the crater as defined by Tornabene et al. (2012) and Robbins and Hynek (2012), respectively – Preservation is scaled from 1-5 with 5 being the most well-preserved and degradation is scaled from 1-4 with 4 being the most well-preserved. n.d. = no data